STUDY OF III-NITRIDE GROWTH KINETICS BY MOLECULAR-BEAM EPITAXY

A Dissertation
Presented to
The Academic Faculty

By

Michael W. Moseley

In Partial Fulfillment
Of the Requirements for the Degree
Doctor of Philosophy in Electrical and Computer Engineering

Georgia Institute of Technology

May 2013

STUDY OF III-NITRIDE GROWTH KINETICS BY MOLECULAR-BEAM EPITAXY

Dr. W. Alan Doolittle
School of Electrical and Computer Engineering
Georgia Institute of Technology

Dr. Shyh-Chiang Shen
School of Electrical and Computer Engineering
Georgia Institute of Technology

Dr. P. Douglas Yoder
School of Electrical and Computer Engineering
Georgia Institute of Technology

Dr. Jongman Kim
School of Electrical and Computer Engineering
Georgia Institute of Technology

Dr. Samuel Graham
School of Mechanical Engineering
Georgia Institute of Technology

Date approved: March 5, 2013

To my wife, for inspiring me
To my mother, for supporting me
To my father, for challenging me

ACKNOWLEDGEMENTS

First and foremost, I would like to thank my family for their unconditional support. My mother and father have both encouraged and challenged me since my earliest memory, and fostered my interest in science. My wife Susie has been a constant source of support throughout my years in college, enduring the difficult times and celebrating the victories with me. Without the strength and love of my family, I would not have succeeded in my graduate studies.

I owe my thesis advisor, Dr. W. Alan Doolittle, an enormous debt of gratitude. He has demonstrated a great deal of patience and encouragement as I have grown professionally and personally. I consider him a colleague, a friend, and a mentor.

I would also like to thank past and present members of Dr. Doolittle's research group, Walter Henderson, Brendan Gunning, Jordan Greenlee, Dr. Daniel Billingsley, Jonathan Lowder, Laws Calley, Dr. Elaissa Trybus, Dr. Shawn Burnham, Dr. Gon Namkoong, Chloe Fabien, Dr. David Pritchett, and Dr. Kyoung Lee. I am privileged to have worked with these extremely bright minds.

I would like to thank my thesis committee, Dr. Shyh-Chiang Shen, Dr. Douglas Yoder, Dr. Jongman Kim, and Dr. Samuel Graham for their guidance throughout my thesis defense. Additionally, the staff of the MiRC has been extremely helpful throughout my research, especially Dean Sutter, Scott Fowler, Gary Spinner, and Charlie Suh.

TABLE OF CONTENTS

LIST OF TABLES

LIST OF FIGURES

LIST OF NOMENCLATURE

Å	Angstrom (10^{-10} meter)
λ	wavelength
λ_{mfp}	mean-free path
ρ	resistivity
σ	conductivity
Ω	Ohm
μ	carrier mobility
μm	micron (10^{-6} meter)
2DEG	two-dimensional electron gas
2DHG	two-dimensional hole gas
a_{AlN}	theoretical in-plane lattice spacing for AlN
a_{GaN}	theoretical in-plane lattice spacing for GaN
a_{exp}	measured in-plane lattice spacing
AFM	atomic-force microscopy
Al	aluminum
AlGaN	aluminum gallium nitride
AlN	aluminum nitride
C-V	capacitance-voltage
c_{AlN}	theoretical 0001 lattice spacing for AlN
c_{GaN}	theoretical 0001 lattice spacing for GaN
c_{exp}	measured 0001 lattice spacing
Cxy	elastic constant
DI	deionized
E_g	bandgap energy
eV	electron volt
FWHM	full width at half maximum
Ga	gallium
GaAs	gallium arsenide
GaN	gallium nitride
H_2SO_4	sulfuric acid
H_2O_2	hydrogen peroxide
HEMT	high electron mobility transistor
HF	hydrofluoric acid
In	indium
InGaN	indium gallium nitride
InN	indium nitride
LD	laser diode
LED	light-emitting diode
MBE	molecular-beam epitaxy
Mg	magnesium
MOCVD	metal-organic chemical vapor deposition
MOMBE	metal-organic molecular beam epitaxy
MOVPE	metal-organic vapor phase epitaxy

N	nitrogen
NH3	ammonia
PL	photoluminescence
$Q_{x,y}$	x-ray diffraction scattering vectors
RC	rocking curve
RF	radio frequency
RGA	residual-gas analysis
RHEED	reflection high-energy electron diffraction
rms	root-mean-square
RSM	reciprocal space map
sccm	standard cubic centimeters per second
SEM	scanning electron microscope
SiC	silicon carbide
SIMS	secondary-ion mass spectroscopy
T_{sub}	substrate (growth) temperature
UHV	ultra-high vacuum
UV	ultraviolet
W	Watts
XRD	x-ray diffraction

SUMMARY

Since the initial breakthroughs in structural quality and p-type conductivity in GaN during the late 1980s, the group-III nitride material system has attracted an enormous amount of interest because of its properties and applications in both electronics and optoelectronics. Although blue light-emitting diodes have been commercialized based on this success, much less progress has been made in ultraviolet emitters, green emitters, and photovoltaics. This lack of development has been attributed to insufficient structural and electrical material quality, which is directly linked to the growth of the material. The objective of this work is to expand the understanding of III-nitride growth towards the improvement of current device capabilities and the facilitation of novel device designs.

Group-III nitride thin films are grown by molecular-beam epitaxy in a pulsed, metal-rich environment. The growths of nitride binaries and ternaries are observed *in situ* by transient reflection high-energy electron diffraction (RHEED) intensities, which respond to the behavior of atoms on the growing surface. By analyzing and interpreting these RHEED signatures, a comprehensive understanding of nitride thin film growth is obtained.

The growth kinetics of unintentionally doped GaN by metal-rich MBE are elucidated, and a novel method of *in situ* growth rate measurement is discovered. This technique is expanded to InN, highlighting the similarity in molecular-beam epitaxy growth kinetics between III-nitride binaries. The growth of Mg-doped GaN is then explored to increase Mg incorporation and electrical activation. The growth of $In_xGa_{1-x}N$

alloys are investigated with the goal of eliminating phase separation, which enables single-phase material for use in photovoltaics. Finally, the growth of unintentionally doped and Mg-doped AlGaN is investigated towards higher efficiency light emitting diodes.

These advancements in the understanding of III-nitride growth will address several critical problems and enable devices relying on consistent growth in production, single-phase material, and practical hole concentrations in materials with high carrier activation energies.

CHAPTER 1: INTRODUCTION

The group-III nitride materials system boasts an outstanding set of properties with applications in light emission, photovoltaics, and power electronics. However, many of these applications are currently unable to be realized by conventional III-nitride thin film growth techniques. For instance, Indium-containing III-nitride materials experience several forms of phase separation, which cause compositional fluctuations as well as the formation of two or more separate phases. Hole concentrations in p-type III-nitride films have historically been very low as a result of the difficulty in incorporating electrically active Mg. Finally, there exists no lattice-matched substrate for III-nitride epitaxy, limiting material quality and requiring buffer layer growth. The objective of this work is to evaluate and solve several pressing issues with the growth of III-nitride compounds towards the improvement of current device performance and the facilitation of novel device designs.

Molecular-beam epitaxy (MBE) provides a unique environment for the study of group-III nitride thin film growth. This growth technology involves the evaporation of elemental source materials (In, Ga, Al, N) onto a heated substrate in an ultra-high vacuum environment. This pristine setting allows for the analysis and constant observation of atomic interactions on the growth surface using *in situ* characterization tools unavailable in other growth technologies. By understanding, monitoring, and controlling the behavior of these reactants during the epitaxial process, the structural and electrical quality of group-III nitride materials will be improved.

1.1 Molecular-Beam Epitaxy

Epitaxy is a term derived from Greek "epi" meaning above, upon, or outer, and "taxis" meaning in an ordered manner [1]. Thus, epitaxy pertains to the growth of a crystalline material layer by layer. Molecular-beam epitaxy is a growth technique for the epitaxial growth of thin films pioneered by Alfred Cho at Bell Telephone Labs. Although first performed in 1968 by Davey and Pankey [2], the term "molecular-beam epitaxy" was not coined until 1970 by Cho [3]. MBE typically involves the transport of reactants from solid sources through an ultra-high vacuum (~10^{-9} Torr) environment, where they collide on a crystalline substrate to form a single-crystal thin film. An illustration of a basic MBE system is shown in Figure 1.1.

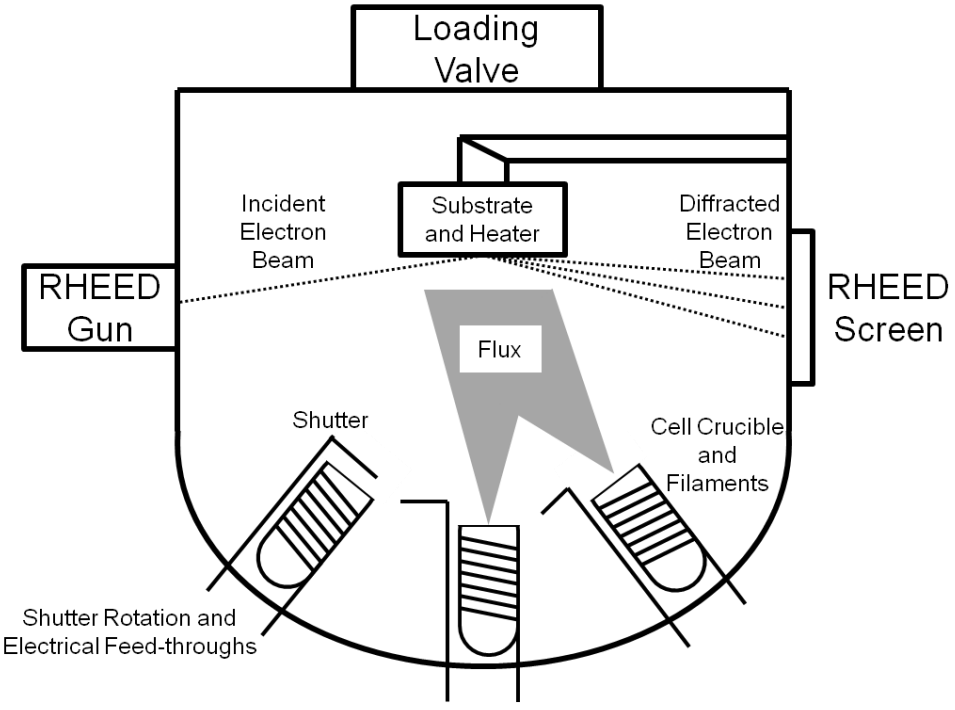

Figure 1.1: Top-down view of a standard MBE chamber, showing effusion cells, substrate heater, and reflection high-energy diffraction characterization equipment.

The low pressures involved in molecular-beam epitaxy increase the distance atoms in the chamber must travel before colliding with another gas particle, known as the mean-free path. In MBE, reactant atoms evaporating out of the effusion cell crucibles would strike the chamber walls many times before hitting another reactant atom or a residual gas particle. This extremely large mean-free path facilitates the existence of a "molecular beam", since these reactant fluxes are able to travel in a straight line to the growth surface, reducing gas-phase interactions and allowing the crystalline structure of the substrate to translate into the film. The equation for calculating the mean-free path of a particle is shown by

$$\lambda_{mfp} = \frac{k_B T}{\pi\, d^2 P} \tag{1.1}$$

where λ_{mfp} is the mean free path, k_B is Boltzmann's constant, T is temperature, d is the atomic collision diameter, and P is pressure.

Solid sources, such as group-III elements in III-V MBE, are generally heated in Knudsen cells inside vacuum, where the reactant is contained in a crucible surrounded by a heating filament. This filament radiatively heats the crucible, which in turn conducts heat to the source material. As the filament increases the source temperature, the source particles evaporate out of the crucible towards the substrate. The flux of the material exiting this crucible can be controlled by the heat applied through the filament. Physical orifice shutters are usually employed to rapidly cut off or open the supply of material to the growth surface to enable the growth of heterostructures. An illustration of an MBE effusion cell is shown in Figure 1.2, with components labeled. Similarly to cell crucible

heating, substrates are radiatively heated by a closely mounted filament. The supplied heat is used to control surface reactions, either by preventing the incorporation of unwanted species, supplying energy for surface reactant transport, or encouraging certain phases of a particular compound to form.

Some constituents (such as NH_3, N_2, As, and P) require a more complex reactant delivery method. To liberate active N from NH_3 and N_2 molecules, a radio frequency assisted plasma source can be used to converts these gasses into more reactive species. In the case of NH_3, energy supplied from the heated substrate can also assist in generation of significant active nitrogen from the ammonia molecule. As and P are traditionally supplied from a specialized cell with a multi-zone heated crucible known as a cracker. The bottom zone of a cracker provides enough heat for the material to evaporate at the desired flux, but in most cases these molecules then need to be broken into smaller, more reactive constituents. The next zone of the cracker is heated to a much higher temperature, supplying the already evaporated molecules with enough energy to break apart, or "crack". The two-step evaporation process is necessitated in the case of As and P because the excess heat required to crack these molecules would result in enormous amounts of flux if only one heating zone was available. A valve near the end of the cracker can also be used to precisely control the exiting flux, such as in the case of Mg dopants in p-type III-nitride growth. An illustration of an MBE valved cracker is shown in Figure 1.3.

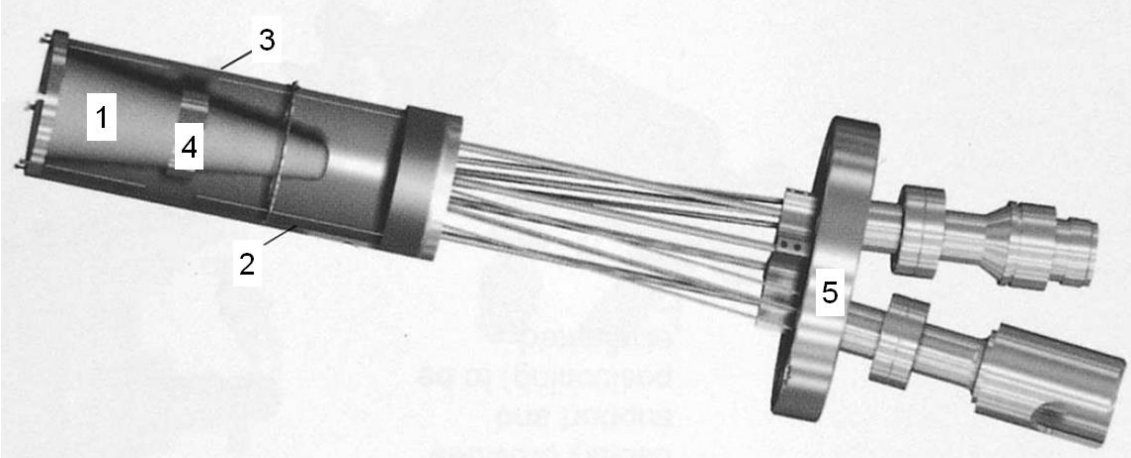

Figure 1.2: Cut-away view of a molecular-beam epitaxy effusion cell, with main components labeled: (1) pyrolytic boron nitride crucible, (2) resistive heating filament, (3) metal radiation shielding, (4) wrap-around thermocouple for temperature measurement, and (5) conflat flange for mounting. From ref [4].

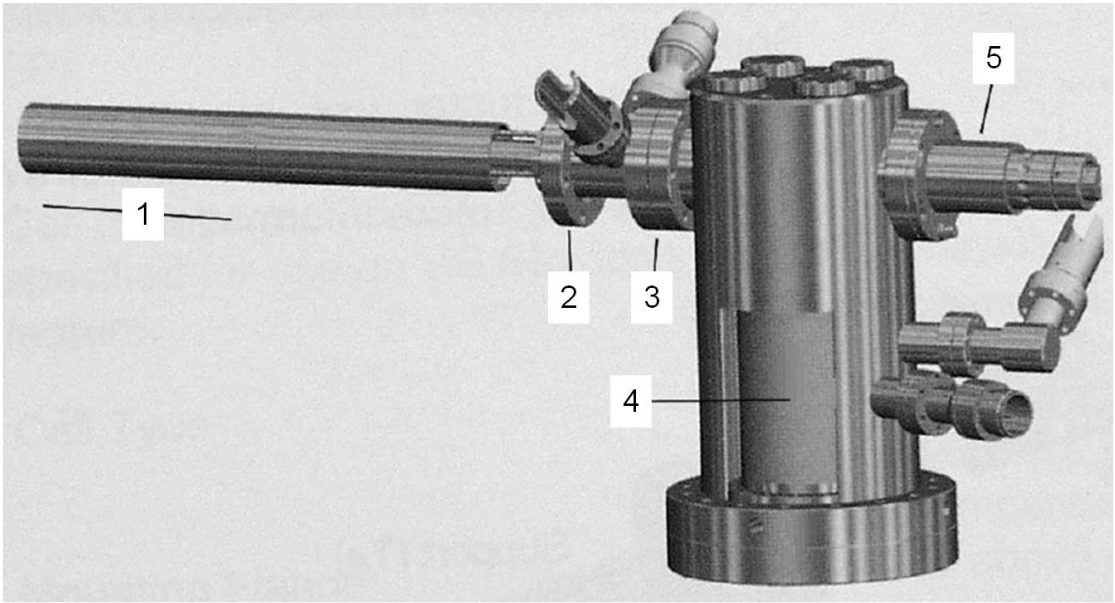

Figure 1.3: Cut-away view of a molecular-beam epitaxy valved cracker cell, with main components labeled: (1) internal hot zone for constituent cracking, (2) conflat flange for mounting, (3) valve seat for isolating charge, (4) external crucible with bulk material for evaporation, and (5) controlled leak valve stem. From ref [4].

The extremely low pressures involved in molecular-beam epitaxy allow for the use of sensitive *in situ* characterization equipment such as reflection high-energy electron diffraction (RHEED) and residual-gas analysis (RGA). These two techniques enable unique studies of surface crystallinity, adsorbed layer accumulation/desorption, and even growth rate. Although RHEED and RGA are by no means the only *in situ* analysis techniques available for MBE, they are prominent enough to be considered standard among MBE equipment and have assisted in propelling MBE forward as an efficient and observant growth tool.

A residual gas analyzer is made of three main components: a filament for gas ionization, a quadrupole biased at an oscillating voltage to manipulate the ionized gas, and a Faraday cup for detecting gathered ions of a specified mass. The basic components of an RGA are shown in Figure 1.4. The filament ionizes gas coming into the RGA, which are then manipulated by the oscillatory voltage in the quadrupole. Only ions of a certain mass, specified by this frequency, are able to pass through the entirety of the quadrupole into the Faraday cup. The Faraday cup then detects the impinging ions as electric current. By changing the quadrupole frequency over time and recording the number of counts registered at the Faraday cup, an RGA is able to scan a range of masses to obtain a gas survey of the system. If needed, these masses can then be summed for an overall pressure estimation. The quadrupole may also be set to one frequency to monitor one mass of interest over time. RGA has been used for simple tasks such as helium leak checking, but also for more complex experiments such as desorption mass spectroscopy to elucidate surface kinetics [5, 6].

A reflection high energy electron diffraction system is composed of two main components: an electron gun to emit electrons at a slight angle towards a sample, and a detector, often consisting of a fluorescent screen. Incoming electrons are diffracted by the surface, and some of these electrons are then collected by the RHEED screen. These collected electrons interfere constructively at certain locations on the screen according to the crystalline structure of the sample. The small angle of incoming electrons prevents electrons escaping from deeper in the material to register on the screen, maintaining RHEED as a surface sensitive technique. MBE growers can then interpret this pattern to study the surface crystallographic properties of thin films, even during growth. An illustration of a RHEED system is shown in Figure 1.5. RHEED allows the grower to obtain information such as crystal structure [7-10], relative atomic spacing [11], surface roughness [12, 13], and surface reconstructions [14, 15]. Although the above mentioned analyses are largely quantitative and require a certain level of expertise and prior experience, quantifiable analysis techniques are also available with RHEED. The intensity of the diffracted features in a RHEED pattern has been used to extract growth rate in 2D growth of thin films [16]. An illustration of the correlation between surface coverage and RHEED intensity in the MBE growth of thin films is shown in Figure 1.6.

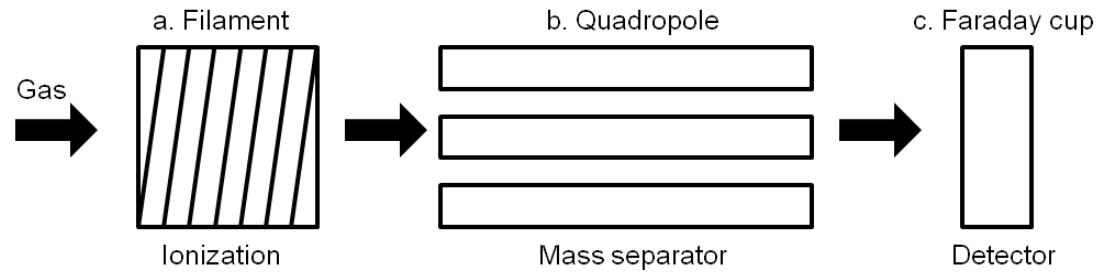

Figure 1.4: Basic components and operation of a residual gas analyzer.

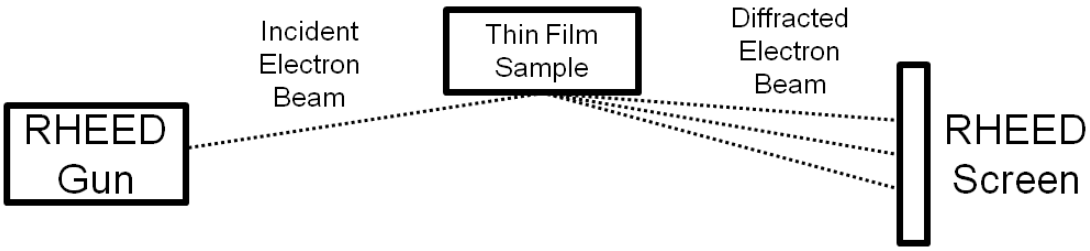

Figure 1.5: Basic components and configuration of a RHEED system in an MBE tool.

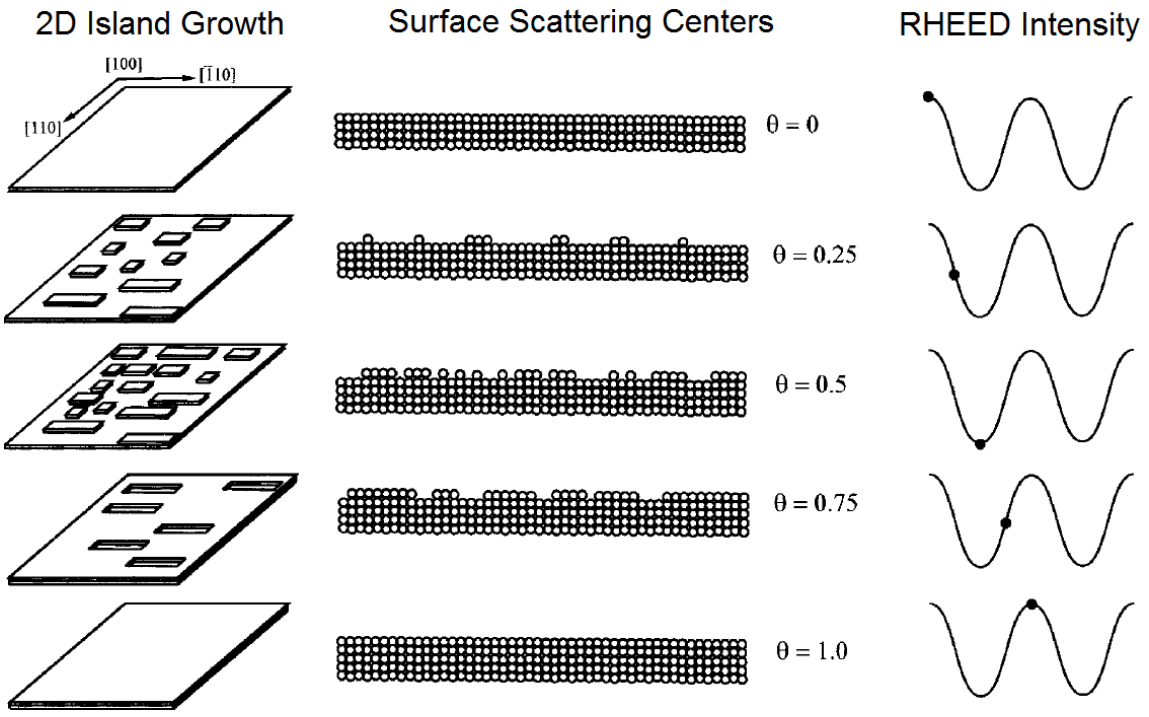

Figure 1.6: Relation between surface coverage, surface scattering centers, and RHEED intensity in 2D MBE growth. From ref. [4].

Aside from 2D growth oscillations shown by Figure 1.6, the time-dependent RHEED intensity has also been valuable in surface kinetics analyses. Due to the scattering caused by an amorphous adlayer [17-19], studies have been performed to determine growth regimes *in situ* [7, 20-22]. By monitoring the effect on RHEED intensity with respect to incoming flux and deposition time, these transient RHEED signatures have also been used to elucidate the growth kinetics in AlN [23, 24], InN [25-27], GaN [7, 28, 29], and InGaN [30, 31]. These studies not only have revealed a new way to study III-nitride growth using tools already available in standard MBE, but have confirmed theoretical work on the stable bilayer [32, 33] and provided new information on mixed adlayers [34, 35].

A popular alternative to molecular beam epitaxy is metal-organic chemical vapor deposition (MOCVD). Group-III elements are supplied by gaseous metal-organic precursors, which allows for plant scalability and fine flux control. These precursors usually require carrier gasses such as N_2 or H_2 because of the relatively high reactor pressure (> 1 mTorr). Ammonia is usually employed to supply active nitrogen, although alternative compounds have been attempted [36-38]. After being carried to the heated substrates, these constituents then dissociate and chemically react to grow the epitaxial film. The pyrolysis of these reactants requires a much higher substrate temperature than MBE (~1,100 °C in MOCVD versus 400-700 °C in MBE). Despite this extremely complex growth chemistry, MOCVD boasts very high material quality and higher growth rates. However, MOCVD is not without issues. The high substrate temperatures needed to crack ammonia into active nitrogen restrict InGaN growth to low indium compositions due to the relative weakness of In-N bonds. Higher growth pressures involved in MOCVD cause gas phase interactions and blurred interfaces between layers in a heterostructures, though the latter can be mitigated by intentionally slowing growth rate. Furthermore, carbon impurities from metal-organic precursors can drastically affect the electrical performance of films grown by MOCVD due to carbon's amphoteric dopant behavior in III-nitrides [39, 40]. In contrast, the low pressures in MBE enable sharp interfaces and have extremely low impurity concentrations, which are very appealing for optoelectronic devices. Advances in MBE growth, yielding higher quality material [23-28] and high carrier concentrations [41-45] at lower substrate temperatures suggest that MBE is the optimal technique for In-containing nitrides.

1.2 Nitride Material System

The III-nitride material system has attracted an enormous amount of interest because of its direct bandgap, outstanding electrical properties, and potential applications in electronic [46, 47], light emitting [48-51], and photovoltaic devices [52-54]. GaN, the most popular nitride binary with a bandgap of 3.4 eV [55], was first synthesized by Johnson and Parsons in 1932 [56]. After the discovery of InN [57] and AlN [58], the nitride material system has become particularly intriguing for use in optoelectronic applications due to its tunable bandgap by forming alloys of the three binaries [59]. The bandgap of InN was recently revised to 0.7 eV [60, 61], which expanded the range of bandgaps achievable by the nitride materials system to span the entire visible spectrum. Shown in Figure 1.7 are the bandgaps of the III-nitride binaries and their respective alloys versus lattice spacing [62].

\

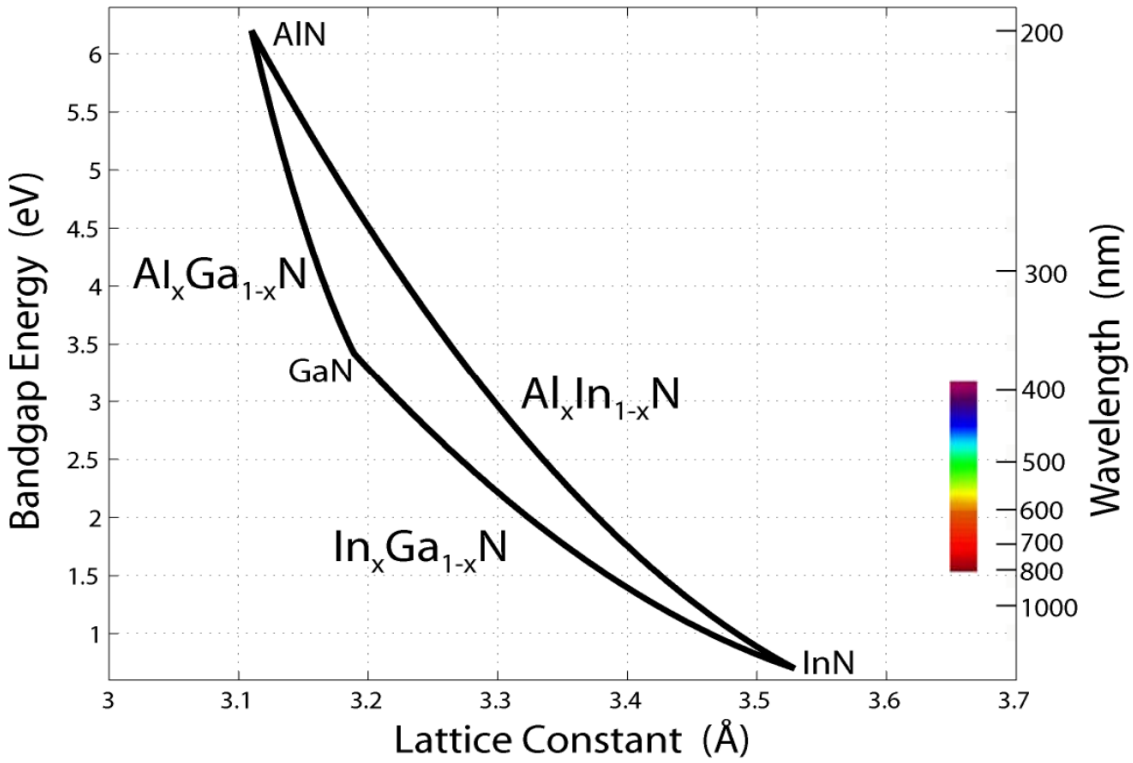

Figure 1.7: Bandgap values versus lattice constant of wurtzite III-nitrides and their respective ternary alloys [62].

The bandgap of a particular III-nitride ternary alloy can be calculated by the equation

$$E_g(A_{1-x}B_x) = (1-x)E_g(A) + (x)E_g(B) - (x)(1-x)C \tag{1.2}$$

where $E_g(A_{1-x}B_x)$ is the calculated bandgap of the alloy, $E_g(A)$ is the bandgap of the first binary, $E_g(B)$ is the bandgap of the second binary, and C is the bowing parameter for the alloy. These bowing parameters differ for each alloy, and are shown in Table 1.1.

It should be noted that bowing parameters often differ between theoretical and experimental results, and calculated bowing parameters can be skewed depending on phase separation in the material. Thus, bowing parameters should be considered rough estimates.

Table 1.1: List of approximate bowing parameters for the group-III nitride alloys [63-65].

	InGaN	AlGaN	InAlN
Bowing Parameter	1.4	1.38	4.7

Common among all group-III nitride compounds is a set of properties that give this material system a broad range of applications. A summary of these properties is shown in Table 1.2 [66-68]. In terms of electronics, high breakdown fields allow III-nitrides to be used for high power electronics [69, 70] while relatively high thermal conductivities [71] allow devices made using these materials to be easily cooled. AlN and GaN have high thermal stabilities [46] due to large bond strengths, affording high temperature operation. The direct bandgap of these materials creates optoelectronic device opportunities. The ability to reach a smaller bandgap than competing electronic materials yields the potential for short wavelength light emission [72], evident in the emergence of violet [50], blue [48, 49], and green [73] nitride emitters. III-nitride alloys have also been noted to exhibit enhanced light emission due to more efficient carrier localization [74], producing efficient light emitters despite high defect densities. Finally, III-nitrides are radiation hard materials [54, 75], enabling device applications in space environments.

Table 1.2: Selected properties of III-nitride binaries, Si, and GaAs [66-68].

Parameter	Si	GaAs	InN	GaN	AlN
Bandgap, E_g [eV]	1.1	1.4	0.7	3.39	6.2
Lattice parameter a/c [Å]	5.4310	5.6533	3.533 5.693	3.189 5.185	3.112 4.982
Breakdown electric field, E_c [MV/cm]	0.3	0.4	1.0	3.3	11.7
Thermal conductivity κ [W/cm K]	1.5	0.5	1.8	1.3	2.7
Dielectric constant, ε	11.8	12.8	9.6	9.5	8.7
Saturated electron drift velocity v_{sat} [10^7 cm/s]	1.0	2.0	2.5	2.5	1.8
Intrinsic carrier concentration n_i [cm^{-3}]	1.5×10^{10}	1.8×10^6	$\sim 10^{13}$	1.9×10^{-10}	$\sim 10^{-31}$

Group-III nitride semiconductors have been shown to exhibit various crystal structures, including wurtzite [67], zincblende [68], and even rock salt [76]. However, wurtzite is the most thermodynamically stable and common crystal structure of the nitrides. Shown in Figure 1.8 is the wurtzite crystal structure.

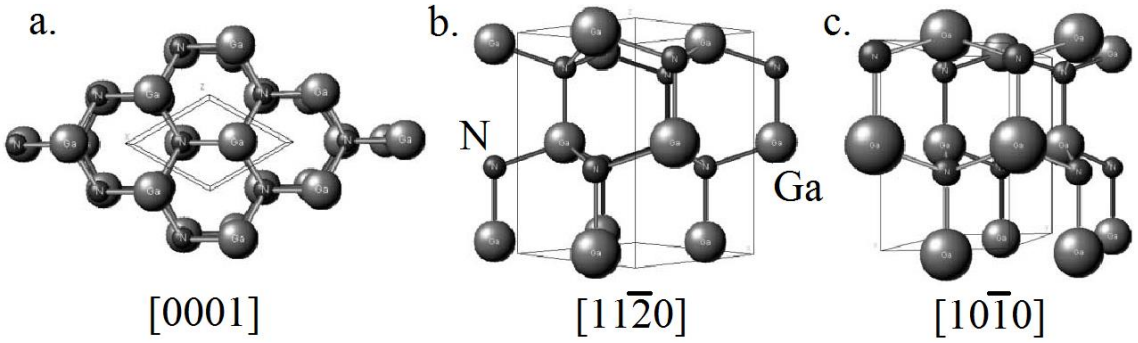

Figure 1.8: Views of wurtzite GaN along various directions: (a) [0001], (b) [1120], and (c) [1010]. The larger grey spheres represent gallium, while the smaller black spheres represent nitrogen.

The lack of inversion symmetry in wurtzite GaN results in a spontaneous polarization of the material. The polarity is determined by the direction of the bonds. In wurtzite III-nitrides, the [0001] direction is faced by metal atoms (Al, Ga, or In) and the opposite direction is faced by nitrogen atoms. The polarity of the material can have a strong effect on both the bulk [77] and surface [78] properties of the film due to differences in growth kinetics [5]. Thus, much effort has been invested into the control of which polarity grows parallel to the growth surface [79-81].

In addition to spontaneous polarization, group-III nitrides also exhibit piezoelectricity, such that a piezoelectric polarization can be created by strain applied to the material. Since piezoelectricity is a reversible property, strain in the material can also be generated by an applied electric field. The spontaneous and piezoelectric polarizations can be summed to produce a net polarization in the material, which can result in extremely large electric fields [82].

The outstanding properties discussed above have made this material system very appealing in a variety of applications. However, there were significant hurdles to overcome in device design and epitaxial growth before this material could be used. Originally considered for optoelectronic devices, the first III-nitride material improvements were made towards the creation of blue light emitting diodes [83]. Early III-nitride crystals suffered from insufficient structural quality, very high background electron concentrations, and low electron mobilities [84] due to large lattice and thermal mismatches between GaN and the chosen sapphire substrate [83]. These faults were dramatically improved upon with the development of a low-temperature AlN buffer layer by Amano et al. in 1985 [85]. After a practical level of material quality was established, efforts were made to obtain p-type GaN. Attempts were made to Zn-dope GaN with little success [86] before using Mg as a p-type dopant [87]. In 1989, low resistivity p-type GaN was achieved [88] by Mg-doping in MOVPE with the use of Cp_2Mg. With the toolset of high crystal quality and doping control, the world's first p-n junction blue/UV light emitting diode was also reported that year [88]. After the development of single-crystal InGaN, the first blue InGaN/GaN quantum well LED was commercialized with an external quantum efficiency of 2.7% [49]. These InGaN layers were relatively defective, and light emission was dominated by lower efficiency donor/acceptor pair transitions instead of band-edge emission. Finally, InGaN material quality was improved by 1995 [89], resulting in drastic increases in LED efficiencies [90] and the emergence of nitride-based LDs [91] and VCSELs [92]. A timeline showing the external quantum efficiencies of GaN-based LEDs correlating with major breakthroughs in III-nitride growth is shown in Figure 1.9.

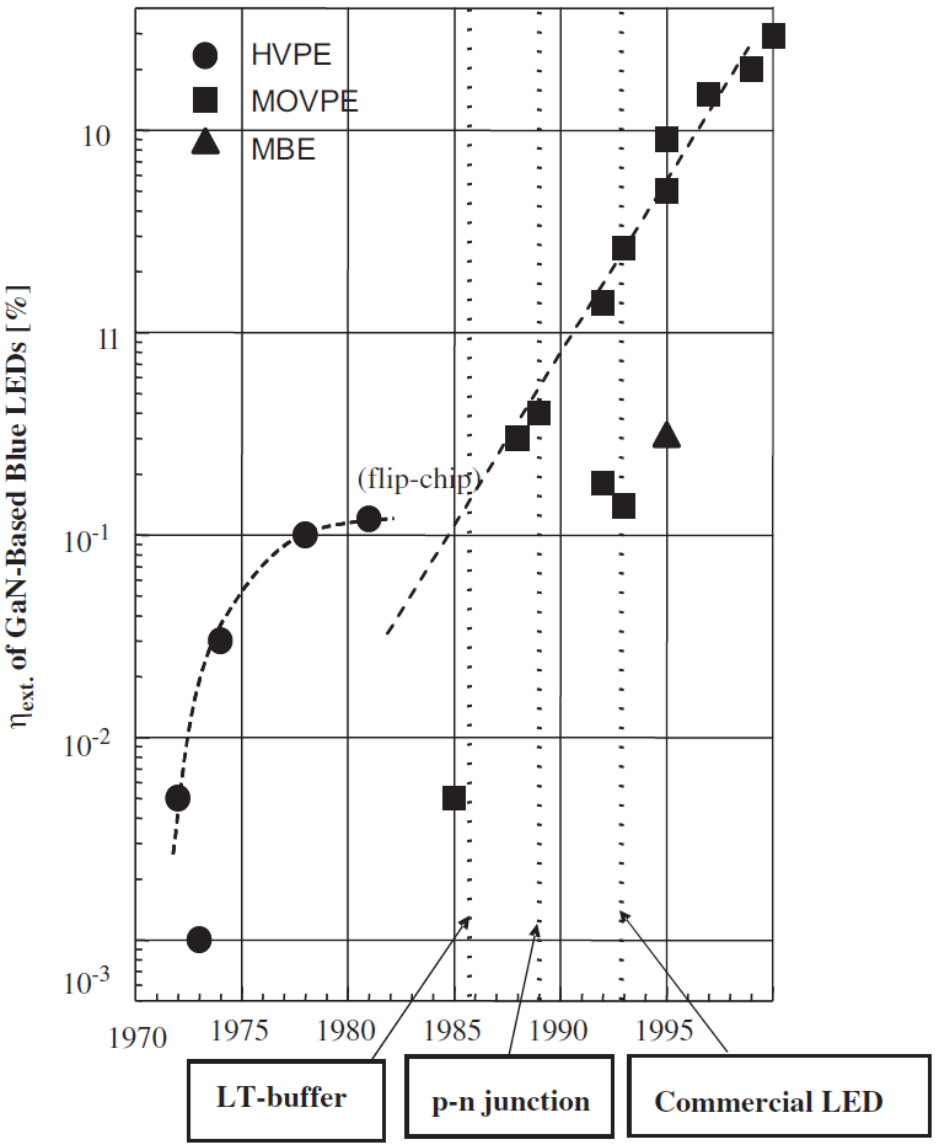

Figure 1.9: Timeline of the increasing external quantum efficiencies of nitride blue light emitting diodes with correlating breakthroughs in material quality and device design.

As these group-III nitride LEDs have been pushed towards higher current densities to compete with conventional incandescent and fluorescent bulbs in area lighting applications, new challenges have surfaced. One of these challenges has been called “current droop” or “efficiency droop”. This phenomenon is identified as a drastic

decrease in external quantum efficiencies of a light emitting diode at higher injection currents [93]. A simulated example of current droop is shown in Figure 1.10. Although easily recognized and very prominent even among extremely high efficiency commercialized LEDs, no general consensus has been reached regarding the source of current droop. Potential causes for current droop have been reported and include Auger recombination [94], defect-related recombination [95, 96], current leakage [97, 98], junction heating [99], carrier spillover/overflow [100, 101], and carrier injection inefficiency [101-103]. Some of the above-mentioned potential causes are interdependent, presenting great difficulty in properly identifying the source of current droop. The issue of current droop is considered an important topic in nitride optoelectronics research, as a solution is needed to allow III-nitrides to be used at high enough efficiencies at high enough current densities for solid state illumination [93].

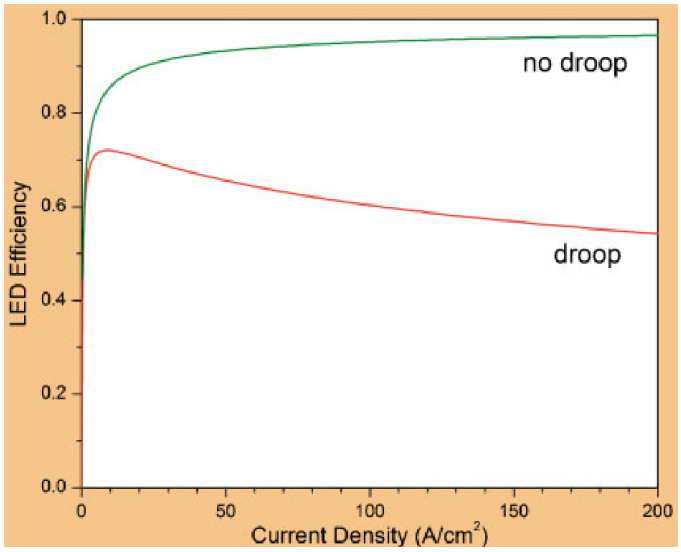

Figure 1.10: Simulated quantum efficiency for an LED with (red) and without current droop (green).

Another challenge in III-nitride device design involves the inherent spontaneous and piezoelectric polarization in the material. Internal electric fields created by polarization can encourage carrier leakage [97, 98] or disrupt carrier transport [104] in situations where it detrimentally affects device performance. More unfortunately, the electric fields generated inside quantum wells can spatially separate electrons and holes to opposite ends of the well, inducing a shift in emission spectrum via the quantum-confined Stark effect [105, 106] and reducing wave-function overlap [107]. To this end, growth along semi- and non-polar axes of nitrides has been explored to either reduce or eliminate these effects [108]. However, this type of growth requires non-standard and potentially very expensive substrates to nucleate the nitride film [109]. Growth kinetics can also change along growth axes different from the (0001) plane [5, 110]. Although still progressing, this technology has the potential to solve a major issue in nitride-based optoelectronics.

Despite the problems with III-nitride LEDs outlined above, spontaneous and piezoelectric polarization has afforded this material system with opportunities in electronics [47]. Since spontaneous polarization differs for each III-nitride binary, increasing in magnitude from GaN to InN to AlN [111], a polarization gradient can be induced in a multi-layer or compositionally graded structure. In the case of a single heterostructures with a smooth, abrupt interface, this polarization gradient occurs across a very small volume between the two layers. Associated with this polarization gradient is a polarization induced charge density, which is compensated by either free electrons or free holes, depending on the sign of the charge density [111]. These charge carriers form a highly mobile sheet of charge, known as either a two-dimensional electron gas (2DEG) or

two-dimensional hole gas (2DHG) [112]. This sheet of charge is the basis of high electron mobility transistors (HEMTs) [82]. Traditional nitride HEMTs, also called heterojunction field effect transistors (HFETs), involve metal-polar growth with an AlGaN layer grown on top of a thick GaN pseudo-substrate [113]. This structure forms a 2DEG at the interface between these layers. In the case of N-polar growth, the sign of the polarity induced charge density is reversed, and a 2DHG can form. Strain-induced piezoelectric polarity can enhance the polarization gradient, such as in the case of tensile strained (0001) AlGaN on GaN. This increases the magnitude of the induced charge density and subsequent carrier gas. An illustration of Ga- and N-polar GaN/AlGaN/GaN double heterostructures are shown in Figure 1.11, with the spontaneous and piezoelectric polarization directions labeled in each layer. Shown in Fig Y are capacitance-voltage profiles of the above-mentioned heterostructures, but also n- and p-doped to illustrate both 2DEG and 2DHG formation. Because of the high breakdown fields and the ability to engineer strain and polarity in III-nitride device structures, this material system has displayed excellent capability in commercialized high-power electronics [46].

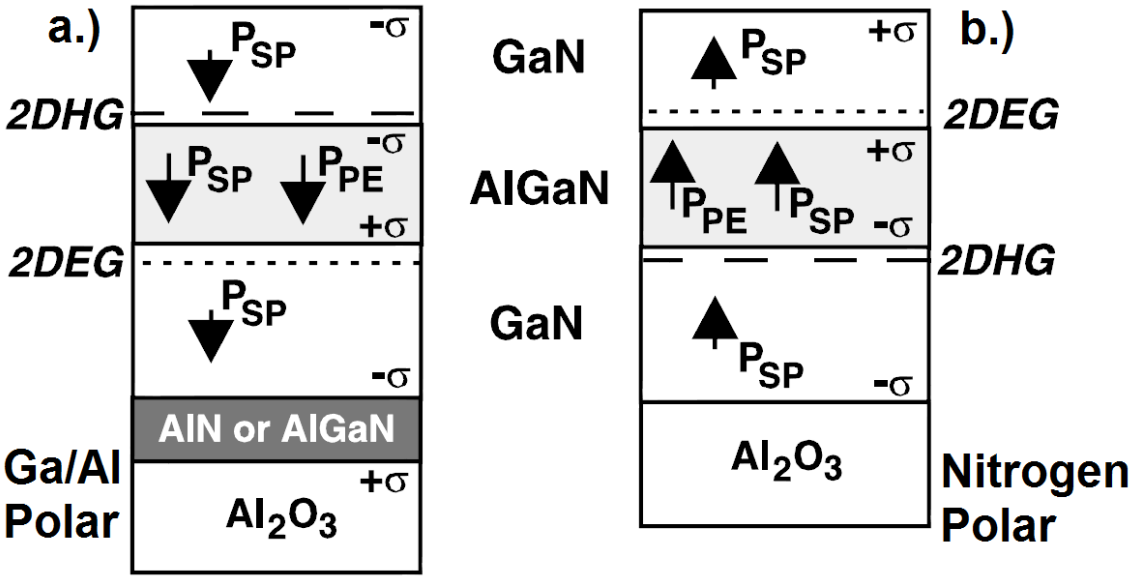

Figure 1.11: GaN/AlGaN/GaN double heterostructures with spontaneous (P_{SP}) and piezoelectric (P_{PE}) polarizations labeled. Ga-polar material is shown on the left (a.) and N-polar material is shown on the right (b.). 2DHG locations are marked in dashed lines, while 2DEG locations are marked in dotted lines. From ref [112].

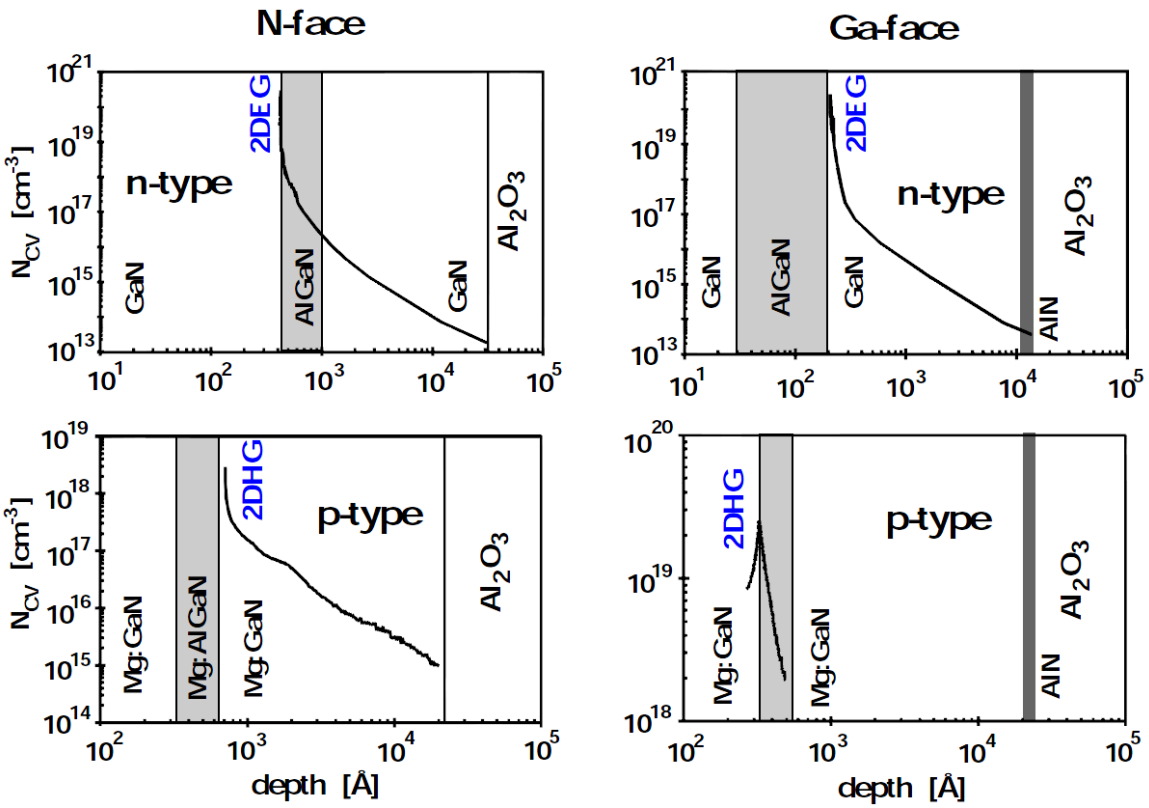

Figure 1.12: Capacitance-voltage profiles of GaN/AlGaN/GaN heterostructures with 2DEG and 2DHG formation locations labeled in blue. The left two profiles were recorded from N-polar material, while the right two profiles were recorded from Ga-polar material. Similarly, the top two profiles were recorded from n-type material, while the bottom two profiles were recorded from p-type material. From ref [112].

1.3 Challenges in III-Nitride MBE for Device Applications

The nitride materials system has an enormous set of potential applications, but several issues with the growth of AlInGaN currently hinder this extraordinary material. There is no lattice-matched substrate for all III-nitride growth, either creating defects in the grown material or requiring expensive and time consuming buffer layers. There is also the issue of phase separation in InGaN alloys, which is critical considering that commercial III-nitride optoelectronics are striving for higher efficiencies in visible-light emitting and photovoltaic devices. Finally, all III-nitrides suffer from low hole concentrations due to the deep acceptor state of Mg, often having to sacrifice material quality in order to achieve practical levels of hole concentrations for devices. These infamous difficulties in growth control, structural quality, and electrical quality of MBE-grown III-nitrides are discussed here.

Currently, there exists no native substrate for III-nitride growth. Inherently, each III-nitride binary has a different lattice spacing, and thus no substrate can be completely lattice matched to all alloys of AlInGaN. Shown in Table 2.1 are popular substrates for III-nitride growth, their respective lattice mismatches to wurtzite GaN, and additional notes regarding further benefits or complications. InGaN LED structures are typically grown by MOCVD on sapphire or SiC substrates which have substantial lattice mismatches to all nitride alloys [67]. The dislocations created by this mismatch are partially mitigated by preparing GaN templates, which annihilate many defects by growing a thick GaN buffer [114]. This technique allows for the growth of thin, low indium content InGaN quantum wells to be grown completely strained and without

relaxation on the thick GaN layers [115]. Although the use of GaN templates only reduces dislocations in GaN for standard ~4 μm buffer layer thicknesses to 10^8-10^9 cm^{-3}, GaN-based LEDs still exhibit very high efficiencies due to localization of carriers in quantum wells [74, 116]. However, higher indium content quantum wells to push light emission further into the green will strain relax, producing more non-radiative recombination centers. This technique provides a solution for violet and blue LEDs, but both lower wavelength emission and more complex structures such as solar cells, HBTs, and laser diodes demand a new approach to substrate InGaN [50].

Table 1.3: A list of popular substrates for group-III nitrides, their respective lattice mismatches to wurtzite GaN, and additional notes citing further benefits or challenges of that specific substrate [67, 117-122].

Substrate	Lattice mismatch to wurtzite GaN	Additional notes
Sapphire	14%	Relatively cheap, requires buffer layer for adhesion/polarity, electrically and thermally insulating
SiC	3.1%	Expensive, electrically and thermally conductive, requires AlN/AlGaN buffer layer for adhesion
Si (111)	17%	Cheap/mature technology, forms amorphous silicon nitride layer upon exposure to reactive nitrogen, simple substrate preparation
$LiGaO_2$	1-2%	Lattice matched to $Al_{0.17}Ga_{0.83}N$, low decomposition temperature, difficult surface preparation, easily etched
ZnO	1.9%	Lattice matched to $In_{0.22}Ga_{0.78}N$, diffusion of O and Zn into GaN at substrate interface
Bulk GaN	0%	Difficult to produce, very expensive, only small wafers available, developing technology

Although there are commonly used methods to circumvent lattice matching issues to utilize InGaN in violet/blue LEDs, there still exist some core material properties that make high-quality, high indium content InGaN difficult to grow. InGaN alloys tend to have some form of phase separation through three main processes: thermal decomposition, spinodal decomposition, and indium surface segregation.

Thermal decomposition must be considered for all growth of group-III nitride materials, but is particularly troublesome for InGaN [19]. The bonds between indium and nitrogen are weaker [123] than that of gallium and nitrogen, so less energy in the form of heat is required for the bonds to break. This property is predominantly inconvenient in MOCVD growth, where elevated temperatures required to crack ammonia into nitrogen prohibit growth of high-indium content InGaN [124, 125]. Higher substrate temperatures during InGaN growth have been shown to dissociate In from the InGaN alloy, leaving excess indium metal on the surface [126]. The effect of substrate temperature on maximum indium content of InGaN grown by MBE is shown in Figure 1.13. A reduction in growth temperature by any growth method reduces material quality [124], as less energy is supplied to reactant atoms to find an optimal location in the crystal lattice. Thermal decomposition thus encourages the search for a growth method to be able to grow high-quality nitride materials at low temperature [127].

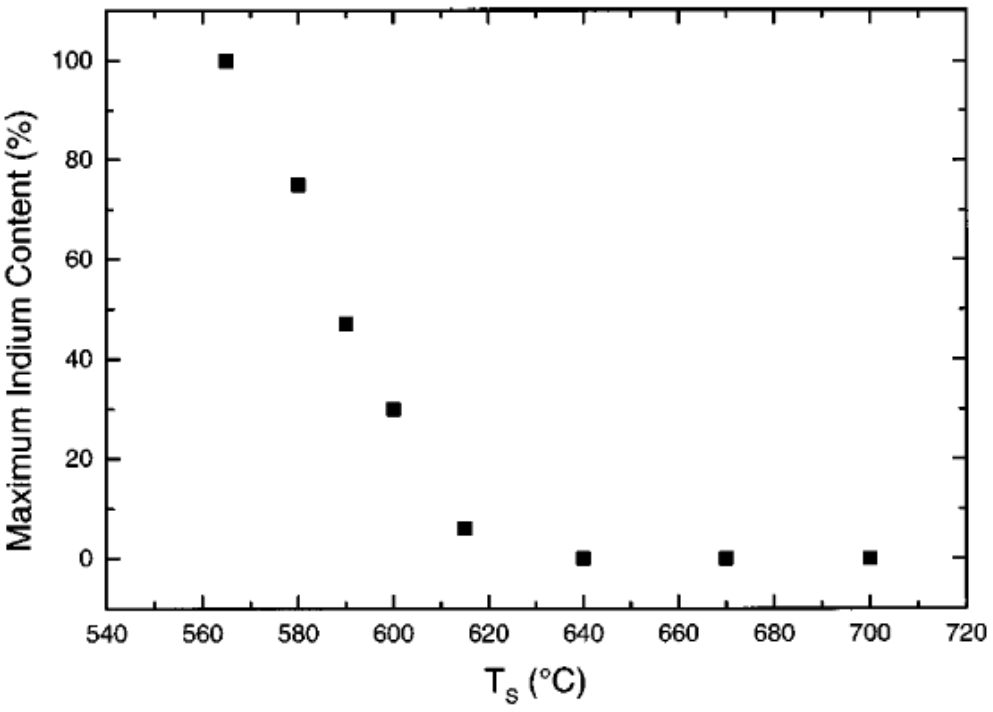

Figure 1.13: Maximum indium content of InGaN grown in nitrogen-rich MBE versus substrate temperature, displaying thermal decomposition of InGaN and InN at higher temperatures [19].

InGaN alloys have a region between InN and GaN such that, at certain temperatures and indium compositions, there is no energy barrier for phase separation. This complex phenomenon known as spinodal decomposition is described more in depth elsewhere [116], and can cause both minor indium compositional fluctuations as well as two completely separated, more energetically favorable phases. Shown in Figure 1.14 are TEM images of a quantum well before and after an anneal, displaying phase separation via spinodal decomposition. Spinodal decomposition seems most unfortunate considering the effort to grow homogeneous InGaN alloys, however recent reports [74, 116, 128] have shown that small amounts of phase separation in InGaN LEDs in fact

drastically enhance light emission. The benefits arise in providing localized radiative recombination centers in denser concentrations than dislocations, which provide non-radiative recombination centers. The benefits of spinodal decomposition regrettably end there, as more complex structures such as solar cells and laser diodes [50] demand both smooth band structures and very low dislocation densities. It should be noted that spinodal decomposition is considered a kinetically limited effect [116], occurring primarily on the surface as bulk diffusion in nitrides is very low. Increased growth rates are looked to as a potential solution, and have been met with some success [30, 129].

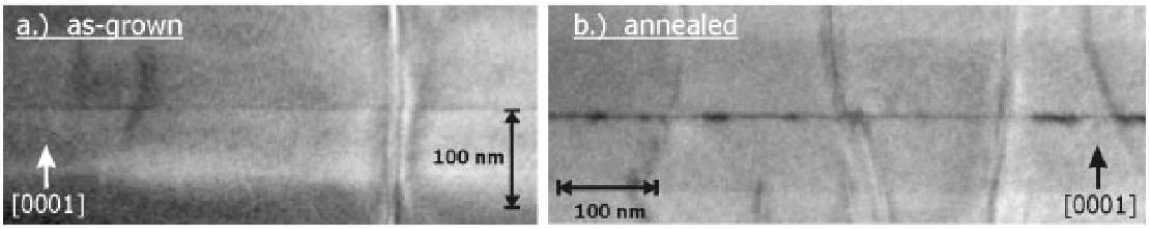

Figure 1.14: Cross sectional TEM images of an InGaN quantum well before (a.) and after (b.) an anneal. After the anneal, the InGaN phase separates via spinodal decomposition into more energetically favorable clusters [130].

Finally, there is the issue of indium surface segregation, which is perhaps the most disruptive of natural limitations of the nitride materials system. Indium surface segregation has been described as the tendency for indium atoms to preferentially migrate vertically [19, 131] along the growth front and laterally [132, 133] across the film during the growth of InGaN [132], InGaAlN [131], and InGaAs [134] alloys.

Vertical indium surface segregation has been explained by a competition between indium and gallium on the film surface, where it is more energetically favorable for gallium atoms to occupy surface sites [135]. The vertical surface segregation of indium has been shown to result in a decrease in indium incorporation [136] and blurring of InGaN/GaN interfaces in quantum well growth [137, 138]. The effect of indium surface segregation on multiple-quantum-well structures is shown in Figure 1.15. Vertical inhomogeneities in quantum wells negatively impact light emission due to wider well width [131], which causes poor electron-hole wave function overlap.

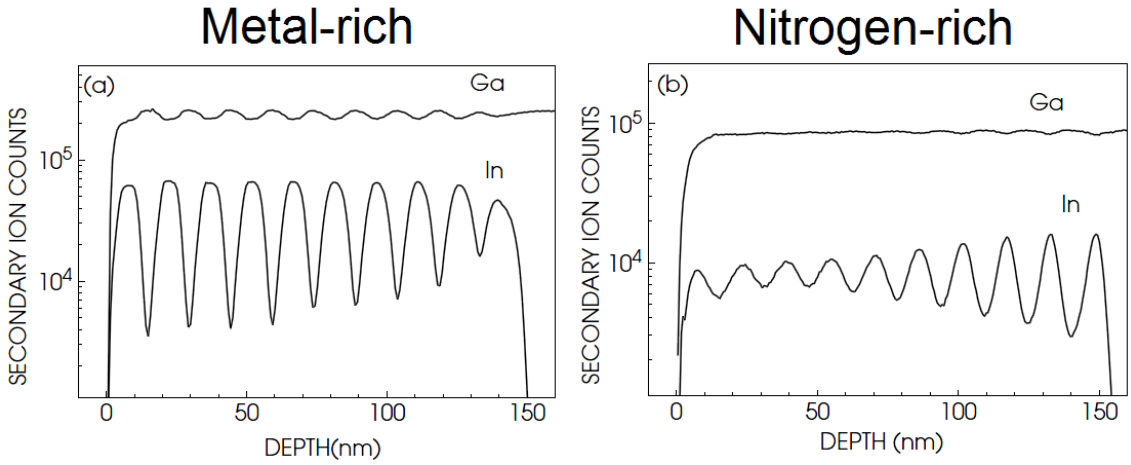

Figure 1.15: SIMS profiles performed on InGaN multiple-quantum-well structures grown in metal-rich (a) and nitrogen-rich (b) MBE. In the metal-rich case, indium surface segregation occurs, which widens the quantum wells, increasing spatial separation of electrons and holes.

Lateral segregation of indium has been explained by the higher stability of In-In bonds than In-Ga bonds [133], encouraging indium to laterally aggregate [139] into islands if given enough time and mobility on the surface. This migration of indium adatoms into clusters on the growing surface has been shown to produce indium-rich nanostructures within the film [132]. Conversely to the case of vertical indium surface segregation, lateral surface segregation has been shown to drastically increase light emission from indium-bearing materials [140]. The quantum-dot-like nanostructures created from this form of indium surface segregation has been shown to enhance spatial carrier localization, producing radiative recombination centers [74]. Indeed, this prominent form of phase separation in InGaN alloys has been hailed as the very reason group-III nitrides have greater LED efficiencies and lower sensitivities to threading dislocations than the phosphide and arsenide materials systems [50]. Although beneficial for LEDs and laser diodes, lateral surface segregation of indium is detrimental for nitride solar cells, where recombination of carriers must be minimized. A need then emerges for an ability to not only observe, but control indium surface segregation to utilize the outstanding qualities of the nitride materials system for both light-emitting and photovoltaic applications.

Indium-rich conditions have been used in the growth of AlGaN [141], GaN [33],\ and InN [25], where indium adlayers have proven to be useful as a surfactant without affecting material compositions. However, for the case of InGaN, excess indium accumulation has a drastic effect on indium incorporation [132, 135, 139]. At the temperatures generally used for InGaN growth, metallic indium has been shown to be difficult to remove from the growth surface *in situ* [131] without risking heat-induced

phase separation [130] of the InGaN alloy. Suppression of indium surface segregation has historically been achieved by the use of nitrogen-rich growth conditions [19, 33, 124], which prohibit a metal adlayer from accumulating on the growing surface. Unfortunately, nitrogen-rich growth conditions result in a reduction in material quality [12] and surface smoothness [137].

Stoichiometric growth conditions would maximize crystal quality and surface smoothness in cases where metal adlayers cannot be accumulated. Such conditions are prohibitively difficult to achieve uniformly across large wafers at temperatures used for InGaN growth where an intermediate regime does not exist [12]. Thus, considering the above list of limitations associated with the growth of high-quality, single-phase InGaN, a new approach to InGaN growth and *in situ* control is needed.

The challenges of p-type doping in GaN are numerous. The optimal growth conditions for high p-type doping in GaN are nitrogen rich, which allows for Mg to occupy a Ga substitutional site [142]. However, these conditions result in rough surface morphologies and high defect densities [20]. Conversely, Ga-rich growth results in compensating nitrogen vacancies and reduced hole concentrations [143], even though it yields smooth surface and higher crystalline quality [12]. Mg has also been shown to cause inversion domains, changing the polarity of the nitride film from Ga-polar to N-polar [144]. Furthermore, the high Mg activation energy of 160-170 meV [145, 146] for both MBE- and MOCVD-grown layers results in a very low Mg activation efficiency, even though the concentration of Mg atoms may be high.

There have been some successes in improving hole concentration in Mg-doped GaN for use in optoelectronics. Bhattacharyya *et al*. demonstrated a hole concentration

of 3×10^{18} cm^{-3}, [147] but at high substrate temperatures where adatom desorption can make precise growth conditions difficult to produce. McLaurin et. al. was able to achieve a hole concentration of 7.5×10^{18} cm^{-3} [148, 149] in m-plane GaN and attributed this success to the absence of inversion domains in the non-polar growth front. Although promising results, the hole concentrations found in recent literature still have not approached the levels needed to realize GaN-based high-efficiency LEDs used in solid-state lighting or tunnel junctions for multi-junction solar cells. It then becomes clear that drastic changes in growth procedure and understanding are warranted.

CHAPTER 2: Transient Atomic Behavior and Surface Kinetics of GaN

2.1 Introduction

The growth of III-nitrides, especially gallium nitride (GaN), by molecular-beam epitaxy (MBE) has been the subject of intense research because of their unique properties for use in electronic and optoelectronic devices [46, 67, 150]. The wide, direct bandgap of GaN, which can be adjusted by forming solid solutions with other III-Nitrides, makes it a promising candidate for light-emitting diodes [48, 51], laser diodes [83], and solar cells [151]. The high breakdown voltage and high electron saturation velocity of III-Nitrides have an advantage in the field of high-frequency and high-power devices such as high electron mobility transistors [47, 82, 152].

A modified epitaxy technique, metal modulated epitaxy (MME), has been introduced and implemented in plasma-assisted MBE systems which has produced marked improvements in several areas of material quality in aluminum nitride [23, 24] and gallium nitride [44, 45]. MME involves the periodic and simultaneous shuttering of metal (Al, In, Ga) and dopant (Mg and Si) cells while maintaining a constant nitrogen flux. Additionally, the fluxes used during MME are excessively metal-rich, which allows the exploitation of the surface smoothing effect [12, 13, 20-22] of the laterally contracted Ga bilayer [32]. Atomic force microscopy (AFM) of step-flow growth achieved by MME at moderately low temperatures is shown in Figure 2.1. This epitaxy technique avoids droplet buildup by incorporation of residual Ga on the surface during

the Ga-shutter closed period, and is further explained in this study. The Ga bilayer has also been shown to exhibit a migration enhancement effect [33], which allows nitrogen adatoms to reach optimal locations in the crystal lattice, even at low temperatures. The lower substrate temperatures ($\leq$ 650 °C) involved in this growth technique allow higher uniformity, better reproducibility as a result of less variation in (or even elimination of) adatom desorption, lower heater induced outgassing of carbon monoxide related components, and the utilization of more sensitive substrates. The MME technique has also been shown to expand the threshold of p-type doping more than an order of magnitude past previously accepted experimental limits [44, 153], previously demonstrating p-type GaN with a hole concentration in excess of 1×10^{19} cm^{-3}. With further development, a hole concentration of 4.3×10^{19} cm^{-3} in p-type GaN was achieved, indicating that MME provides a promising technique for growing unique devices currently bottlenecked by low hole concentration.

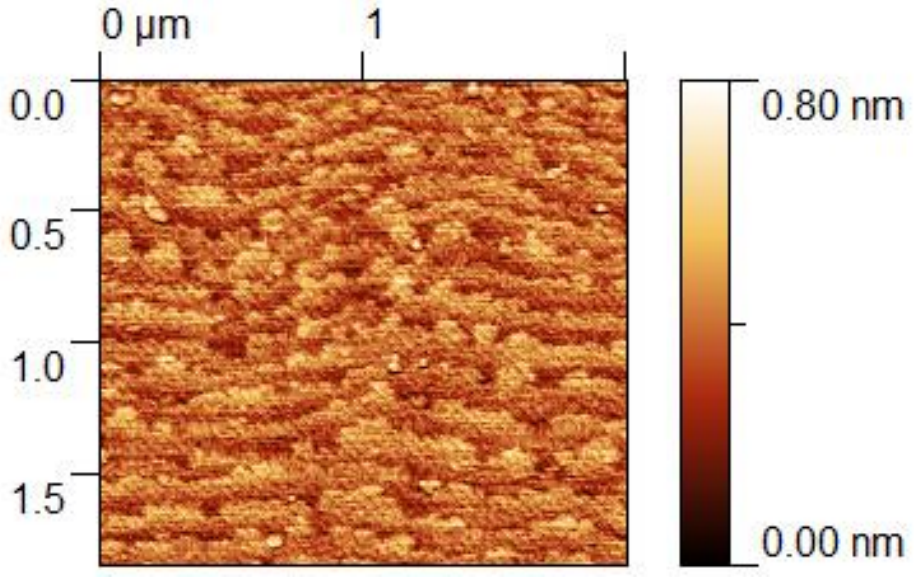

Figure 2.1: Atomic-force microscopy of step-flow growth achieved by MME.

Other groups have employed similar shuttered growth methods, some towards the same goal. Interrupted growth epitaxy (IGE), developed by Munasinghe *et al*., modulates the Ga shutter while growing in the nitrogen regime [154], which increased the number of optically active rare earth ions in the GaN film but was performed under nitrogen rich conditions. MME differs from IGE primarily in the excessive metal richness of the MME approach, which employs 2 to 4 times the normal metal fluxes needed for non-shuttered stoichiometric growth. Poblenz *et al*. developed a very long period, shuttered MBE technique such that Ga and N are modulated simultaneously [155], taking advantage of the high mobility of the adatoms in the Ga wetting layer and preventing droplet buildup by allowing excess Ga to desorb when both shutters are closed. Metal-rich Ga fluxes similar to MME are used in this method, but shutter cycle times were reported as several minutes whereas in MME they are a few seconds. Additionally, MME uses the delivery of a constant Nitrogen flux to consume the excess Ga, essentially eliminating the need for high substrate temperatures and maintaining a growth rate up to ~90% of the non-shuttered growth rates, 1.0-1.3 μm/hr in the present case. This last difference is critically important for commercial use of any shuttered growth method as MBE already suffers from low growth rates compared to competing technologies. Finally, the lower substrate temperatures used in GaN MME differ sharply from the technique proposed by Poblenz *et al*. [155]. This feature and the quick transitions from droplet to nitrogen-rich surface phases during shuttering with minimal time spent in the intermediate regime results in more uniform accumulation of Mg. This is attributed to the segregation of Mg to the surface, not accumulating at pitted nucleation sites which are known to result from intermediate-regime growth [13]. This more uniform incorporation

of Mg results in higher electrically active Mg concentrations, reduced defect compensation and higher hole concentrations in excess of 4×10^{19} cm^{-3}.

Reflection high-energy electron diffraction (RHEED) is traditionally used to characterize the surface of crystalline materials and detect *in situ* growth rate from intensity oscillations caused by constructive and destructive interference in unshuttered growth [16]. However, transient RHEED signals have been investigated by Daudin *et al.* and associated with adatom behavior during growth [156]. Adelmann et. al. demonstrated the usefulness of RHEED for determining the surface phase of GaN and showed that RHEED could be used to identify transient kinetic behavior of adatoms. RHEED transients have also been shown to provide information about growth regime when combined with MME [23].

The objective of this study is to expand upon the *in situ* analysis of GaN by investigating transient RHEED signals resulting from shutter transitions, and to develop a model for transient atomic behavior on the surface of GaN is developed. This model both supports previous theoretical models [21, 32, 33, 78, 156] of the Ga bilayer and provides new insight to the surface kinetics of GaN, particularly the formation and depletion of a nitrogen adlayer.

2.2 Experimental Setup

All growths for this study were conducted in a Riber 32 MBE system equipped with a Veeco SUMO effusion cell for gallium (Ga) and a standard Veeco effusion cell for aluminum (Al). Nitrogen is supplied by a Veeco-unibulb nitrogen source operated at 350 W with a constant flow rate of 1.3 sccm for all growths. A Stanford Research Systems RGA200 was positioned facing the substrate for desorption mass spectrometry (DMS) measurements during growth. Since the enormous signal of nitrogen at mass 28 saturated the residual gas analyzer, the smaller nitrogen shoulder signal at mass 27 was used. It was verified herein, as was done elsewhere [23], that the mass 27 signal exactly traced the mass 14 atomic nitrogen signal, but supplied a larger signal convenient for observation. GaN films were deposited on c-plane lithium gallate (LGO) and c-plane sapphire. All substrates were backside sputtered with 1.5 microns (μm) of tantalum (Ta), to promote efficient and uniform heating. All Ga and Al shutter modulation schemes were 10 seconds open, 10 seconds closed, unless otherwise noted. For this study, the active closed loop control method previously reported [43] for MME was not employed so that steady conditions could be maintained.

For the growth of GaN on lithium gallate substrates, custom polishing was performed to achieve an RMS roughness of ~1-2 Å. Following polishing, the substrates were solvent cleaned (trichloroethylene, acetone, methanol) in a 6-cycle sonic bath. Substrates were dried with nitrogen before being loaded into the introductory chamber where they were outgassed at 300 °C for one hour before being transferred into the growth chamber. A 30 nm thick N-rich GaN buffer layer was grown at a substrate

temperature of 600 °C using an un-modulated Ga flux of 1.5×10^{-7} Torr beam equivalent pressure (BEP). After the buffer layer was deposited, a modulated Ga-rich bulk GaN layer was grown.

For the growth of GaN on sapphire, the substrates were cleaned in a hot piranha etch, which was a 4:1 mixture of H_2SO_4:H_2O_2 heated to 90 °C. After cleaning, the substrates were rinsed in DI water, dried with nitrogen, and loaded into the introductory chamber. The substrates were then outgassed at 300 °C for one hour and loaded into the growth chamber. The substrates were exposed to a nitridation process, which consisted of exposure to 1.3 sccm of nitrogen at a substrate temperature of 300 °C for 30 minutes [157-161]. A 140 nm AlN buffer layer was then deposited using a metal modulated Al flux of 4.9×10^{-7} Torr BEP [161, 162]. A modulated Ga-rich GaN bulk layer was then grown on top of the AlN buffer layer.

LGO was used as a substrate because of its proven ability to generate atomically flat GaN even at low temperature, which facilitates a tool for exploring the low temperature surface kinetics of GaN. LGO has a very small biaxial lattice mismatch to GaN of 0.9-1.9% [121, 163-167] at room temperature. These properties result in elastically strained buffer layers allowing Stranski-Krastanov buffer layers instead of the normal island nucleation [168]. A comparison of properties for technologically important substrates in the growth of GaN is shown in Table 2.1.

Table 2.1: Properties of significant substrates for the growth of GaN

Substrate	Lattice mismatch to GaN	Thermal Conductivity at 300K (W/mK)	Bandgap (eV)
$LiGaO_2$	0.9-1.9% [121, 163-167]	17 [169]	4.4-5.6 [170]
6H-SiC	~3.5% [171]	490 [171]	3.02 [67]
Sapphire	~13% [171]	46 [171]	8.1-8.6 [67]

Ga-rich GaN was grown on LGO at various substrate temperatures and Ga fluxes and monitored with RHEED during growth. Ga fluxes ranged from 7×10^{-7} to 1.2×10^{-6} Torr BEP, at intervals of 1×10^{-7} Torr, grown at temperatures of 650, 600, 550, and 500 °C. For comparison, the Ga flux which unmodulated growth formed droplets observed at the end of growth is approximately 4.5×10^{-7} Torr BEP indicating a substantial Ga-rich growth condition during the shutter open half cycle. During this study, temperature was decreased linearly, while Ga fluxes were randomly visited to minimize systematic errors associated with substrate roughening at lower Ga flux. It is important to note that smooth RHEED images are required for this analysis, which demands that the growth surface be sufficiently planar. Spotty RHEED images often results in inconsistent behavior because of the tendency of intensity data being dominated by surface scattering on rough surfaces rather than intrinsic behaviors described herein. Metal-modulated epitaxy of AlN and GaN described in this report provide sufficiently smooth surfaces such that (2 x 2) reconstructions are often observed during growth, indicating an atomically flat surface [172]. The excessively metal-rich conditions used in this study consistently produce

smooth RHEED patterns and are sufficient to produce a starting point for monitoring RHEED intensity.

To observe relationships between RHEED transients and growth rate, three growths of GaN on LGO were performed at a substrate temperature of 600 °C using Ga-rich Ga fluxes of 8×10^{-7}, 1×10^{-6}, and 1.2×10^{-6} Torr BEP. To show compatibility with more conventional but less convenient substrates and to study the effects of more extreme modulation, one growth of GaN on sapphire was performed at a substrate temperature of 600 °C using various Ga-rich Ga fluxes and shutter modulation schemes. Additionally, all p-type GaN results reported herein are on sapphire.

In order to monitor the variations in RHEED intensity, a photodiode amplifier circuit was constructed with a Texas Instruments OPT101P photodiode and mounted flat against the fluorescent RHEED screen during growth. The photodiode was placed directly on top of the main RHEED streak as possible to maximize the signal to noise ratio. The output voltage of the photodiode was sampled at a frequency of 5Hz in all modulated Ga-rich growths for consistency of results although a higher sampling rate is possible.

2.3 Kinetic Analysis of GaN MME via RHEED and RGA

Although RHEED can provide information through reconstruction patterns [17], it can also provide information in the intensity of the different components of the pattern. Shown in Figure 2.2 are RHEED intensity variations from GaN grown on LGO at a constant temperature with varying Ga fluxes. Several consistent trends and flux-dependent traits are immediately apparent. Before the Ga shutter is opened, only nitrogen is impinging on the sample, and the RHEED intensity increases with a relatively constant positive slope. Immediately after the Ga shutter is opened, there is an abrupt increase, followed by a subsequent decrease in intensity. The RHEED intensity continues to decrease as a concatenation of two flux-dependent exponential decay functions until it reaches a saturation point, where the intensity decreases much more slowly. After the Ga shutter is closed, there is a dose-dependent delay before intensity rapidly increases to a local maximum, and then decreases slightly again to the initial, increasing region.

The intensity of a RHEED signal can be influenced by several factors. Traditionally, RHEED oscillations have been primarily interpreted to result from constructive and destructive interference between layers of differing heights in a growing film [16]. However, for GaN grown by MME, the interpretation of RHEED is a more complex compilation of many separate mechanisms. Under nitrogen-rich GaN growth conditions, three-dimensional growth preferentially occurs, and smooth RHEED streaks slowly transition to a series of spots. The intensity of the streak will be focused into the spots, slowly increasing the local intensity of the screen at a spot. Additionally, the

electron density of physically adsorbed (physisorbed) layers will affect the intensity of the RHEED signal. Physisorbed layers with higher electron densities (Ga in this case) will reflect more of the incoming electron beam than a lower electron density layer (N in this case) [18]. Another mechanism for reduced RHEED intensity is when the crystalline surface is covered in an amorphous layer which will scatter the incoming electron beam. This is commonly observed for thin oxides on GaAs, Si and other surfaces [17, 18]. In the case of GaN, a chemically adsorbed (chemisorbed) monolayer or bilayer of amorphous Ga atoms will dampen the RHEED intensity by a magnitude proportional to the thickness and surface coverage of the adsorbed layer(s). Finally, if enough chemisorbed Ga atoms accumulate on a surface, the Ga will form into three-dimensional droplets and physically block the electron beam, further decreasing RHEED intensity. This behavior is identical for AlN [14, 23, 24].

To qualify these transient signals, two fluxes were examined further which exhibited all of the aforementioned features. Shown in Figure 2.3 are two detailed modulation cycles with Ga fluxes of 7×10^{-7} and 1×10^{-6} Torr BEP. More detailed features are more easily visible in the lower flux case, but a higher flux must also be examined since some features, most notably the features we ascribe to droplet formation and consumption, did not occur in the lower flux case for the selected modulation scheme. Illustrations describing the physical mechanism for each feature labeled in Figure 2.3 are shown in Figure 2.4.

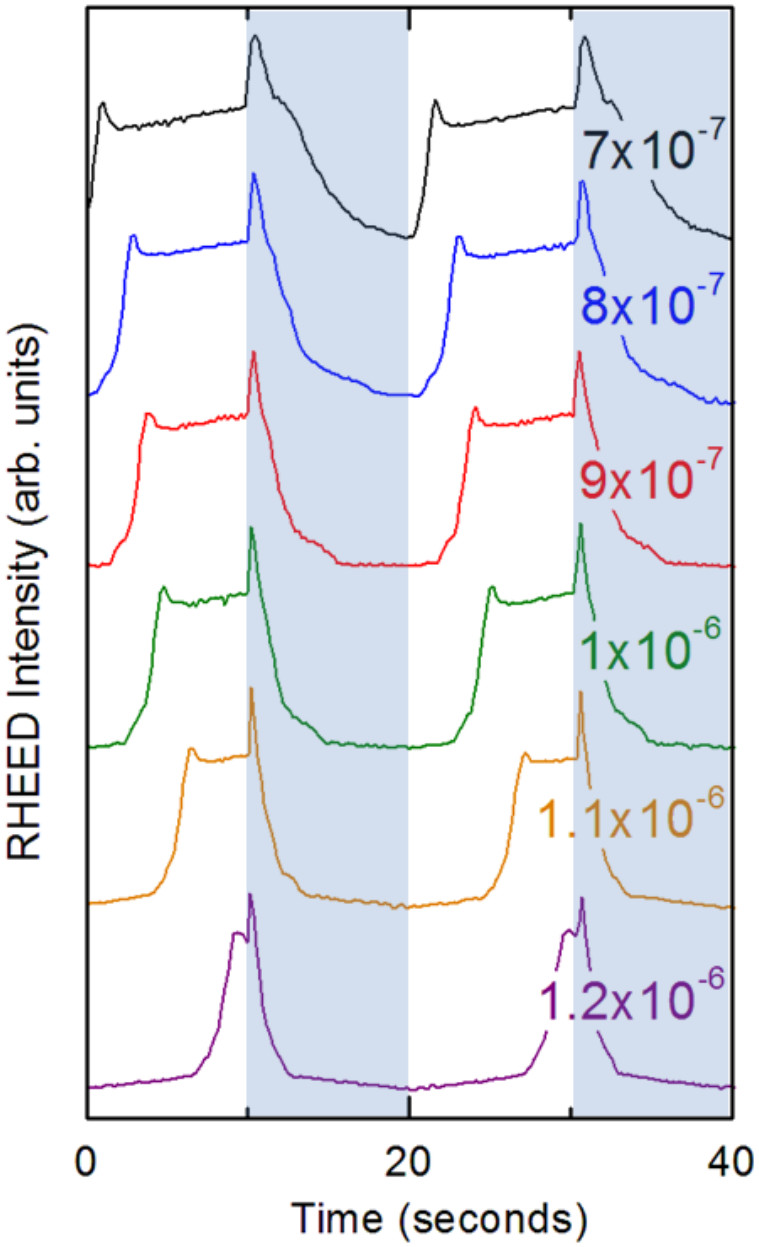

Figure 2.2: Transient RHEED signals for a variety of metal-rich Ga fluxes (shown on the right). Shaded regions indicate Ga shutter open portion of the modulation scheme.

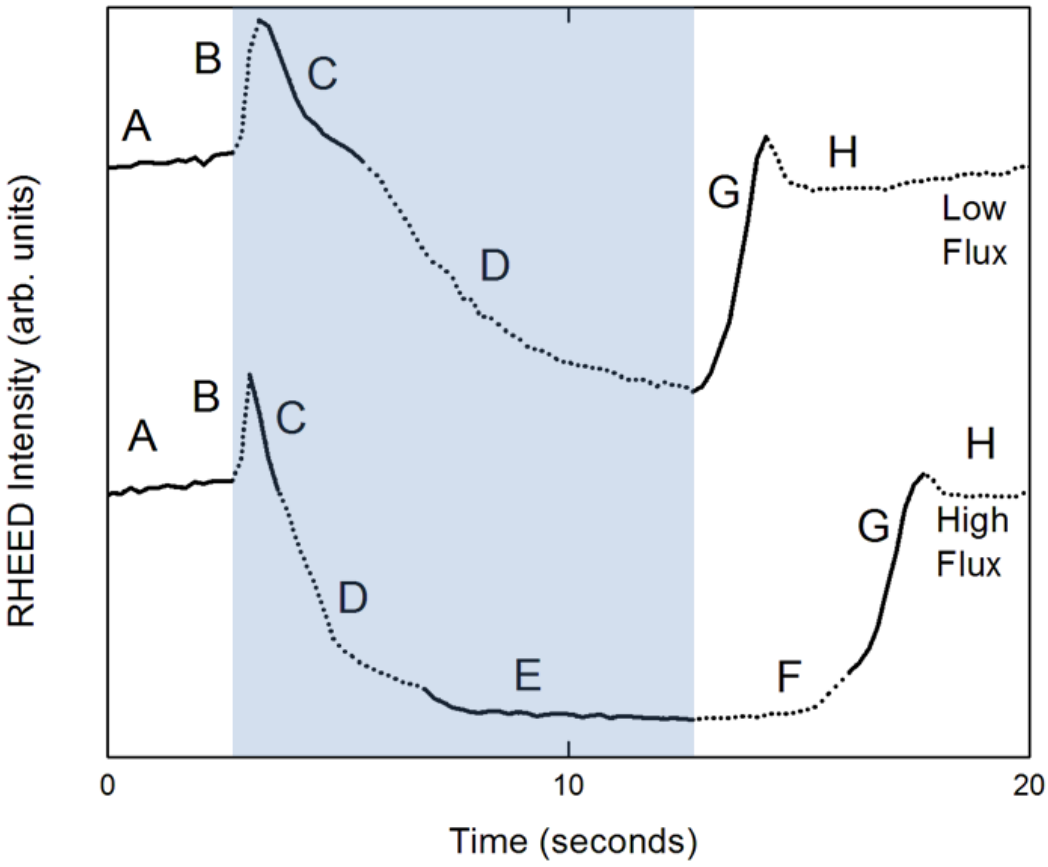

Figure 2.3: Detailed view of two representative transient RHEED signals for low and high Ga flux conditions. Features are labeled and shaded region indicates Ga shutter open portion of the modulation scheme.

Feature A refers to the region of slow intensity increase before opening of the Ga shutter, which is assumed to be a dampened signal attributed to an adsorbed N layer on the GaN surface. The gradual increase in signal intensity during Feature A is believed to be slow consolidation of the RHEED streak into a spot as a result of roughening of the surface during the nitrogen-rich growth condition. Immediately after opening of the Ga shutter, a significant increase in the RHEED intensity is observed as shown in Feature B, which is attributed to the exchange of physisorbed nitrogen with a higher-electron density physisorbed gallium layer and thus, higher electron reflectance. Although the shutter

modulation scheme used for detecting RGA signals in a separate growth was much longer, this exchange in adsorbed nitrogen when the Ga shutter is opened is visible when monitoring mass 27, as shown in Figure 2.5 and described previously for Al and N in AlN growth [23]. It is important to note that the transient time constants in the detected RGA signals were much larger than that of the RHEED. At a growth pressure of 1.5×10^{-5} Torr BEP, which is not fully in the molecular flow regime, desorbed nitrogen from the GaN surface causes a slow change in the background chamber pressure. The relatively high growth pressures and nitrogen pumping speed limitations result in a much slower recorded effect in the RGA of mass 27. As was performed elsewhere [23], an RGA signal at mass 40 was also observed to be independent of shutter transitions indicating no measureable thermal load on the chamber while shuttering of the hot effusion cell.

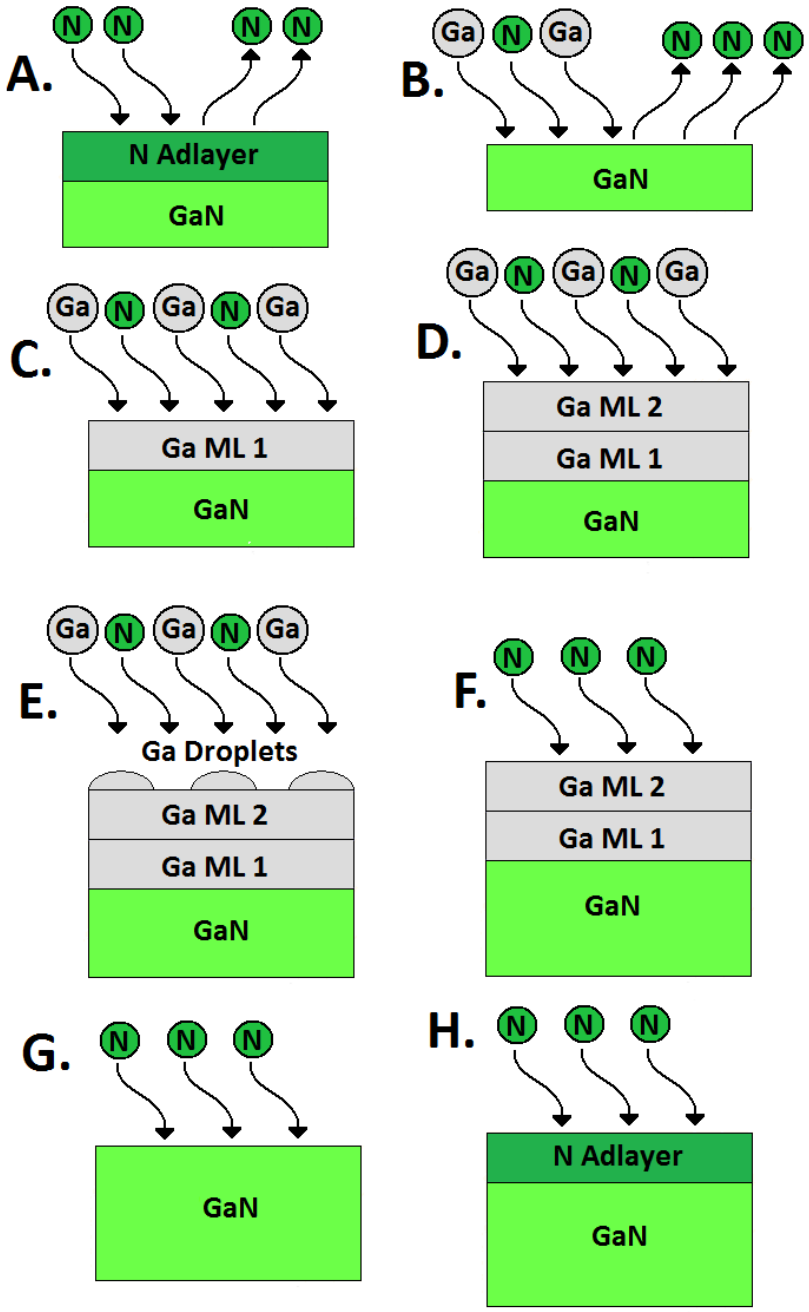

Figure 2.4: Illustrations of the surface behavior during growth of GaN in each feature labeled in Figure 2.3.

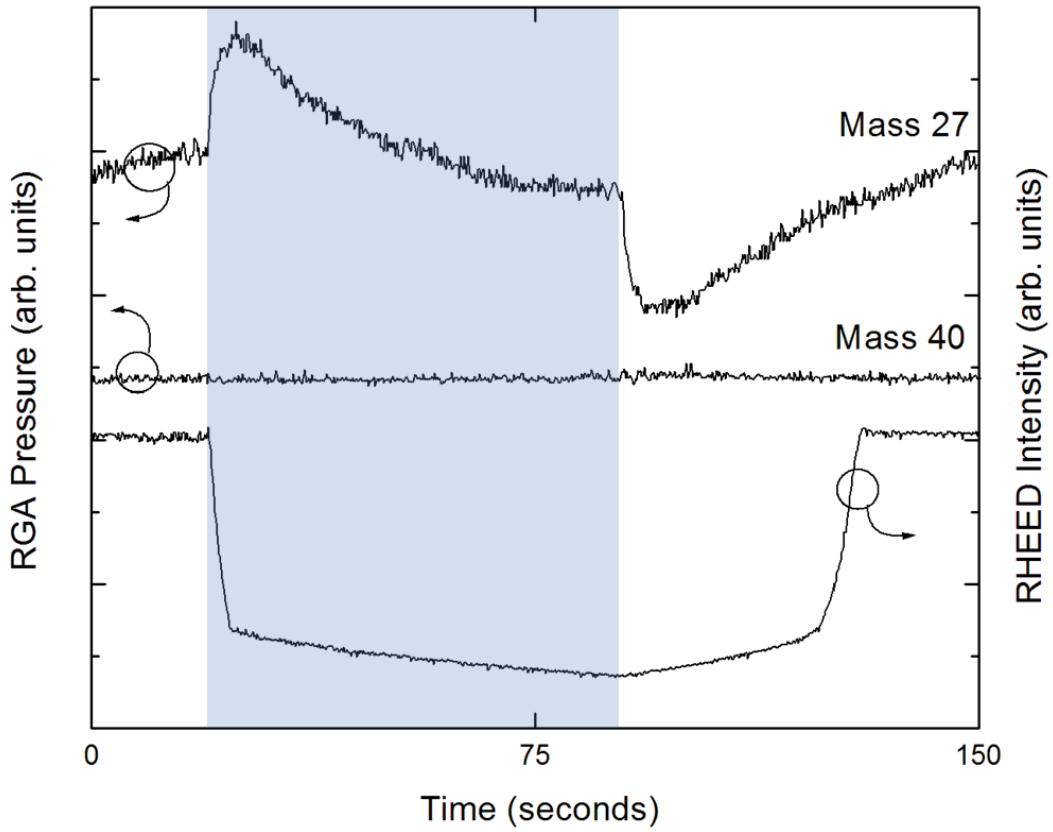

Figure 2.5: RGA signal of mass 27, which mimics nitrogen. Shaded region indicates Ga shutter open portion of the modulation scheme. Note that the partial pressure of mass 27 tends toward a lower pressure when Ga shutter is open, indicative of the nitrogen consumed during GaN growth.

After reaching a maximum, a noticeable exponential decay is visible in Feature C. This intensity decrease is believed to be the formation of the first Ga chemisorbed adlayer which attenuates the reflection of the RHEED beam. This attenuation occurs because of the near-amorphous nature of the adsorbed Ga wetting layer as described above. It is worth noting that the exponential decay behavior of this feature ends prematurely and does not fully saturate. This implies that the low mobility of the first gallium monolayer directly on the underlying GaN results in an incomplete monolayer before the next

feature, the Ga-bilayer, begins to form. This incomplete monolayer formation explains the surface pits that form when traditional MBE is performed in the intermediate flux range [20]. Attenuation of the RHEED beam also suggests a discrepancy from the modeled contracted bilayer [32, 78] which predicted a contracted ordered crystalline Ga monolayer as was observed experimentally by Adelmann *et al*. [21]. This discrepancy is likely because of these models being developed at low temperature and not taking into account the dynamics of the flowing surface. Additionally, the growth conditions (very slow growth, and very hot substrate conditions) used in the case of Adelmann *et al*. make for a significant change from those used presently and may give enough time and fast diffusion for Ga adlayer ordering.

Feature D is a second, similar exponential decay believed to be the formation of the second Ga chemisorbed adlayer. The second monolayer dampens the RHEED streak intensity further. Unlike the first Ga monolayer, the full Ga bilayer has a higher mobility [33] and can fully cover the entire surface before another feature occurs. This leads to a nearly complete saturation of Feature D before the next feature begins. Feature E is the final decay attributed to Ga droplet formation, which continues on a downward trend until the Ga shutter is closed. It is worth noting that the behavior of this last feature is not exponential. Compared to the first two Ga accumulation processes (monolayer and bi-layer formation) which have clear limits in their final bounds (once full coverage is obtained), this last mechanism is unconstrained. Therefore, this non-exponential behavior is attributed to the complex three dimensional nature of the shadowing of the RHEED beam as Ga droplets are randomly formed and grow in size.

It has been shown that this droplet accumulation denoted as Feature E results in a delay after shutter closing that is dose dependent [20, 23, 24]. In the low-flux signal in Figure 2.3, Feature E and the subsequent delay do not exist, since the gallium flux was too low for droplets to accumulate before the shutter was closed. The delay in the RHEED signal on shutter close that is attributed to Ga droplets were examined for a variety of fluxes and are shown in Figure 2.6. Ga fluxes below 9×10^{-7} Torr BEP were found to have little to no delay, suggesting very little droplet buildup within the 10 second shutter open period. The delays were very similar for both substrate temperatures of 550 °C and 650 °C, suggesting that little Ga desorption or GaN decomposition occurs at these temperatures as expected. Delay time was found to be related linearly to Ga flux above 8×10^{-7} Torr BEP, further confirming the droplet coverage being Ga dose dependent.

After the Ga shutter was closed, the RHEED streak intensity slowly increases in Feature F in a droplet accumulating case as the Ga droplets are consumed by growth of GaN. It is important to point out that during this time the growth rate of GaN does not change, even though the growth occurs solely from the consumption of Ga droplets since the Ga source is closed. If an insufficient Ga dose was supplied during the 10 second shutter open half cycle such that droplets were not accumulated on the GaN surface, Feature F is not observed as shown in Figure 2.3 for the low-flux case (upper curve).

Feature G is attributed to the consumption of the full Ga bilayer as the amorphous surface scatters less of the RHEED beam, resulting in a rapid increase in signal intensity. This is supported by the RGA response of mass 27, which decreases rapidly at the closing of the Ga shutter as shown in Figure 2.5. Since Ga is no longer impinging upon the

surface, there is a reduction in competition between N and Ga for adsorption sites. This allows for higher nitrogen adsorption, resulting in a decrease in mass 27 partial pressure. The slope of Feature G was found to be independent of Ga flux provided that the supplied Ga dose fully saturates the bilayer feature, which supports the suggestion that Feature G results from the consumption of the bilayer, since the Ga shutter is closed during this feature. Feature G also exhibits a constant rate of rise regardless of previous Ga flux, which is attributed to the constant consumption of the bilayer as a result of a fixed nitrogen supply and a finite number of available bilayer sites. It is important to note that although the rate of rise of Feature G is constant for all experiments described above, the impinging N flux may be too high to differentiate the consumption of the second monolayer with the first monolayer of the bilayer. Therefore, the magnitude of the rate of rise of Feature G is similar to the slope of Features C and D (bilayer accumulation stages) shown in Figure 2.2 for the very high flux cases.

The local maximum between Feature G and H is attributed to the higher electron density of the remaining physisorbed Ga monolayer originating physically from the same mechanism described previously for Feature B. Finally, once this monolayer is consumed, the surface is again dominated by an accumulated electron-deficient nitrogen adlayer resulting in the lower intensity Feature H. The cycle then returns to Feature A. During this stage, when only a nitrogen adlayer is present, no growth occurs.

In order to confirm that the RHEED intensity spike seen in Feature A is actually a result of the Ga-N exchange, Ga and N were simultaneously exposed to a GaN surface that did not have a nitrogen adlayer. A nitrogen adlayer deficient GaN surface was prepared by accumulating one monolayer of Ga and immediately blocking both Ga and N

sources for 15 minutes. Simultaneous Ga and N exposure was performed by opening both shutters simultaneously. A sharp decrease in RHEED intensity was observed without a preceding spike as shown in Figure 2.7. Therefore, it is confirmed that Feature A results only when a sample is exposed to N flux before shutter opening and thus is directly related to the nitrogen adlayer.

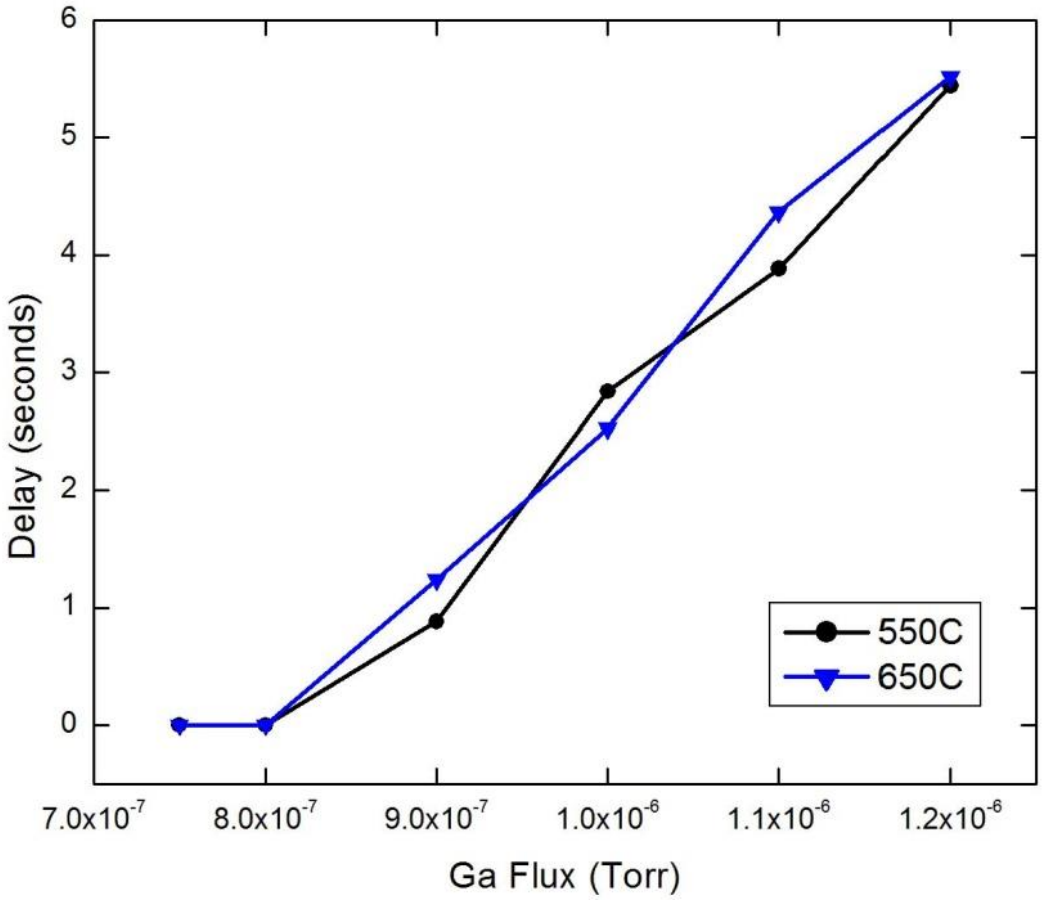

Figure 2.6: Recorded delay before RHEED intensity increase after Ga shutter close in the metal-rich regime versus flux for two temperatures. Note that the increase is linear after 8×10-7 Torr BEP.

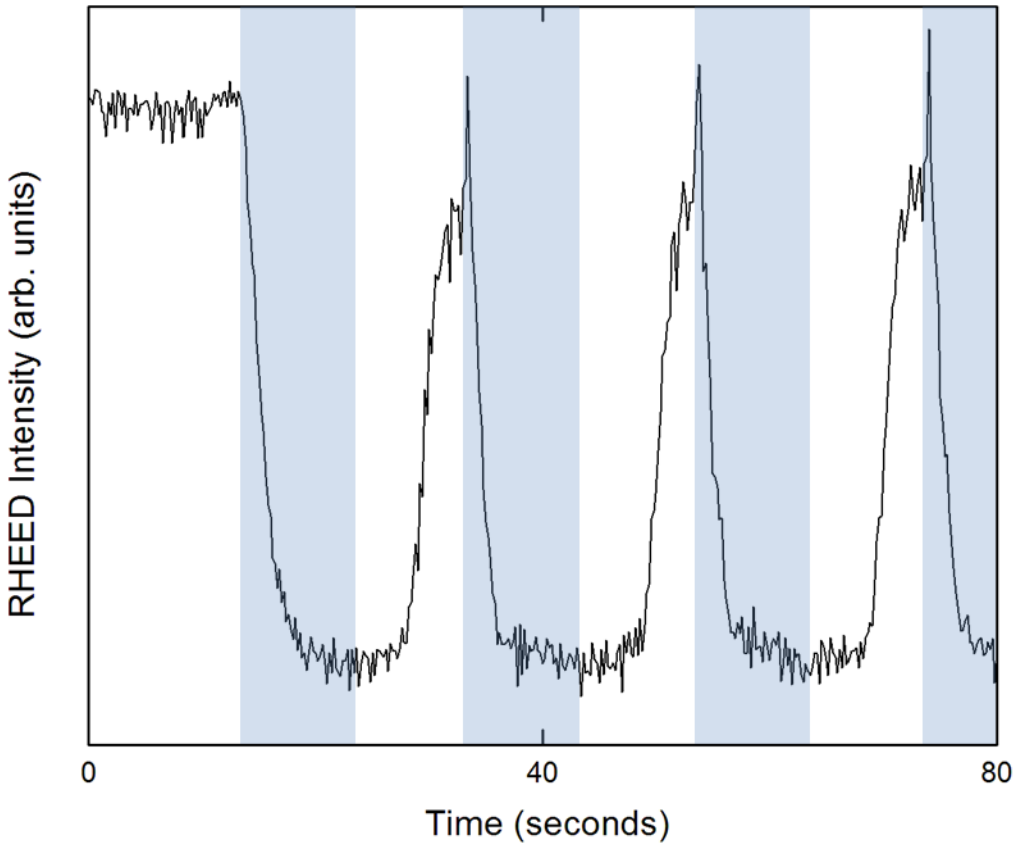

Figure 2.7: Transient RHEED signal recorded after closing both N and Ga shutters and desorbing off Ga from the sample. Both shutters were opened and no spike in intensity was seen on the first cycle, which confirms the relation of the spike to the nitrogen adlaye. Shaded regions indicate Ga shutter open portions of the modulation scheme, while the nitrogen shutter was permanently opened at the beginning of the first shaded region.

2.4 In Situ Growth Rate Determination

Given the complexity of the assumed model and the inability to directly observe the growing surface, the physical interpretation of some features of the indirect observations of RHEED and DMS described above may be disputed. Experiments were described above that confirmed the origin of all features except C and D. One may argue a different physical origin for these two features than those described herein. Therefore, we attempt to solidify the assumptions of the origin of Features C and D by estimating the growth rate *in situ* by applying the physics of the proposed model with comparison to the *ex situ* measured growth rate. While the model may be useful in growth rate determination, its primary purpose as presented here is to provide confidence in the assignment of features C and D to the physical mechanisms of monolayer and bilayer formation.

A novel *in situ* growth rate estimation technique is possible using the suggested surface kinetics model of MME. The relationship between flux, growth rate, bilayer buildup, and desorption can be summarized with the rate equation

$$R_{Flux} = R_{Growth} + R_{Bilayer} + R_{Desorption} \tag{2.1}$$

where the rates R_{Flux}, R_{Growth}, $R_{Bilayer}$, and $R_{Desorption}$ represent the rate of Ga arrival from the effusion cell, the rate of Ga consumption from growth, the rate of Ga bilayer buildup (which includes the first and second monolayers) and the rate of Ga desorption, respectively. At modulation schemes and substrate temperatures used for this study

($T_{sub} \leq 650$ °C), $R_{Desorption}$ $R_{Desorption}$ is negligible [5, 173]. When the Ga shutter is closed, $R_{Flux} = 0$, which leaves only

$$R_{Growth} = -R_{Bilayer}\,. \tag{2.2}$$

It has been suggested that when the Ga shutter is closed, the mobility of the Ga bilayer is high enough such that the droplets will fully sustain the bilayer until all droplets are consumed [5]. This finding gives rise to the significance in the transition between Features F and G, since that point in time is the beginning of the consumption of the bilayer. The entire bilayer, which corresponds to 2.3 monolayers of gallium [32], is consumed during Feature G. The rate at which GaN is constructed from the Ga bilayer can be translated directly to growth rate.

This growth rate, while determined from feature G alone, is the same nitrogen-limited rate found during Features B, C, D, E, F, and G. However, no growth occurs outside of these features, so the raw growth rate must be converted to an effective growth rate over the entire modulation cycle by accounting for the duty cycle. The duty cycle was found to be ~65% for low flux cases, and ~90% for high flux cases. Before factoring in the duty cycle, estimated growth rate for all experiments were approximately 1 μm/hr.

Figure 2.8 shows *ex situ* measured growth rates by profilometry and ranges of *in situ* estimated growth rates for three growths of bulk GaN with different metal-rich Ga fluxes. Note that this approach provides an *in situ* estimate of growth rate accurate to ±10%, making it both useful for practical applications and providing confidence in the model. The range in error was attributed to the low sampling rate of the photodiode and

human error involved with picking the correct locations of the transition points between various features in the transient signals.

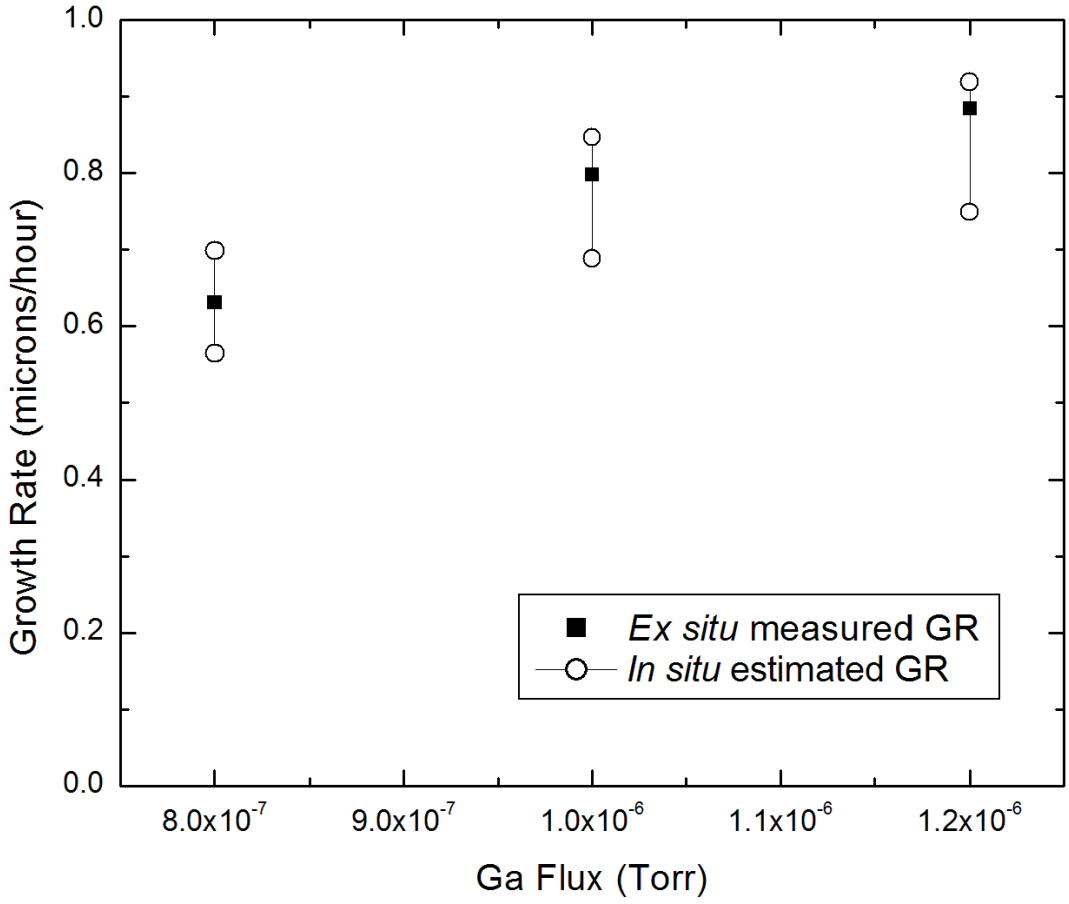

Figure 2.8: Measured *ex situ* growth rate and estimated *in situ* growth rate for three Ga fluxes.

2.5 Conclusions

In this study, a model for defining the surface kinetics and atomic behavior of metal adatoms on the surface of GaN is developed by systematically analyzing the transient RHEED intensity for a variety of different shuttered, metal-rich growth conditions. The suggested model not only provides the opportunity to achieve higher quality GaN films at lower temperatures, but also gives insight to the transient behavior of adatoms on the surface of the growing film. This model is employed in the development of a novel *in situ* growth rate estimation technique, which is found to have an accuracy of ±10%.

CHAPTER 3: GROWTH AND CHARACTERIZATION OF DEEPLY DEGENERATE P-TYPE GaN

3.1 Introduction

After the first report of p-type conductivity in GaN [88], the first InGaN-based blue LEDs were able to be commercialized [49, 50, 140]. However, there have since been relatively few advances in Mg-doped GaN [174]. The lack of high hole concentration p-type GaN has spurred a great deal of research into the difficult task of creating low-resistance Ohmic contacts to p-GaN layers with low hole concentrations [175, 176]. Some have even attributed the notorious efficiency droop in LEDs to low hole injection efficiency [102, 103, 177], which could be alleviated with better electrical quality p-type layers.

The objective of this study is to explore the doping of GaN with Mg by Metal-Modulated Epitaxy. A range of p-GaN samples are grown using one shutter modulation scheme but varying gallium fluxes. Room-temperature Hall effect measurements are used to characterize the hole concentration of grown layers versus Ga flux. Secondary ion mass spectroscopy (SIMS) analysis is used to determine Mg activation efficiency, and temperature-dependent Hall effect measurements are explored to further the understanding of extremely high hole concentrations in GaN.

3.2 Experimental Setup

All samples were grown in a Riber 32 MBE system using the Metal-Modulated Epitaxy technique on sapphire substrates. A standard effusion cell was used to supply aluminum, a Veeco SUMO cell was used to supply gallium, and a Veeco corrosive series valved cracker was used to supply magnesium. A Veeco Unibulb plasma source was used to supply active nitrogen species at 1.3 standard cubic centimeters per minute and was operated at 350 W. Sapphire substrates were backside coated in 1.5 μm of Ta to provide uniform radiative heating in vacuum. The substrates were then cleaned in a 4:1 mixture of H_2SO_4:H_2O_2 at 160 °C before being loaded into an introductory chamber and outgassed at 200 °C for 30 minutes. The substrates were then nitridated at a substrate temperature of 300 °C and a nitrogen flow rate of 1.3 standard cubic centimeters per minute [157-161]. A 140 nm AlN buffer layer was then deposited at 700 °C substrate temperature using an Al flux of 4.9×10^{-7} Torr BEP with a modulation cycle of 10 seconds of metal shutter open time followed by 10 seconds of metal shutter closed time [161, 162]. The magnesium cracker cell was operated with a bulk temperature of 300 °C, a tip temperature of 900 °C, and a valve position of 120 mils. Mg-doped GaN layers were grown for 40 minutes at 500 °C and 600 °C substrate temperatures with varying gallium fluxes in a random matrix to eliminate Mg memory effects in the chamber. The modulation scheme for all p-GaN samples was 5 seconds of metal and dopant shutter open time followed by 10 seconds of metal and dopant shutter closed time.

3.3 Growth of Extremely High Hole Concentration p-Type GaN

Several Mg-doped GaN samples were grown with Ga fluxes ranging from 3×10^{-7} Torr BEP to 1×10^{-6} Torr BEP at a substrate temperature of 500 °C. The hole concentrations and resistivities of these samples are shown by the solid circles and triangles, respectively, in Figure 3.1. For reference, the stoichiometric flux of Ga for this system is approximately 6×10^{-7} Torr BEP. Below the stoichiometric point, higher resistivities and lower hole concentrations are observed, similar to that found elsewhere in the literature for traditional MBE growth [174]. The low electrical performances of these films are attributed to columnar growth and faceting typically observed for nitrogen-rich growth [178, 179]. As gallium flux increases past the stoichiometric point and metal-rich growth begins to occur during the metal and dopant cell shutter open times, the resistivity decreases and the hole concentration increases. At a gallium flux of 7.5×10^{-7} Torr BEP, a peak hole concentration of 1.4×10^{19} cm^{-3} is observed with a resistivity of 1.15 Ω-cm and a mobility of 0.4 cm^2/Vs.

The metal-rich samples of this range were duplicated with a higher substrate temperature of 600 °C. The hole concentrations and resistivities of these hotter samples are shown by the open circles and triangles, respectively, in Figure 3.1. The samples at this higher substrate temperature had drastically higher hole concentrations. The highest hole concentration observed was 7.9×10^{19} cm^{-3} with a resistivity of 0.26 Ω-cm and a mobility of 0.3 cm^2/Vs at a gallium flux of 6.5×10^{-7} Torr BEP. This experiment showed that extremely high hole concentrations an order of magnitude higher than the previously accepted maximum [148, 149] could be obtained by Metal-Modulated Epitaxy.

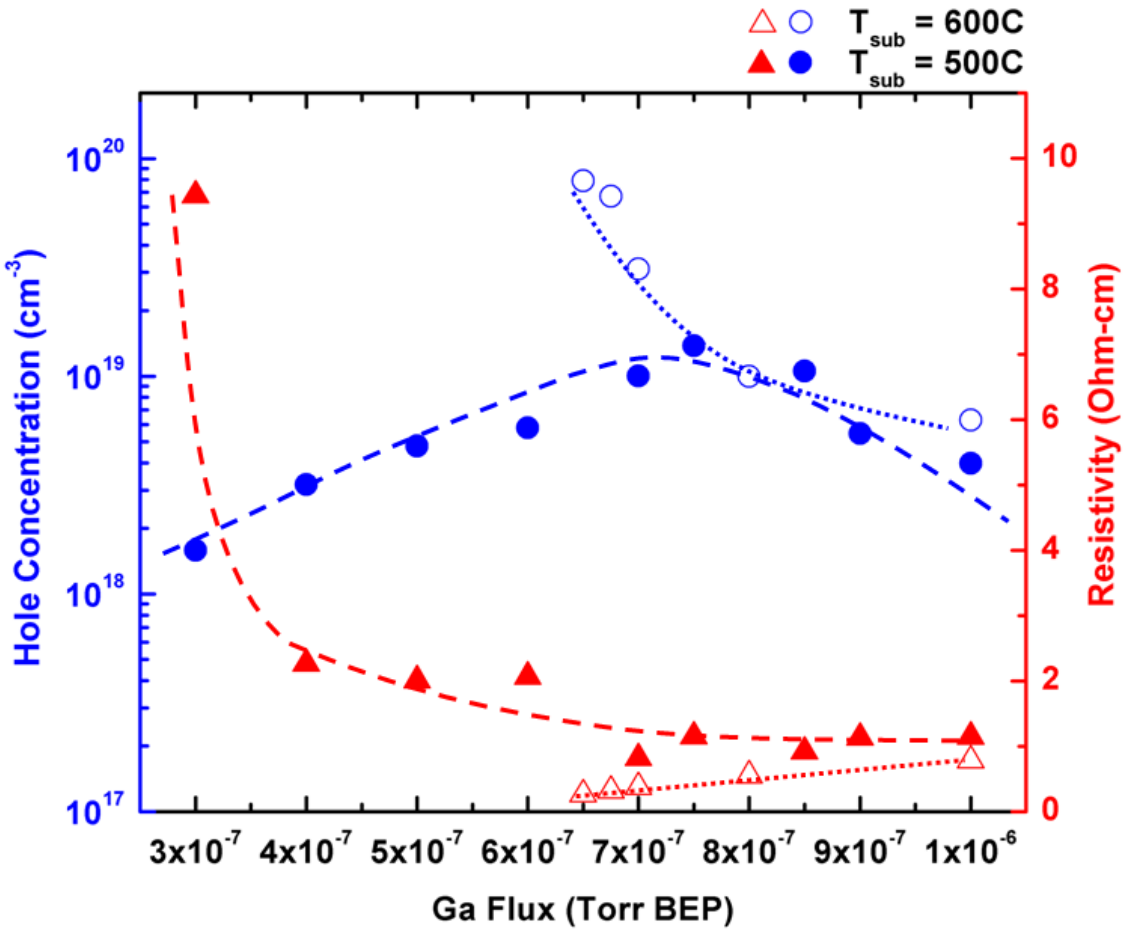

Figure 3.1: Dependence of hole concentration (circles) and resistivity (triangles) on gallium flux during MME of p-GaN. Solid shapes indicate growth at 500 °C, while hollow shapes indicate growth at 600 °C.

3.4 SIMS Analysis and Mg Activation Efficiency

One sample with a hole concentration of 6.7×10^{19} cm^{-3} was sent to Evans Analytical Group for SIMS analysis. The depth profiles of aluminum, gallium, and magnesium in this sample are shown in Figure 3.2. It should be noted that the levels of residual H, C, and O were lower than the measured hole concentration, ruling out co-doping effects. The Mg concentration of this sample was averaged over the thickness of the p-type layer, yielding an average dopant concentration of 1.28×10^{20} cm^{-3}.

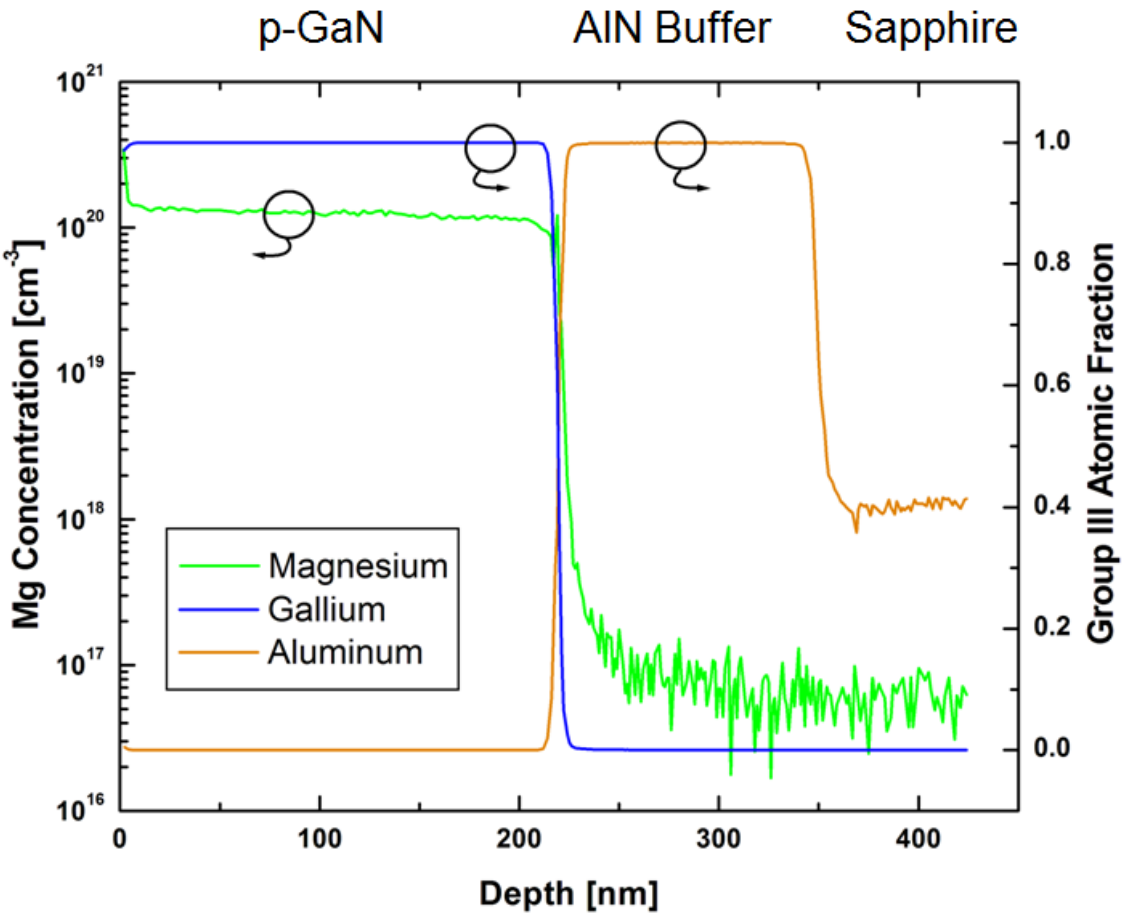

Figure 3.2: SIMS profile of a sample with a hole concentration of 6.7×10^{19} cm^{-3} hole concentration. Average detected level of Mg in the p-GaN region was 1.28×10^{20} cm^{-3}.

The doping efficiency can be extracted by dividing the hole concentration by the measured Mg concentration. It was found that the doping efficiency for this particular sample was 52.3%, which is substantially higher than that reported in literature for p-GaN layers grown by MBE [147, 174, 180], MOCVD [181-183], and even MME [44, 153].

3.4 Conclusions

This study revealed that extremely high hole concentrations in GaN were possible. A maximum hole concentration of 7.9×10^{19} cm^{-3} was detected, which is over an order of magnitude higher than those reported by traditional growth techniques. SIMS analysis detected a Mg doping efficiency of over 50%, indicating that this growth technique is capable of not only introducing an enormous amount of Mg into p-GaN layers, but also placing these dopants on the correct Ga-substitutional site. The breakthroughs in electrical performance of these MME-grown p-GaN layers facilitate the development of devices relying on extremely low contact resistances and tunnel junctions.

CHAPTER 4: OBSERVATION AND CONTROL OF SURFACE SEGREGATION IN $In_xGa_{1-x}N$ BY TRANSIENT RHEED ANALYSIS

4.1 Introduction

For over two decades [48] the group-III nitride materials system has been the subject of rigorous investigation for its electronic [66] and optoelectronic [124] properties. Indium-bearing nitrides possess the unique capability of a bandgap that can be can be engineered from 0.7 eV (InN) to 3.4 eV (GaN), creating a wide array of applications in light-emitting [51, 140] and photovoltaic devices [52, 151]. High breakdown fields [46] common among all group-III nitrides provide a foundation for high-power electronics [47]. Although this materials system boasts a large set of potential applications, there still exist many challenges with the growth of indium-bearing nitrides.

InGaN alloys are especially prone to phase separation through several processes: spinodal decomposition [116], thermal decomposition [19, 123], and indium surface segregation [131, 133]. These processes create inhomogeneities in the crystal, which can be detected via standard materials characterization techniques, including x-ray diffraction [184], and transmission electron microscopy [73]. Although these inhomogeneities have been shown to assist in radiative emission in LEDs due to enhanced carrier localization, devices like solar cells[52, 53] and laser diodes[50] require more uniformity.

These detrimental processes have been shown to be related to growth conditions, and thus can be suppressed. For instance, reductions in growth temperature have been shown to reduce thermal [126] and spinodal decomposition [116], while nitrogen-rich growth conditions can be used to inhibit indium surface segregation [19, 135]. However, lower substrate temperatures and nitrogen-rich growth are both associated with reductions in material quality [12, 137]. Therefore, a new approach to nitride growth is appealing.

The constraints of InGaN growth suggest Metal-Modulated Epitaxy (MME) as a potential growth candidate, which has been successfully used for AlN [23, 24], and GaN [28, 29, 43-45, 153]. MME is a low-temperature growth technique applied to group-III nitrides in which metal and dopant cell shutters are periodically opened and closed while the active nitrogen flux remains constant. This technique generally uses extremely metal-rich fluxes that would rapidly accumulate droplets in traditional molecular beam epitaxy, exploiting the enhanced adatom diffusion supplied by an excess metal layer [33]. However, periodic closing of the metal and dopant cells allows this excess metal to be consumed into the film, providing abrupt interfaces. The low temperatures used during MME avoid desorption of adatoms from the substrate, thereby reducing sensitivity to temperature variations and increasing growth uniformity. MME has been shown to significantly advance p-type doping in GaN [28, 43-45, 153], resulting in hole concentrations in the 10^{19} cm^{-3} range. Furthermore, MME can be used in concert with transient reflection high energy electron diffraction (RHEED) intensities, providing a unique *in situ* characterization method with observation and control of fractions of metal monolayers [29].

The objective of this study is to apply Metal-Modulated Epitaxy to the growth of unintentionally doped InGaN and elucidate the mechanisms of phase separation. Surface kinetics and structural properties of InGaN are investigated. Indium surface segregation is identified and subsequently alleviated *in situ* via transient RHEED analysis.

4.2 Experimental Setup

Growths for this study were conducted in a Riber 32 MBE system with standard effusion cells for gallium and indium. Active nitrogen was supplied by a Veeco Unibulb plasma source operated at 350 W and a flow rate of 1.3 sccm. To insure identical starting defect structure for all films, substrates used were Lumilog MOCVD-grown GaN templates and were backside sputtered with 1 μm of Ta to provide uniform and efficient heating. The substrates were cleaned in H_2SO_4:H_2O_2 (4:1) at 160 °C before being loaded into an introductory chamber and outgassed for 30 minutes at 200 °C. A ~100 nm GaN buffer was grown via MME on the templates at 600 °C using extremely metal-rich, shutter-modulated conditions to create a clean, smooth surface for InGaN growth [29]. All InGaN alloys were grown from 400 °C to 450 °C and had the same metal-rich total group-III flux of 0.24×10^{-7} Torr BEP normalized by Z-number to account for ion gauge sensitivity differences between In and Ga. The indium to gallium ratio was varied to grow the targeted indium content film, and both Group-III shutters were modulated simultaneously with a constant nitrogen flux.

4.3 Growth of $In_xGa_{1-x}N$ layers by Metal-Modulated Epitaxy

Two metal-rich InGaN samples best representative of the trend described herein were grown with different shutter modulation schemes for 10 minutes each. Sample A was grown with a modulation scheme of 10 seconds metal shutter open time and 10 seconds metal shutter closed time. Sample B was grown with a modulation scheme of 4 seconds metal shutter open time and 10 seconds metal shutter closed time. The metal fluxes for both samples targeted an indium composition based on normalized fluxes of 22%. The transient RHEED intensities and RHEED patterns of these two samples are shown in Figure 4.1. The transient RHEED intensity and RHEED pattern recorded during the growth of Sample A is shown in Figure 4.1(a) and (c), respectively. The transient RHEED intensity and RHEED pattern recorded during the growth of Sample B is shown in Figure 4.1(b) and (d), respectively. The shaded regions indicate where the metal shutters were open. The shaded regions of the transient RHEED intensities shown on the left side of Figure 4.1 indicate the time when the metal shutters were open. In the transient RHEED signatures of both samples, a peak intensity occurs shortly after opening the metal shutters. The reader's attention is then directed to the behavior of the intensity upon closing of the metal shutters.

In Sample A, the metal shutters are closed several seconds after this peak takes place, and the RHEED intensity then immediately drops to a very low level as shown in Figure 4.1(a). A dark, diffuse RHEED pattern is visible during this process and is shown in Figure 4.1(c), with a contrast enhanced version shown as an inset. This diffuse RHEED pattern indicates that residual indium is present on the surface, decreasing the

RHEED intensity by both shadowing of the beam by droplets and scattering of the beam by the higher electron content of the indium atoms [34, 35].

In Sample B, the metal shutters are closed during the decline in intensity almost immediately after the peak, as shown in Figure 4.1(b). After the closing of these shutters, the intensity continues decreasing to a local minimum and increases again to a flat, steady state level, indicating growth continues after the metal shutters are closed until all adsorbed metal is consumed. The RHEED pattern visible during this growth condition is shown in Figure 4.1(d). As shown in Figure 4.1(d), a bright and streaky RHEED pattern visible during growth indicates a smooth, dry surface with no residual indium adlayers or droplets.

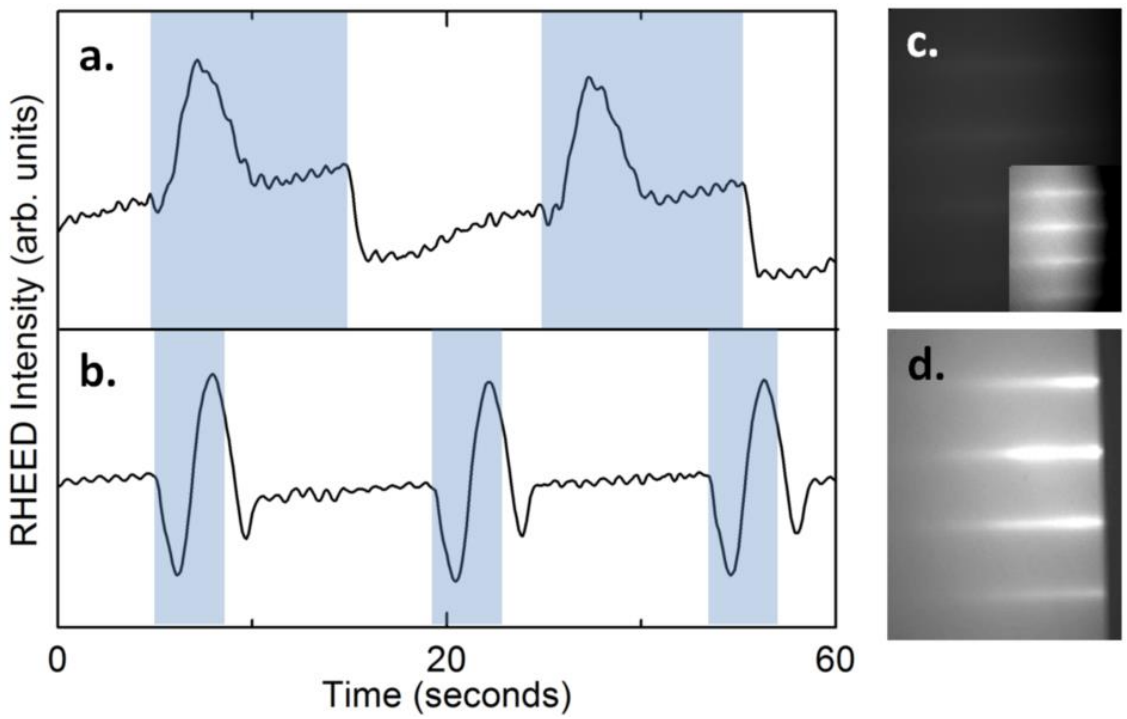

Figure 4.1: Transient RHEED intensities and RHEED patterns of two InGaN samples: 10 seconds (top) and 4 seconds (bottom) metal shutter open time per cycle. Because of the low brightness of the RHEED pattern for Sample A, a contrast enhanced version is included as an inset.

The x-ray diffraction scans, RHEED patterns after cooldown under nitrogen plasma, and atomic force microscope (AFM) morphologies of Samples A and B are shown in the top and bottom rows of Figure 4.2, respectively. The x-ray diffraction scan of Sample A shown in Figure 4.2 (a) reveals a broad InGaN peak corresponding to multiple phases of material with an average composition of 18% indium, lower than the normalized flux targeted composition of 22%. A peak at 31.3° corresponding to InN is also visible. Furthermore, after cooling down under a nitrogen plasma, a spotty RHEED pattern appears at a different spacing than the InGaN streaks underneath and is shown in Figure 4.2 (c). A very rough surface of 3.81 nm RMS is visible in the AFM image shown in Figure 3(e) and resembles large, nitrided drops of indium.

The lower metal shutter open time growth, Sample B, exhibits an InGaN peak corresponding to 22% indium content with prominent thickness fringes as shown in Figure 4.2(b). The InN peak at 31.3° is reduced in intensity compared to that of Sample A. The AFM morphology of Sample B shown in Figure 4.2(f) is much smoother at 1.06 nm RMS, however still shows what looks like small crystalline structures on a smooth underlying surface. Although the RHEED pattern during growth shown in Figure 4.1(d) was very bright and streaky, upon cooldown under a nitrogen plasma a spotty pattern still appears as shown in Figure 4.2(d).

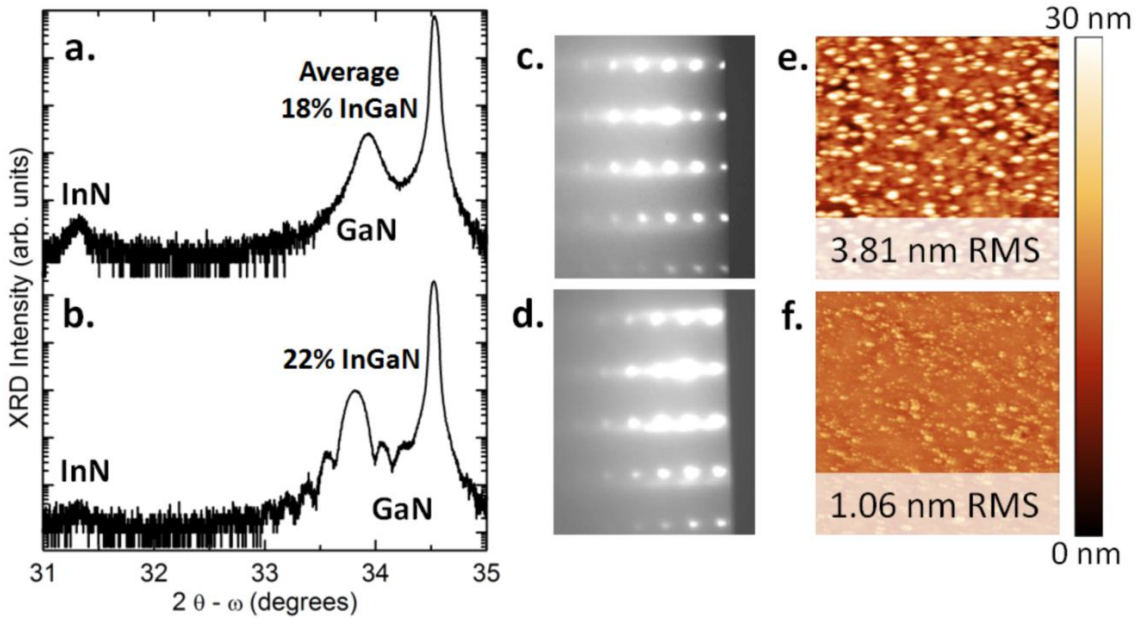

Figure 4.2: X-ray diffraction scans, RHEED patterns recorded after growth, and atomic force microscope morphologies of Sample A and Sample B. Results from Sample A are on the top row, while results from Sample B are on the bottom row.

4.4 Identification of Indium Surface Segregation

It is clear from the XRD, RHEED, and AFM data that Sample A exhibits strong evidence of surface segregation during growth, displayed by the dark RHEED pattern from residual indium adlayers and droplets during growth, nitrided indium droplets upon cooldown evident from the XRD peaks and AFM morphology, and a broad InGaN XRD peak shifted towards GaN. In contrast, Sample B exhibits a bright RHEED pattern during growth indicative of no residual indium layers or droplets present during growth with a single-phase XRD spectra at the targeted composition. Thus, the sharp decrease in RHEED intensity upon closing the metal shutters during the growth of Sample A is then attributed to the consumption of gallium in the segregated metal adlayer, leaving indium behind during the shutter closed period and generating a darker RHEED pattern.

4.5 Prevention of Thermal Decomposition

It should be noted that although no indium surface segregation occurs in Sample B, there is still evidence of InN in the x-ray diffraction scan, after-growth RHEED pattern, and AFM. An identical sample was grown with a 10 nm GaN cap to prevent thermal decomposition during the cooldown step. The XRD, RHEED, and AFM data from this GaN-capped sample are shown in Figure 4.3.

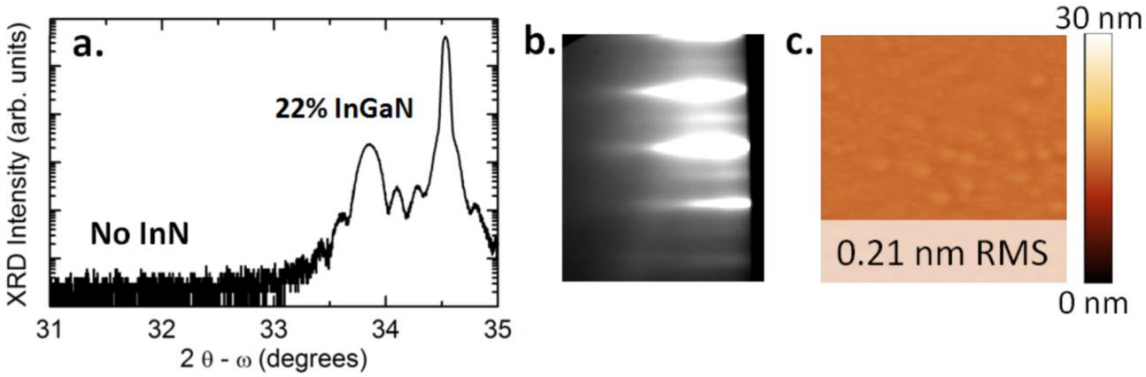

Figure 4.3: X-ray diffraction scan, RHEED pattern recorded after growth, and atomic force microscope morphology a sample identical to Sample B, but capped in 10 nm of GaN.

As shown in Figure 4.3(a), the sample with a smaller shutter open time of 4 seconds open and capped in 10 nm of GaN exhibits no evidence of InN in the x-ray diffraction scan. Furthermore, a 2 × 2 reconstruction pattern shown in Figure 4.3(b) is visible after cooldown under a nitrogen plasma, indicating a very smooth surface with no spots from either In or InN. The AFM morphology of this sample is shown in Figure 4.3(c), exhibiting a surface roughness of 0.21 nm RMS. These results indicate that the small InN peak in the XRD and the microstructures in the AFM observed in Sample B

result from thermal decomposition of the InGaN surface at the end of the growth [34, 35]. This residual indium on the surface is subsequently nitridated under a nitrogen plasma into InN as the temperature drops low enough for InN to become stable.

Indium surface segregation has been reported to be related to III-V ratio and it is typically suppressed by employing nitrogen-rich growth conditions [123, 126]. This study shows that indium surface segregation is not necessarily dependent on growth regime, but instead is more accurately associated with the quantity of the adsorbed metal. Both Sample A and Sample B were grown in metal-rich conditions, accumulating a metal adlayer during each modulation cycle. However, the excess metal dose was limited in Sample B, and no evidence of indium surface segregation was observed. Despite the limited quantity of the metal adlayer, Sample B still exhibited a (0002) rocking curve full width at half maximum (FWHM) of 362 arcseconds at the InGaN peak. This rocking curve FWHM is similar to the GaN template used to substrate these layers. This outstanding material quality suggests that the enhanced adatom mobility associated with an adsorbed metal layer is exploited [19, 124, 135], yet no indium surface segregation effects are observed due to the limited excess metal dose.

4.6 Conclusions

Surface kinetics of InGaN have been explored through the use of MME combined with analysis of transient RHEED intensities. It was found that indium surface segregation is not solely associated with growth regime, but instead is more dependent on excess metal dose. MME allows the management of the metal dose through shuttered growth, exploiting the benefits of metal-rich growth while eliminating droplet formation or indium segregation. A method for observing and controlling indium surface segregation *in situ* via RHEED during MME growth of InGaN is demonstrated. This chapter reveals that metal adlayers can be controlled to produce enhanced material quality in InGaN without promoting indium surface segregation.

CHAPTER 5: CONTROL OF SURFACE ADATOM KINETICS FOR THE GROWTH OF HIGH INDIUM CONTENT InGaN THROUGHOUT THE MISCIBILITY GAP

5.1 Introduction

InGaN alloys are promising materials for device applications such as light emitting diodes and photovoltaics [52, 66, 150, 151]. The direct bandgap of InGaN can be tuned to allow emission or absorption from the entire visible spectrum by adjusting the indium content. However, high indium fraction InGaN alloys are notoriously difficult to obtain as a result of spinodal decomposition [116, 185], indium surface segregation [124, 133, 137, 139], and thermal decomposition [19, 126]. Furthermore, higher indium content InGaN alloys have a larger lattice mismatch to GaN, which results in increased defect densities caused by strain relaxation [186, 187].

The low temperatures required for high indium content InGaN makes metal-modulated epitaxy (MME) a promising growth technique for these complex materials. MME is a growth technique in which extremely high Group-III metal fluxes are shuttered at a fixed modulation scheme while impingent nitrogen flux remains constant. Several variants of shuttered growth have been proposed and are differentiated from MME elsewhere [29]. This growth method has been employed for both GaN and AlN [23, 24, 28, 29, 44, 45, 153] and has been shown to result in improved material quality and grain sizes as a result of the enhanced surface adlayer diffusion provided by the accumulated

metal layers, even at low temperatures (400 °C - 600 °C). The periodic closing of the metal effusion cells is essential to the process, which allows for complete consumption of excess metal on the surface, preventing droplets from persisting throughout the growth. Previously high hole concentrations have been reported [28, 44, 45, 153] and more recently, hole concentrations in GaN in excess of $7x10^{19}$ cm^{-3} have been demonstrated by the authors using this technique. When combined with an *in situ* analysis of transient intensities of reflection high-energy electron diffraction (RHEED) streaks, this technique has been shown to provide crucial insight into the surface kinetics of III-nitride growth [23, 24, 29].

The objective of this study is to perform a comprehensive study of the growth of InGaN by MME in order to further understand the surface kinetics and atomic behavior of metal rich growth in InGaN. Specifically, the onset of indium surface segregation is studied to elucidate its causes and discover a way to prevent it. A quantified model correlating excess adlayer dose to surface segregation is developed. MME is then employed to grow InGaN films with varying compositions to determine the feasibility of this technique for high-quality, high indium content InGaN.

5.2 Experimental Setup

All layers were grown in a Riber 32 MBE system using standard effusion cells for indium and aluminum, and a Veeco SUMO cell was used to supply gallium. A Veeco Unibulb plasma source was employed for nitrogen, and had a flow rate of 1.3 sccm at 350W. Growth rates were approximately 800 nm/h for all InGaN growth reported herein.

To provide a uniform starting point for all studies, Lumilog metal organic chemical vapor deposition grown GaN templates were used as substrates and were back-side sputtered with 1 μm of Ta to provide uniform heating [153]. Substrates were cleaned in H_2SO_4:H_2O_2 (4:1) before being loaded into the introductory chamber and outgassed at 200 °C for 30 minutes [29]. All InGaN alloys were grown between 400 °C and 450 °C with metal-rich fluxes [30]. Metal fluxes used were normalized based on atomic number to account for ion gauge sensitivity differences between In and Ga and were between 0.24 and 0.3 × 10^{-7} Torr normalized BEP.

InGaN was grown via MME using a shutter modulation scheme similar to that described previously [30], which is illustrated in Figure 5.1. Both indium and gallium are opened and closed simultaneously, while nitrogen remains constant. This shutter scheme was used to study the reflection high energy electron diffraction (RHEED) response of In/Ga adlayers, and to achieve metal-rich growth of InGaN while preventing droplet buildup.

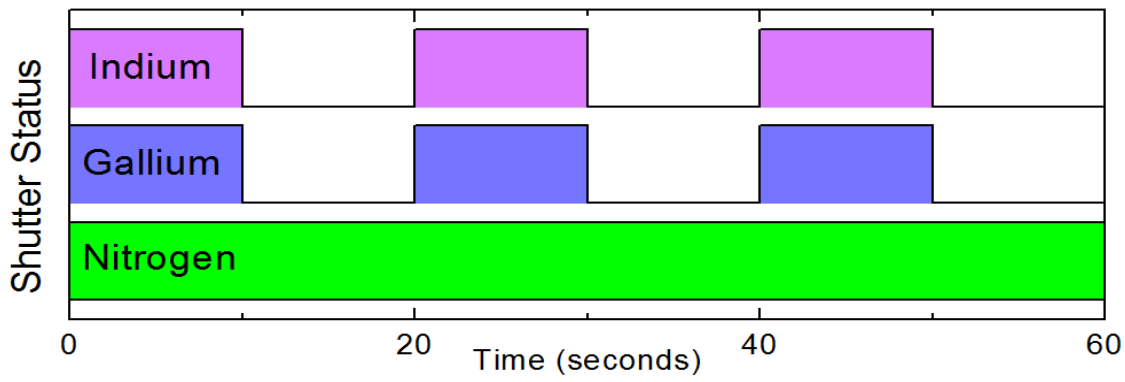

Figure 5.1: Simplified illustration of the modulation scheme used for the MME growth of InGaN.

Samples were grown with differing metal shutter open times and indium to gallium ratios to characterize adatom kinetics of the growing InGaN surface. A range of indium compositions throughout the miscibility gap of InN-GaN were grown using conditions found during the experiment. Independent confirmation of the success of these findings is also provided.

5.3 Qualification of Shuttered, Metal-rich InGaN Growth Kinetics

Previous results have shown the success of using metal-modulated epitaxy to suppress indium surface segregation in InGaN while still growing metal rich [30]. Although features of transient RHEED intensities during the growth of InGaN were related to indium surface segregation, association of each feature of the InGaN RHEED transient to a surface mechanism and the *in situ* quantification of indium surface segregation has until now not been reported. In Figure 5.2, representative RHEED transients observed during the growth of 20% InGaN for several metal shutter open times from 1.5 seconds to 3.25 seconds are shown with shaded regions indicating metal shutters open. These transient RHEED intensities were determined from one growth for consistency, with GaN interlayers grown between each InGaN layer to consume residual indium from the intentional surface segregated conditions and to provide a smooth template to facilitate comparable initial growth conditions. It is worth noting that the shutter open times shown in Figure 5.2 are smaller than those previously reported for similar RHEED transients, which are due to an increase in total metal flux in this present

experiment. Furthermore, an enhancement of signal-to-noise ratio in RHEED intensity collection has allowed for more detail, and thus more accurate data analysis.

Several features across all shutter open times are immediately apparent. First, a decrease of intensity on shutter open occurs, and is immediately followed by an increase in intensity. A flat, steady state intensity is also reached within a few seconds of metal shutter close which is visible across all shutter open times. Shutter-open-time-dependent features include a decreasing level of the steady-state intensity relative to a peak intensity observed during the shutter open period and an increasing width of a peak during the shutter open cycle for higher shutter open times. All of these features will be discussed in detail below. An expanded view of the 1.5 seconds, 2 seconds, and 2.75 seconds shutter open time RHEED transients are shown in Figure 5.3 in order to identify and explain specific features.

Shown in Figure 5.3 are expanded views of 3 transient RHEED signatures shown previously in Figure 5.2. Specific features to be discussed are colored in blue and green, where the blue region indicates metal shutter open time. The region shaded in green is a signature observed after the metal shutters are closed. Following the green region is a section of relatively flat intensity described herein as a steady state period. It is clearly seen from both Figure 5.2 and Figure 5.3 that for a given metal shutter open time in a modulation scheme, the transient RHEED intensity always begins and returns to the same intensity, regardless of truncation. If these RHEED oscillations were the result of constructive/deconstructive interference from the growing InGaN film [16, 188-191], terminating the growth by closing the cell shutters at different portions of the growth cycle would result in the next open shutter cycle picking up where the previous

oscillation left off. This correlation of the signature to the solid state growth of the InGaN film is not observed, an instead the intensity returns to a steady-state level upon closing the metal shutters. It can then be stipulated that the transient cannot be associated with a RHEED oscillation of the growing nitride film, and therefore must be dominated by the accumulation and subsequent consumption of the metal adlayer. An oscillatory relationship between adlayer accumulation and elimination has been observed previously in the literature [6, 21, 192], and is further supported by the analysis of the signature as described below.

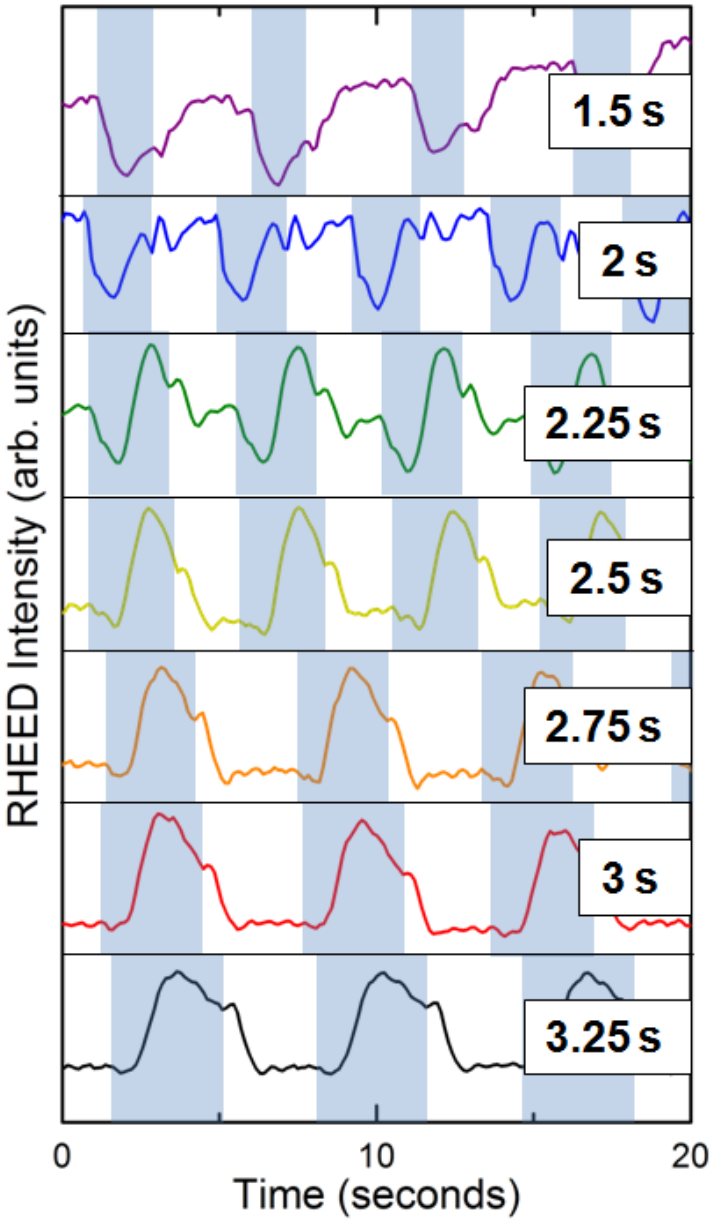

Figure 5.2: Transient RHEED intensity versus time for several metal-shutter open times. Shaded regions indicate metal shutters open.

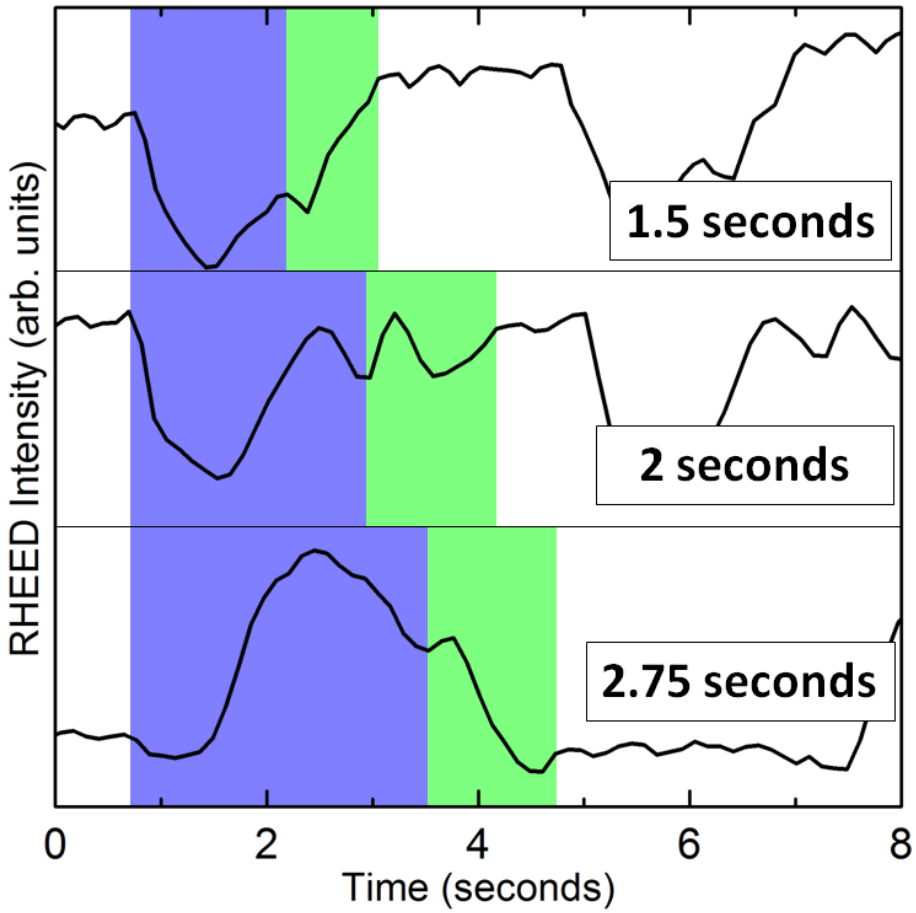

Figure 5.3: Expanded view of three transient RHEED intensities shown in Figure 5.2. Blue and red regions indicate where the metal shutters were open. Green regions indicate a period of oscillation before returning to steady state.

The reader's attention is directed to the 2 seconds metal shutter open time section of Figure 5.3. The white region on the left side of the figure is a flat RHEED intensity reached after a previous cycle and before metal shutters are opened that will be referred to as a steady state. Upon opening the metal shutters, an oscillatory function composed of the blue region occurs. This behavior is attributed to a RHEED oscillation associated solely on the adsorption of one metal monolayer (ML), where the minimum intensity is

deconstructive interference caused by an incomplete layer, and the following maximum intensity is constructive interference caused by a complete layer. The remaining decrease in intensity is a continuation of this sinusoidal oscillation as the second monolayer of metal is adsorbed, but is truncated by the closing of the metal shutters, halting the supply of metal to the surface. After the metal shutters are closed, the green region occurs, which is another sinusoid that resembles the time-opposite of the blue region. This signature is attributed to the consumption of the adsorbed metal layer into the film. After the green region occurs, where adsorbed metal is consumed into the film, a steady state is again reached. An illustration of this process is shown in the non-segregated column of Figure 5.4, and a characteristic RHEED pattern of a sample grown under these conditions is shown in Figure 5.5(a), which confirms a flat, dry surface by the bright streaks.

Next, the expanded view of the 1.5 seconds shutter open time RHEED transient of Figure 5.2 is examined, and is shown at the top of Figure 5.3. This case is also non-surface segregated, and is similar to the 2 seconds metal shutter open time case considered above. With the use of a smaller shutter open time, a comparable RHEED oscillation is observed during the blue region after opening of the metal shutters. This oscillation similarly corresponds to the adsorption of the first monolayer of excess metal. However, the metal shutters are closed before a full oscillation takes place, which indicates truncation of excess metal accumulation before a full monolayer forms. Upon closing of the metal shutters, this excess metal is consumed into the film during the green region, and a signal that resembles the time opposite of the blue region occurs. Unfortunately, although this film exhibits no form of indium surface segregation, the lack of accumulation of a full adlayer limits the beneficial effects of the metal adlayer [12, 32]

on surface smoothness. This roughness is demonstrated by both the gradual increase in RHEED intensity over time in Figure 5.2 and Figure 5.3, and the spotty RHEED pattern in Figure 5.5(b). An illustration of this process is shown in the non-segregated column of Figure 5.4 excluding the bottom two steps in the blue region.

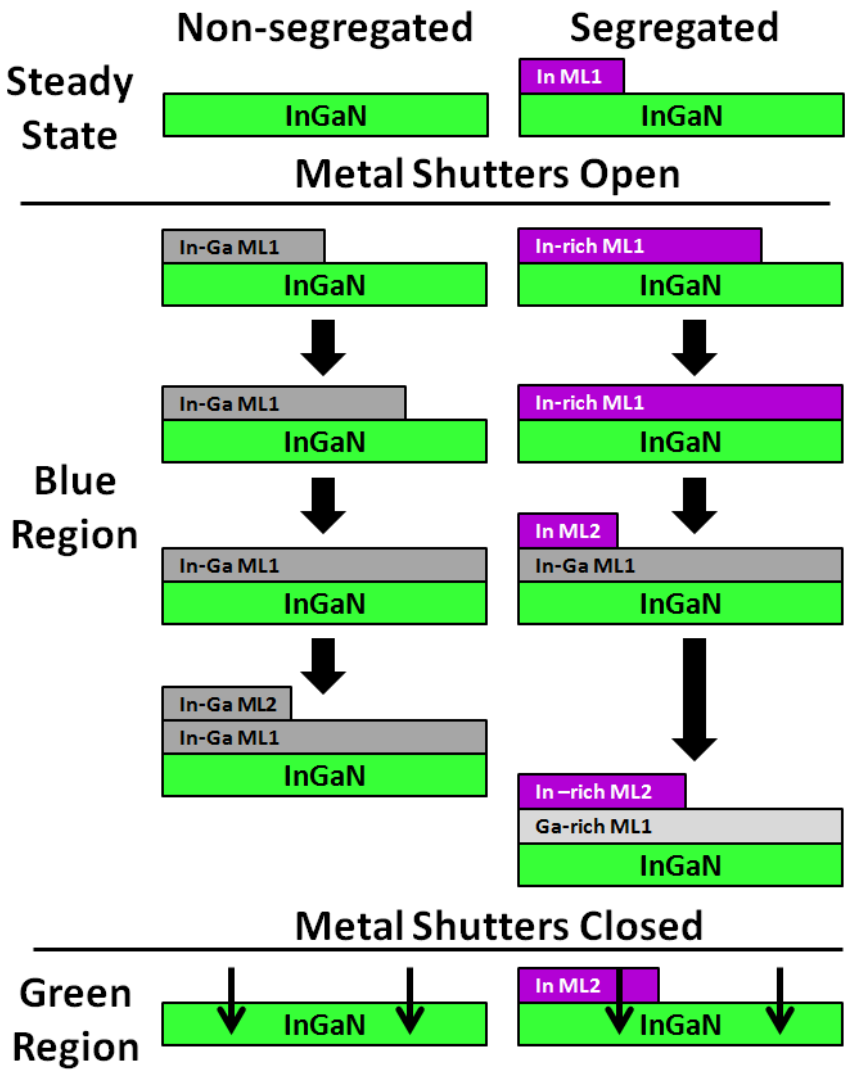

Figure 5.4: Illustration of the mechanism of indium surface segregation during MME of InGaN.

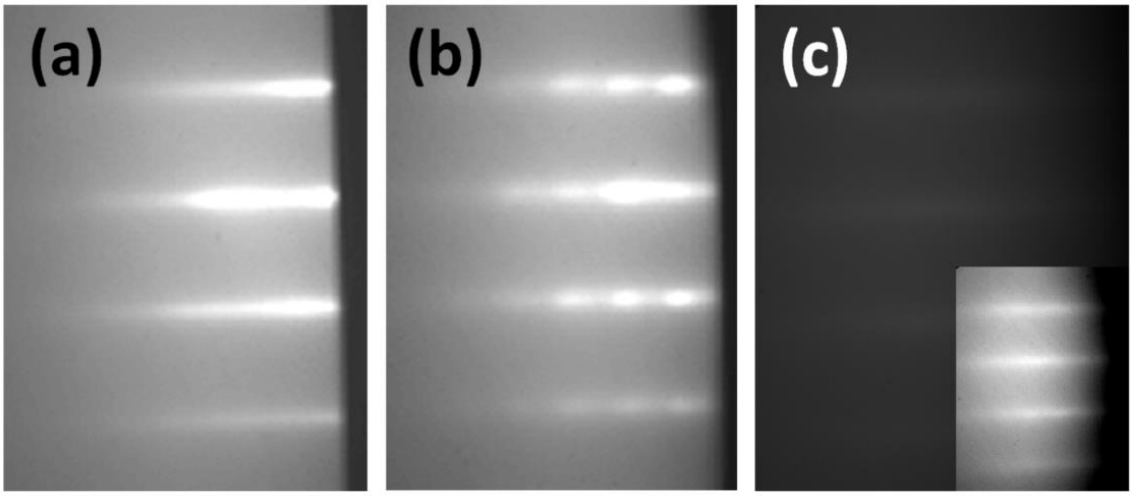

Figure 5.5: Characteristic RHEED patterns of InGaN grown with (a) a standard shutter open time, (b) a low shutter open time, and (c) a high shutter open time. Since the RHEED pattern of (c) is so that dim it may appear black to the reader, a brighter, contrast-enhanced version is included as an inset.

Finally, the zoomed-in view of the RHEED transient with the 2.75 second shutter open time is considered, shown in Figure 5.3. This case is similar to one established in a previous work to be indicative of indium surface segregated InGaN growth [30]. Before analyzing transient RHEED intensities of this extreme case, it is important to determine the qualitative condition of the steady state period between modulation cycles, shown by the white region on the left. In this case, so much excess metal is supplied to the adlayer in the previous modulation cycle that indium surface segregation has occurred, resulting in indium atoms riding on top of the rest of the adsorbed metal. Upon consumption of the adlayer, residual indium metal remains on the surface, as indium nitride cannot form in this system at the substrate temperatures used for these growths [131]. The presence of indium is supported by the diffuse RHEED pattern [19] visible during the shutter closed portion of the modulation scheme, shown in Figure 5.5(c). With an understanding that

some amount of metallic indium is present on the surface during the steady state period, an analysis of transient RHEED intensities during a growth condition with surface segregation can be performed.

Upon opening the metal shutters in the blue region of the 2.75 second shutter open time transient in Figure 5.3, the RHEED intensity quickly decreases to a minimum before steadily increasing again to a maximum. The time elapsed until reaching the minimum intensity is reduced in this case compared to the transients with smaller shutter open times in Figure 5.2. Furthermore, the intensity during the steady state period is also decreased. These features are concurrent with the conclusion that indium is already present on the surface. The deconstructive interference produced by this incomplete layer results in a phase shift in the sinusoid associated with the RHEED oscillation. The behavior of the RHEED intensity after opening the metal shutters is then attributed to an oscillatory function associated with the continued accumulation of one monolayer of excess metal. Since only indium may be present as all residual gallium would have been consumed [19], it can be expected that this newly assembled adlayer is indium-rich, potentially forming In-rich InGaN.

The RHEED intensity then continues to increase as the first ML begins to finish. However, the analysis of the RHEED transients becomes more complex than constructive/deconstructive interference considerations when gallium begins to replace indium for surface sites. As the first ML finishes and further impingent metal cannot spread laterally, a second monolayer begins to form. In this case, incoming gallium atoms will preferentially displace indium atoms in the indium-rich first monolayer [19, 135, 136]. This process provides an increase in intensity after the first monolayer forms,

as gallium has been shown to scatter the RHEED beam less than indium [34, 35]. The second monolayer is also able to hold more metal than the first monolayer [6, 21, 192], which causes a decrease in frequency of the sinusoidal RHEED oscillation. These two effects produce a tall, broad peak in the RHEED intensity just after one ML of excess metal accumulation.

The substitution of gallium for indium on surface sites will also affect the composition of the growing InGaN film, producing indium-lean material. Combined with the growth of indium-rich InGaN from a mostly indium adlayer at the beginning of the modulation scheme, this surface-segregated growth is expected to produce a multi-phase material. Evidence of composition fluctuations from similar growth conditions has been shown previously [30] by wide x-ray diffraction scan peaks in surface segregated samples.

After the metal shutters are closed, the green region occurs, resembling a faster, time-opposite of the blue region. Similarly to the green regions of the smaller shutter open times, this period of the transient RHEED intensity indicates consumption of adlayer material into the film. However, in this case, indium has been displaced by gallium to the second monolayer, and the adlayer as a whole is no longer homogenous. As the adlayer is consumed, the indium-lean first monolayer incorporates first [33], leaving mostly indium on the surface. At the temperatures used for this growth InN cannot form in this system. This process leaves residual indium on the surface during the steady state period, which contributes to the diffuse RHEED pattern shown in Figure 5.5 (c) and a decreased RHEED intensity shown in Figure 5.2 and Figure 5.3. An illustration of this process is shown in Figure 5.4 under the surface segregated column.

It is thus shown that indium surface segregation is linked to adlayer accumulation on the growth surface as opposed to metal-rich growth in general. By limiting the quantity of this adlayer, surface segregation can be inhibited and metal-rich growth of InGaN can be conducted. However, the thickness of this adlayer can be limited too much, hindering the smoothing effect of a wetting layer and resulting in a rough film as shown by the spotty RHEED pattern in Figure 5.5(b). It then becomes essential to identify the exact thickness of excess metal required to induce surface segregation, and adsorb as close to that thickness as possible during each modulation scheme. Without further analysis, the exact transition between non-segregated conditions and segregated conditions is difficult to discern. A method of quantification of indium surface segregation is then developed to both further understand indium surface segregation and provide a more calculable means of *in situ* characterization.

5.4 Quantification of Surface Segregation Onset Dose

Now that a mechanism describing indium surface segregation during metal-modulated epitaxy is elucidated, data can be further analyzed examined using methods established in previous work [29]. Specifically, the time required to consume the adlayer upon closing the metal shutters is considered. If indium surface segregation has occurred, some of the metal supplied during the metal shutter open time will not be able to incorporate into the film. This effect should result in a smaller time required to reach a steady state after the metal shutters are closed relative to a non-segregated growth

condition. This experiment is performed both to determine the exact amount of metal required to induce surface segregation, herein called the surface segregation onset dose, and to strengthen the theory suggested in the qualification section above. To extract the thickness of the consumed layer, a general MBE growth equation is considered. The relationship between growth rate, incoming metal flux, adlayer accumulation, and adlayer desorption can be described with the equation

$$R_{Flux} = R_{Growth} + R_{Adlayer} + R_{Desorption} \tag{5.1}$$

where R_{Flux} is the rate of incoming flux, R_{Growth} is the rate of film growth, $R_{Adlayer}$ is the rate of adlayer accumulation, and $R_{Desorption}$ is the rate of adatom desorption from the surface. The low temperatures used for the growth of these InGaN samples allows for the assumption that desorption of the adlayer is negligible. Furthermore, when the metal shutters are closed, the flux term can be eliminated which simplifies to the following equation.

$$R_{Growth} = -R_{Adlayer} \tag{5.2}$$

This equation has been used to determine growth rate from the consumption of the known thickness of the bilayer in GaN (2.3 ML) [29]. It can also be used in this case for a known growth rate to determine the thickness of an unknown adlayer on the surface of the growing InGaN film, by

$$R_{Growth} = -\left(\frac{D_{Adlayer}}{t_{accumulation}}\right) = \frac{D_{Adlayer}}{t_{consumption}} \tag{5.3}$$

where $D_{Adlayer}$ is the thickness of the incorporated adlayer, and $t_{consumption}$ is the time required to consume this adlayer. It has been calculated from calibration samples for this work that this composition of ~20% InGaN has a growth rate of approximately 800 nm/hr for a particular modulation scheme. However, this growth rate takes into account the steady-state time between modulation schemes, shown by the flat, unshaded regions in Figure 5.2 and Figure 5.3 where no growth occurs. Furthermore, this measure of growth rate is dependent on each particular modulation scheme. If the steady-state period is eliminated by only considering the time where metal is present during growth [29], the film has been calculated to grow at approximately 900 nm/hr. This allows for a modulation-independent calculation of the thickness of the adlayer consumed into the film during the metal shutter closed period. With a known growth rate and a measurable time of adlayer consumption, the thickness of this consumed adlayer can be calculated and converted to monolayers.

The green region, the time to consume the metal adlayer, was monitored for two indium compositions and several metal shutter open times. The length of time of this region and shutter open times were averaged for several modulation cycles and plotted in Figure 5.6. The secondary y-axis of Figure 5.6 is the thickness of the metal adlayer accumulated onto the film calculated from the time elapsed to consume this adlayer.

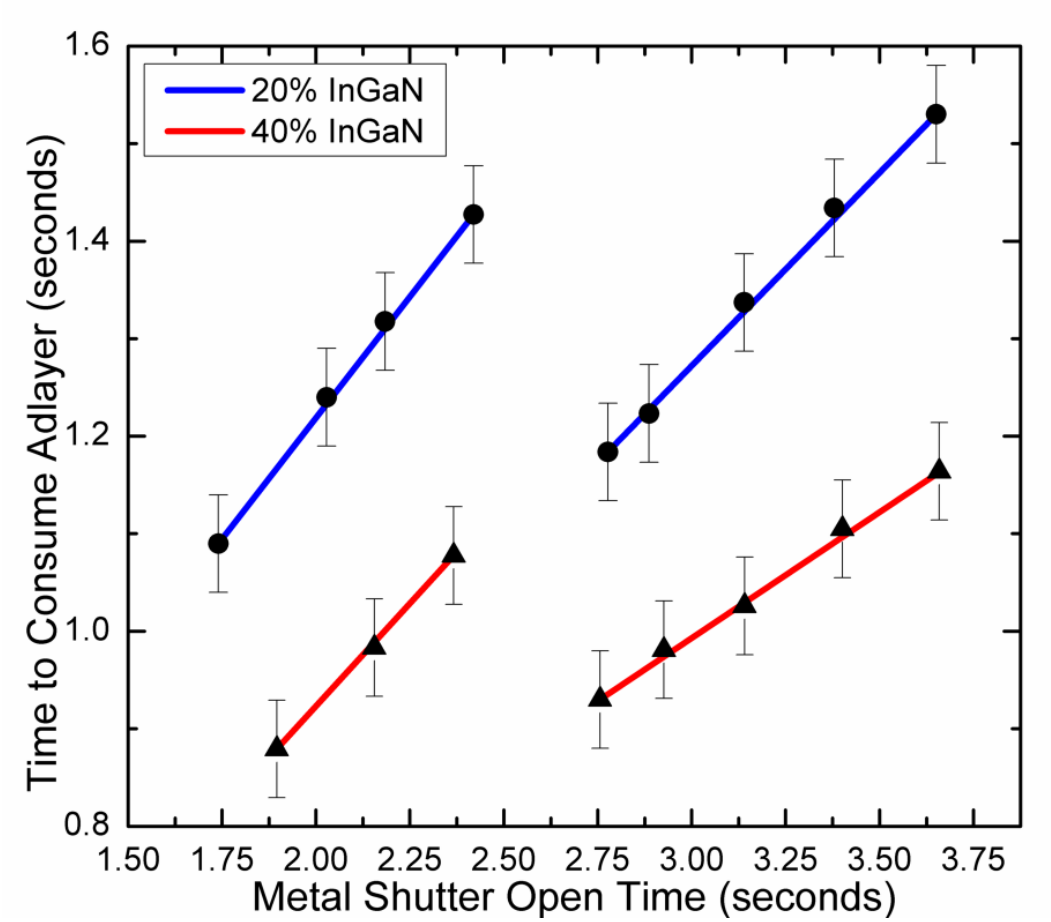

Figure 5.6: Time of consumption of metal adlayer and the corresponding adlayer thickness plotted versus metal-shutter open time for all conditions shown in Figure 5.2.

Shown in Figure 5.6 are both the time of consumption and thickness of the metal adlayer for several metal shutter open times during the growth of 20% and 40% InGaN. For both indium compositions, the time to consume the metal adlayer increases linearly until a certain metal shutter open time. After this point, the time to consume the adlayer decreases to a lower value, then linearly increases at a different slope than before. This break in linearity is attributed to the onset of indium surface segregation, which causes

indium to segregate on top of the gallium in the adlayer. In a segregated case, once the gallium-rich first monolayer of the adlayer is consumed, mostly indium remains on the surface and is prevented from incorporating into the film due to the substrate temperature being greater than needed for InN decomposition. This would cause the steady state regions shown in Figure 5.2 and Figure 5.3 to be reached sooner since the thickness of the adlayer that can consume into the film is effectively decreased.

The decrease in time to consume the metal adlayer occurs at approximately 1.45 seconds of growth to consume the adlayer into the film in the 20% InGaN case. Factoring the growth rate (900 nm/hr), c-spacing (0.532 nm), and number of metal layers per nitride unit cell (2), the thickness of the monolayer at the end of this metal shutter open time is 1.36 +/-0.05 ML. For 20% InGaN, an adlayer thickness above approximately 1.4ML will result in indium surface segregation. Similarly for the 40% InGaN case, the time to consume the adlayer is 1.1 seconds, which translates to surface segregation onset dose of 1.05 +/-0.05 ML.

The existence of a surface segregation onset dose (1-2ML) less than the droplet accumulation thickness (2-2.5ML) [6, 21, 32, 192] is significant. Because an intermediate regime does not exist at these low temperatures, unshuttered MBE growth will either produce droplets or result in dry, nitrogen rich growth. Thus, some form of modulation is required for high-quality, metal-rich InGaN growth in order to accumulate a certain amount of excess metal for its beneficial effects while preventing indium surface segregation.

5.5 Application of Metal-Modulated Epitaxy to High-Indium Content InGaN

The understanding and suppression of indium surface segregation has enabled higher indium content films to be grown, well within the InN-GaN miscibility gap. Shown in Figure 5.7 are x-ray diffraction scans of InGaN samples with varying indium contents from 22% to 72% and associated rocking curve full widths at half maximum (FWHM) for the <0002> symmetric reflections. Atomic force microscopy images with 30 nm height scales are shown on the right with inset root-mean-square roughnesses. Film thicknesses were measured from the thickness fringes visible in the x-ray diffraction scan for all samples. Each of the samples shown in Figure 5.7 exhibit single phase x-ray diffraction spectra with rocking curve FWHMs comparable to the GaN templates used to substrate these films (~350 arcseconds).

This method was independently confirmed by Gon Namkoong at Old Dominion University for thicker InGaN layers. Shown in Figure 5.8 are x-ray diffraction scans of single-phase InGaN samples, all with thicknesses of approximately 250 nm.

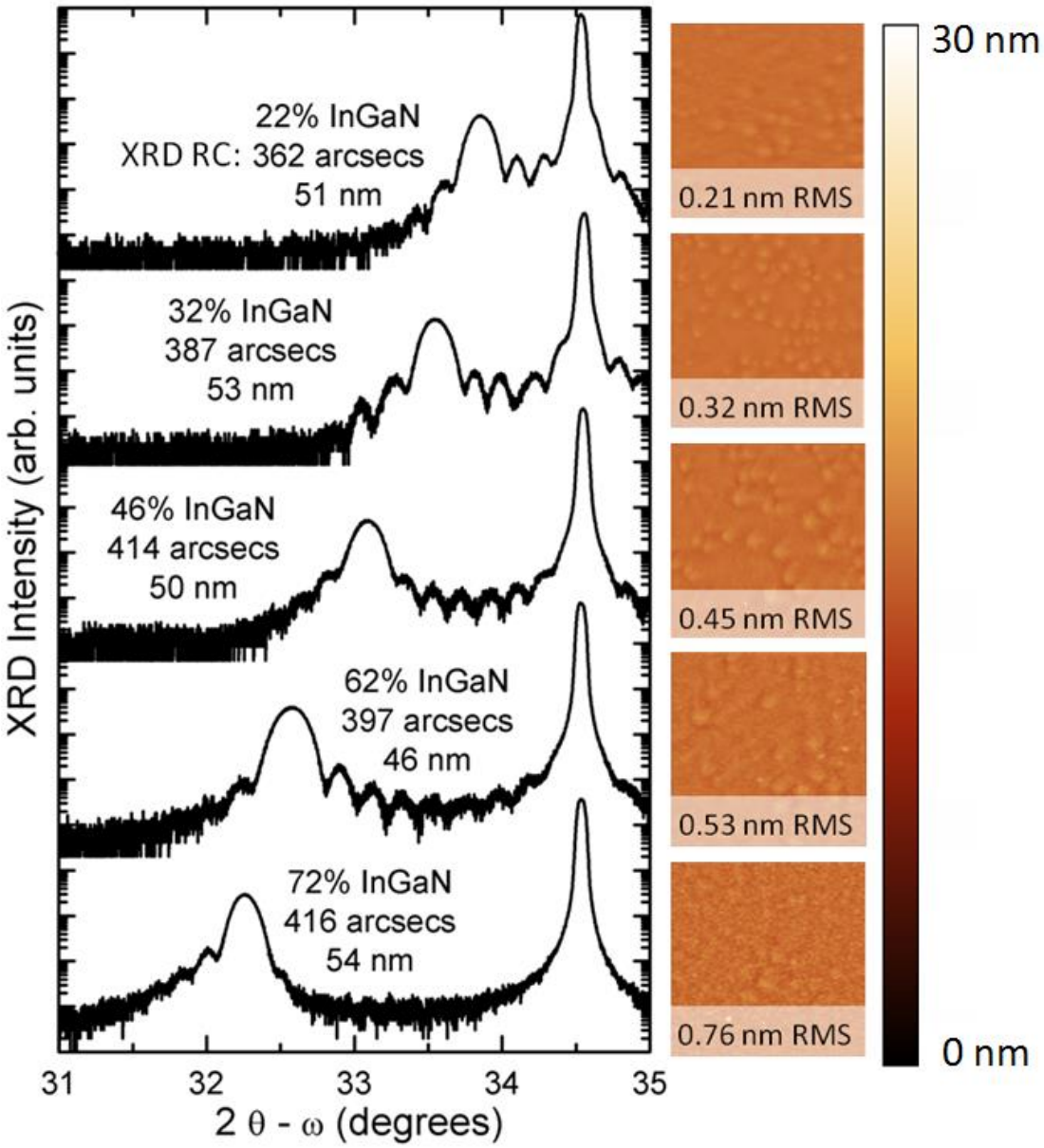

Figure 5.7: X-ray diffraction scans, rocking curves, and corresponding AFM morphologies of InGaN layers grown throughout the miscibility gap. AFM images have a 30 nm height scale and inset root-mean-square roughnesses.

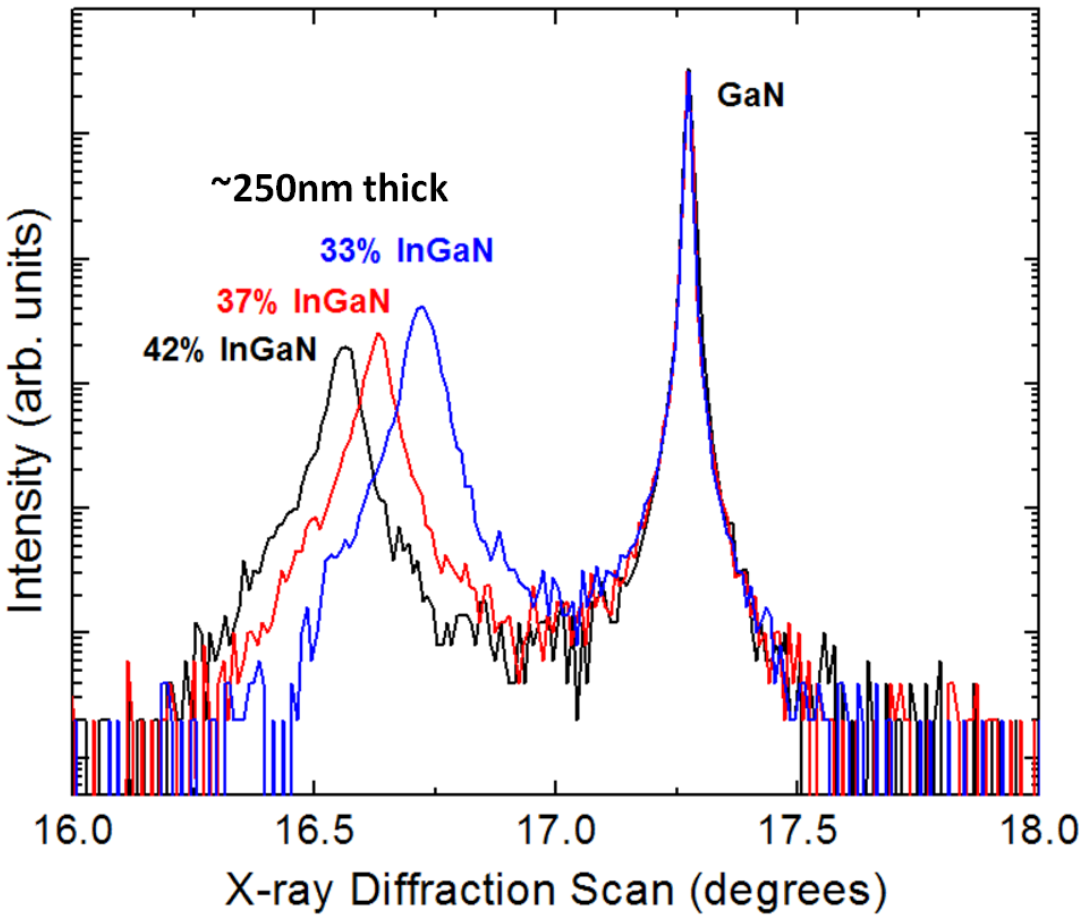

Figure 5.8: X-ray diffraction scans of independently grown InGaN layers, all at approximately 250 nm thick.

5.6 Conclusions

Metal-modulated epitaxy of InGaN has been investigated. A model has been developed regarding adlayer buildup and indium surface segregation based on RHEED patterns and transient RHEED intensities. This model was strengthened by a quantification of the indium surface segregation onset dose, which is found to be a value less than 2ML. These findings indicate that for metal rich growth of InGaN, some form of modulation will be required in order to suppress indium surface segregation while obtaining high-quality growth. Finally, these theories were tested by growing InGaN samples with varying compositions. Single-phase, high quality InGaN with compositions throughout the miscibility gap and RMS roughnesses less than 0.8 nm were obtained demonstrating the feasibility of shuttered, metal-rich InGaN growth.

CHAPTER 6: APPLICATION OF METAL-MODULATED EPITAXY TO InN

6.1 Introduction

For over two decades, the group-III nitride materials system has been the subject of rigorous investigation for its electronic and optoelectronic properties. Indium-bearing nitrides possess the unique capability of a bandgap that can be can be engineered from 0.7 eV (InN) to 3.4 eV (GaN), creating a wide array of applications in light-emitting and photovoltaic devices. Specifically InN is considered very attractive among the III-nitride binaries for its outstanding material properties and applications in electronics [125]. The first synthesis of this material from a melt was conducted in the early 1900s with limited success [193]. Polycrystalline films were then grown by sputtering in the 1970s and 1980s [194, 195], yielding preliminary measurements of the properties of this material. It was only in 1989 that the first growth of single-crystal InN was conducted [196], but with several limitations on the electrical and structural properties of the film created from the MOCVD growth technique. Although many of these issues have been mitigated in the growth of InN by MBE [197-199], there still exist many challenges with the growth of In-bearing nitrides in general.

InN, exhibiting by far the largest unit cell among the III-nitride binaries, currently has no native substrate for epitaxial growth [200]. Without a sufficiently lattice-matched substrate, these InN films form an extremely high density of structural defects [201]. Subsequently, the bonds from In to N in InN are the weakest among the nitride binaries,

mandating a relatively low growth temperature (300-600 °C) [125]. This temperature requirement poses a significant problem for MOCVD, as higher temperatures are generally required to liberate active nitrogen from ammonia. Similarly, MBE must be conducted at a lower substrate temperature to remain near or below the dissociation temperature of InN, sacrificing material quality usually collected from thermal energy. Grown InN films generally exhibit a high background electron concentration, creating challenges with p-type doping [202] and electrical measurement [203].

The constraints associated with the growth of InN growth suggest Metal-Modulated Epitaxy (MME) as a potential growth candidate, which has been successfully used for AlN [23, 24], and GaN [28, 29]. MME is a low-temperature growth technique applied to group-III nitrides in which metal and dopant cell shutters are periodically opened and closed while the active nitrogen flux remains constant. This technique generally uses extremely metal-rich fluxes that would rapidly accumulate droplets in traditional molecular beam epitaxy, exploiting the enhanced adatom diffusion supplied by an excess metal layer [32]. However, periodic closing of the metal and dopant cells allows this excess metal to be consumed into the film, providing abrupt interfaces. The low temperatures used during MME avoid desorption of adatoms from the substrate, thereby reducing sensitivity to temperature variations and increasing growth uniformity. MME has been shown to significantly advance p-type doping in GaN [43-45], resulting in hole concentrations in the 10^{19} cm^{-3} range. Furthermore, MME can be used in concert with transient reflection high energy electron diffraction (RHEED) intensities, providing a unique *in situ* characterization method with observation and control of fractions of metal monolayers [29-31].

The objective of this study is to apply Metal-Modulated Epitaxy to the growth of InN to explore metal-rich growth at extremely low temperatures. The surface kinetics of InN grown by MME are discussed and related to those previously elucidated for GaN and AlN. A method of reducing the background electron concentration of grown InN films by the modification of shutter modulation scheme is attempted. Finally, the structural and electrical properties of these films are shown.

6.2 Experimental Setup

All samples reported herein were grown in a Riber 32 MBE chamber. A Veeco Unibulb plasma was used to supply active nitrogen species and operated with a flow rate of 1.3 standard cubic centimeters per minute operated at 350 W. Aluminum and indium were supplied by standard effusion cells. Sapphire wafers with MME grown AlN were used to substrate InN to electrically isolate the layers for Hall effect characterization. All substrates were backside sputtered with 1 μ of Ta to provide uniform radiative heating in vacuum and cleaned in H_2SO_4:H_2O_2 (4:1) prior to being loaded into the introductory chamber and outgassed at 160 °C for 30 minutes.

Metal and dopant cells were opened and closed simultaneously, while the active nitrogen supply to the growth surface remained constant. The aluminum flux used for AlN buffers was 5.5×10^{-7} Torr BEP. Substrate temperatures were 750 °C for AlN buffer growth and 275 °C for InN growth. The shutter schemes for AlN and InN were calibrated to grow metal-rich films without droplet formation [23, 29]. RHEED patterns were recorded both during growth and after cooldown under a nitrogen plasma.

Electrical properties of the InN films were obtained using a custom Hall-effect system. This Hall system consisted of a 0.3 Tesla fixed magnet and high-precision Keithley electronics, including a model 2128A nanovoltmeter, a model 6221 current source operating in DC mode, and a model 7001 switch matrix with a hall measurement card. Additionally, the Hall measurement procedure discussed in this chapter follows ASTM Standard F76 [204].

6.3 Growth of Metal-Rich InN by Metal-Modulated Epitaxy

Approximately 500 nm of unintentionally-doped indium nitride was grown via MME on a MME-grown 100 nm AlN/sapphire substrate. A shutter modulation scheme of 10 seconds of metal shutter open time followed by 6 seconds of metal shutter closed time was employed. The indium flux was chosen to obtain metal-rich growth, while still consuming all excess metal into the film each modulation cycle. Shown in Figure 6.1 is the transient RHEED intensity of the specular streak recorded during this growth. The shaded regions indicate time when the metal shutters were opened, while the clear regions indicate time where only active nitrogen was impingent upon the surface..

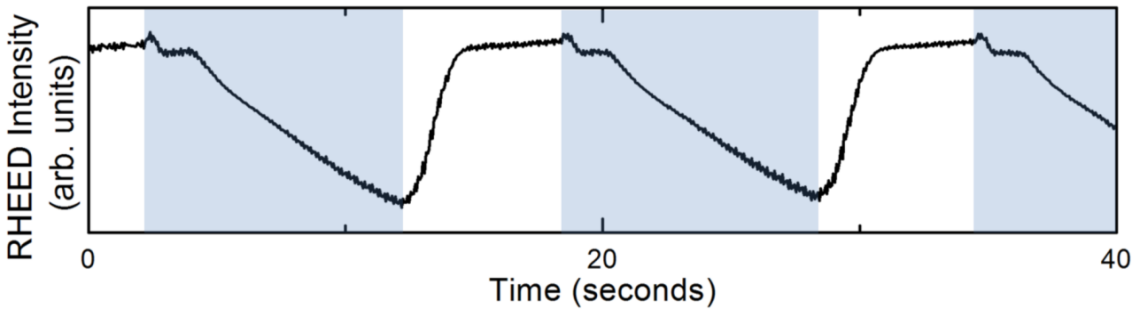

Figure 6.1: Transient RHEED intensity recorded during the growth of InN with a shutter modulation scheme of 10 seconds indium shutter open time and 6 seconds indium shutter closed time. Shaded regions indicate where the indium shutter was open.

The decrease in RHEED intensity upon opening of the metal shutters seen in Figure 6.1 is attributed to the accumulation of excess metal on the growth surface [23, 32, 33]. The subsequent increase in the intensity of the RHEED streak therefore corresponds to the consumption of the excess indium into the film. This behavior is strikingly similar to what has been previously observed before for MME growth of GaN [29] and AlN [24]. This sample was then electrically characterized by Hall-effect analysis and exhibited a resistivity of 3.75×10^{-3} Ω-cm, a mobility of 700 cm^2/Vs, and an electron concentration of 2.4×10^{18} cm^{-3}. Structural characterization via x-ray diffraction revealed (0002) and (10$\bar{1}$ 4) rocking curves of 1055 arcseconds and 747 arcseconds, respectively. These figures of merit are respectable in comparison to recent reports in literature [205-207], when considering the thickness of these layers grown directly on an AlN buffer.

Considering the difficulty in measuring bulk InN electrical properties as a result of a surface inversion layer [208, 209], bulk InN carrier concentrations are not claimed in this chapter. Instead, only the Hall results are reported in the same manner as the literature used in comparison [205-207].

6.4 Effect of Growth Conditions on Background Electron Concentration in InN

Some authors have attributed the often-observed high background electron concentration of metal-rich MBE-grown nitride layers to the existence of nitrogen vacancies [210]. This idea has been challenged by more recent theoretical reports [143, 211], citing that the nitrogen vacancy is a high-energy defect in nitrides and unlikely to be responsible for n-type conductivity. Still, prominent experts on GaN electrical characterization assert that the nitrogen vacancy must be the source of residual n-type conductivity in unintentionally-doped group-III nitrides [212]. The Metal-Modulated Epitaxy growth technique provides a unique opportunity to explore this possibility.

As discussed in Chapter 2, the growth surface alternates between a wet, metal-covered area to a dry, nitrogen impingent area during MME. If the metal-rich growth generates nitrogen vacancies when the metal shutters are open, it is plausible that some of these vacancies may be periodically filled by the diffusion of nitrogen into the film [213] when the metal shutters are closed. An illustration of this periodic *in situ* nitrogen anneal is shown in Figure 6.2. To this end, a second sample was grown with the same conditions but with a longer metal shutter closed time of 20 seconds. The length of the growth was increased to compensate for the additional time during the modulation scheme where no growth was occurring. The transient RHEED intensity recorded of the specular streak during growth is shown in Figure 6.3.

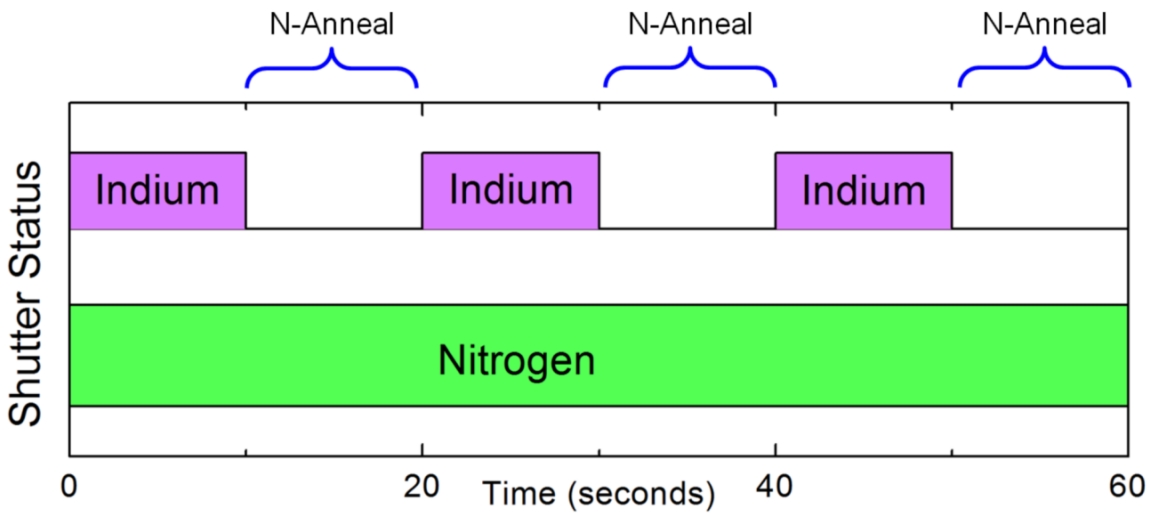

Figure 6.2: Illustration of the metal-modulated epitaxy shutter scheme. The areas where metal is not impingent upon the surface are labeled as "N-Anneal."

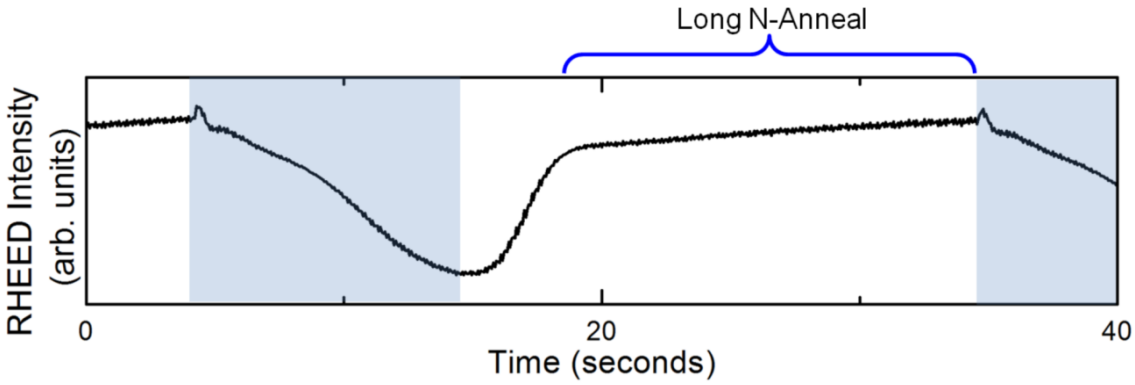

Figure 6.3: Transient RHEED intensity recorded during the growth of InN with a shutter modulation scheme of 10 seconds indium shutter open time and 20 seconds indium shutter closed time. Shaded regions indicate where the indium shutter was open.

This second 500 nm InN sample was then electrically characterized by Hall-effect analysis and exhibited a resistivity of 2.46×10^{-3} Ω-cm, a mobility of 590 cm^2/Vs, and an electron concentration of 4.1×10^{18} cm^{-3}. Structural characterization via x-ray diffraction revealed a (0002) and ($10\bar{1}\,4$) rocking curves of 1050 arcseconds and 813 arcseconds, respectively. The qualitative x-ray diffraction analysis suggests that these two samples are structurally very similar.

The longer *in situ* nitrogen anneal had no appreciable effect on the electrical properties of the grown InN layers. A possible cause for this result is that the growth pressure (10^{-5} Torr) used for these experiments may be too low to eliminate nitrogen vacancies. A high-pressure growth environment may provide a setting to fill these nitrogen vacancies, but further studies are necessary to explore this possibility.

6.4 Conclusions

In this chapter, the 500 nm thick layers of InN grown by MME on AlN/sapphire are discussed. Structural and electrical characterizations of these layers agree well with that found in the literature for similar thicknesses on similar substrates. Growth conditions were then modified in an attempt to reduce the background electron concentration. Specifically, the time of the shutter modulation scheme where only nitrogen is impingent upon the surface is increased in an attempt to reduce nitrogen vacancies. This process had no appreciable effect on the background electron concentration, while having very little effect on structural quality.

CHAPTER 7: APPLICATION OF METAL-MODULATED EPITAXY TO Mg-DOPED $Al_xGa_{1-x}N$ ALLOYS

7.1 Introduction

The outstanding properties of the aluminum gallium nitride materials system have encouraged a great deal of research towards micro- and optoelectronic devices [113, 150, 214]. Specifically, the tunable bandgap between 3.4 eV (GaN) and 6.2 eV (AlN) makes this materials system enticing for ultraviolet (UV) light-emitters and photovoltaics [215, 216]. High breakdown fields common among all group-III nitrides have been exploited for currently commercialized high-power electronics [68, 152]. These materials could be further utilized in space applications due to their substantial radiation hardness [75]. AlGaN alloys have an enormous array of potential applications such as air and water purification, medical phototherapy, solar-blind detectors/emitters, high power electronics, and high frequency devices [47, 72].

These alloys are not without challenges of implementation, however. AlGaN is typically grown at higher substrate temperatures than GaN or InGaN [141, 167]. Thus, temperature fluctuations and desorption of reactant species can alter growth conditions at an exponential rate. Furthermore, AlGaN alloys remain difficult to p-type dope [217] and UV wavelength emitters suffer from reduced external quantum efficiencies [215]. This decrease in efficiency arises from the deeper acceptor state occupied by p-type dopants in AlGaN alloys versus the GaN binary [218]. The activation energy for holes in traditionally-grown GaN is relatively high (160-170 meV), but the activation energy for

holes in AlGaN increases with rising Al content. The deep acceptor requires more energy to produce holes, making the p-type conductivity required for working diode structures difficult to obtain using standard growth techniques [174, 182].

The transient RHEED analysis technique developed for Metal-Modulated Epitaxy (MME) provides an environment where adlayer quantity can be monitored *in situ* and adjusted accordingly by changing effusion cell temperatures. Similarly, the recent success in p-GaN grown by Metal-Modulated Epitaxy (MME) suggests this technique as a promising candidate for p-AlGaN growth. The effective activation energy of holes in GaN has been drastically reduced as a result of an increased concentration of electrically active Mg [219]. This success was attributed not to the increase of Mg concentration in the film, but to an increase of the electrical activation efficiency of the Mg dopants.

The objective of this study is to apply Metal-Modulated Epitaxy to the growth of AlGaN layers towards the stabilization of unintentionally-doped AlGaN growth and increasing the concentration of electrically active Mg dopants in p-AlGaN layers. Improvements in the electrical and structural quality of these alloys will not only improve the efficiencies of current devices, but also enable novel device designs.

7.2 Experimental Setup

All growths described in this chapter were conducted in a Riber 32 MBE system. A standard effusion cell was used to supply aluminum, while a Veeco SUMO cell was used to supply gallium. Magnesium was delivered by a water-cooled Veeco corrosive series valved cracker, operated at a bulk temperature of 300 °C and a tip temperature of

900 °C. The cracker valve was set to 120 mils during p-type nitride growth, corresponding to a previously measured flux of approximately 1×10^{-9} Torr BEP. The nitrogen source was a Veeco Unibulb RF plasma source, operated at 350 W with a flow rate of 1.3 sccm. MOCVD-grown 4 μm thick AlN layers were back-side metalized with 1.5 μm of Ta and used as pseudosubstrates. Before loading into the growth chamber, a 30 minute outgas at 150 °C in an introductory chamber was performed for each sample. Approximately 100 nm of AlN was deposited on these substrates using MME conditions to provide a smooth, clean surface for AlGaN growth. These AlN buffers were grown at a substrate temperature of 850 °C using an extremely metal-rich Al flux at a shutter modulation scheme of 30 seconds Al shutter open time followed by 30 seconds of Al shutter closed time..

Three AlGaN samples were grown with varying aluminum compositions. All AlGaN layers were grown at a substrate temperature of 600 °C, and had a targeted thickness of 70 nm. Accurate total metal fluxes for differing flux compositions were obtained by normalizing by the Z-number to account for ion gauge sensitivity differences between Al and Ga. Both the aluminum and gallium shutters were periodically opened and closed simultaneously, while nitrogen flow to the growth surface was kept constant.

Three Mg-doped AlGaN samples were grown, all employing metal-rich fluxes and targeting 70 nm in thickness. A Mg-doped GaN sample was grown at the same thickness as a control set. All AlGaN and GaN layers were grown at a substrate temperature of 600 °C. Aluminum, gallium, and magnesium shutters were periodically opened and closed simultaneously to consume excess metal resulting from the metal-rich conditions, while nitrogen flow to the growth surface was kept constant. The shutter

modulation scheme used for all p-type growths was 5 seconds of all metal shutters open time followed by 10 seconds of metal shutter closed time.

Electrical properties of the AlGaN films were obtained using a custom Hall-effect system. This Hall system consisted of a 2 Tesla electromagnet and high-precision Keithley electronics, including a model 2128A nanovoltmeter, a model 6221 current source operating in DC mode, and a model 7001 switch matrix with a hall measurement card. Additionally, the Hall measurement procedure discussed in this chapter follows ASTM Standard F76 [204].

7.3 Structural Analysis of AlGaN Layers

Shown in Figure 7.1 are x-ray diffraction scans of the AlGaN layers. On the right side of each diffraction scan is the AlN pseudosubstrate, while the peak on the left of each scan represents the AlGaN peak. The fringes surrounding the AlGaN peak are Pendellösung fringes [220, 221], providing a qualitative measure of the quality and smoothness of these layers. Film thicknesses of 65-75 nm were extracted from the period of these fringes for all samples, which agrees well with the targeted thickness of 70 nm. The aluminum compositions of these AlGaN layers were found to be 2.9%, 8.3%, and 19.8% by Vegard's Law [222]. X-ray rocking curves were obtained from the symmetric (0002) peak of each AlGaN layers. The FWHM of the RC of the 2.9%, 8.3%, and 19.8% p-AlGaN layers were found to be 461, 281, and 179 arcseconds, respectively.

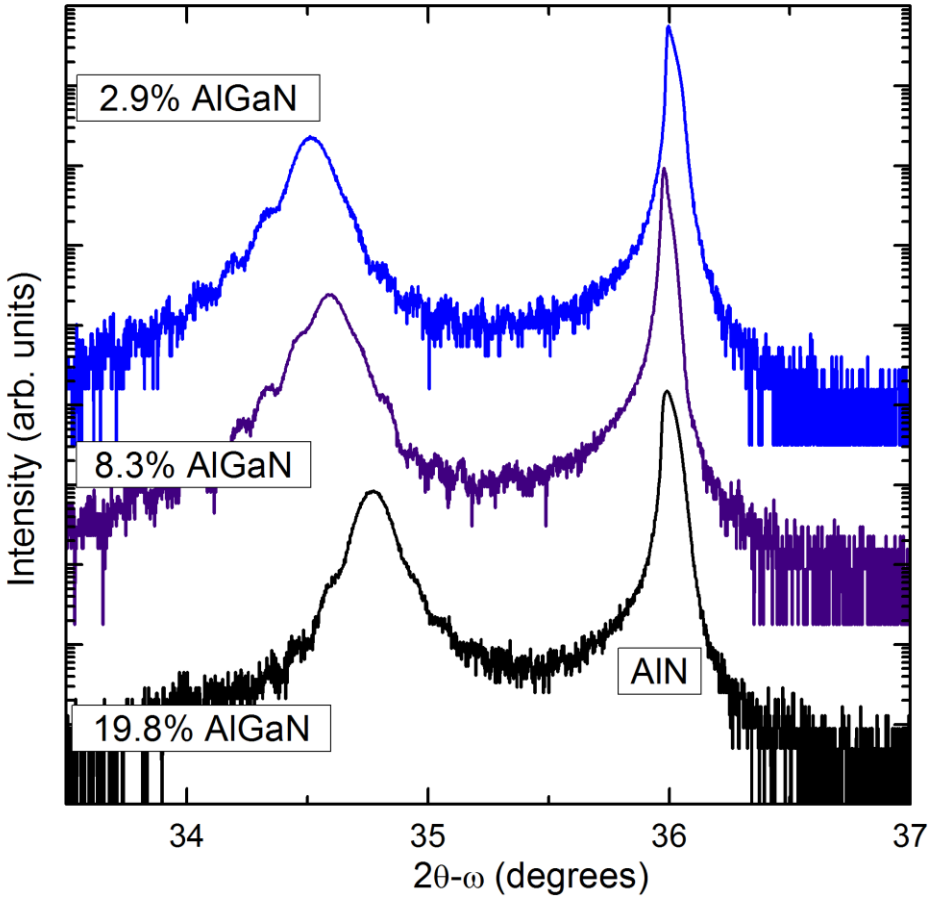

Figure 7.1: X-ray diffraction spectra for AlGaN layers of three different compositions grown by Metal-Modulated Epitaxy

7.4 RHEED Analysis of AlGaN Growth

Shown in Figure 7.2 is a transient RHEED intensity representative of all layers grown in this chapter. The shaded regions indicate where the aluminum and gallium shutters were open. Before opening the metal shutters, there is a steady state, flat intensity where no growth occurs. Once the metal shutters have been opened, the intensity decreases at two different rates. This behavior of the RHEED intensity is very

similar to that shown in the low gallium flux case of Figure 2.3 shown in Chapter 2. The two different rates of intensity decrease are attributed to the adsorption of the first and second monolayers of excess metal [5, 6]. Following the closing of the metal shutters, the RHEED intensity then increases as this excess metal is consumed into the film, resulting in a dry, crystalline surface. Subsequently, the steady state period is reached and the cycle begins again. These transient RHEED intensities are very similar to that previously found for GaN [29] and AlN [23, 24], demonstrating the versatility of the MME technique.

It is also worth noting that there is no evidence of surface segregation seen in the transient RHEED intensities or the x-ray diffraction spectra of the AlGaN layers. InGaN alloys grown previously by the MME technique at similar growth conditions exhibited XRD peak broadening from phase separation, InN surface cluster formation, and a signature in the RHEED transient attributed to indium surface segregation. However, none of these characteristics are seen in the AlGaN layers. This experiment concludes that gallium surface segregation in AlGaN growth is much less of a concern than indium surface segregation in InGaN.

Shown in Figure 7.3 is a RHEED image representative of all layers grown in this chapter. This RHEED pattern is very similar to that recorded previously for highly p-type GaN films [44, 153, 223]. MME has been shown to combine the enhanced substitutional site placement of Mg during N-rich growth with the increased structural quality provided by metal-rich growth. The streaky-spotty nature of this pattern, as opposed to a completely spotty pattern, reveals that sufficient material quality and surface smoothness is being maintained during the MME process.

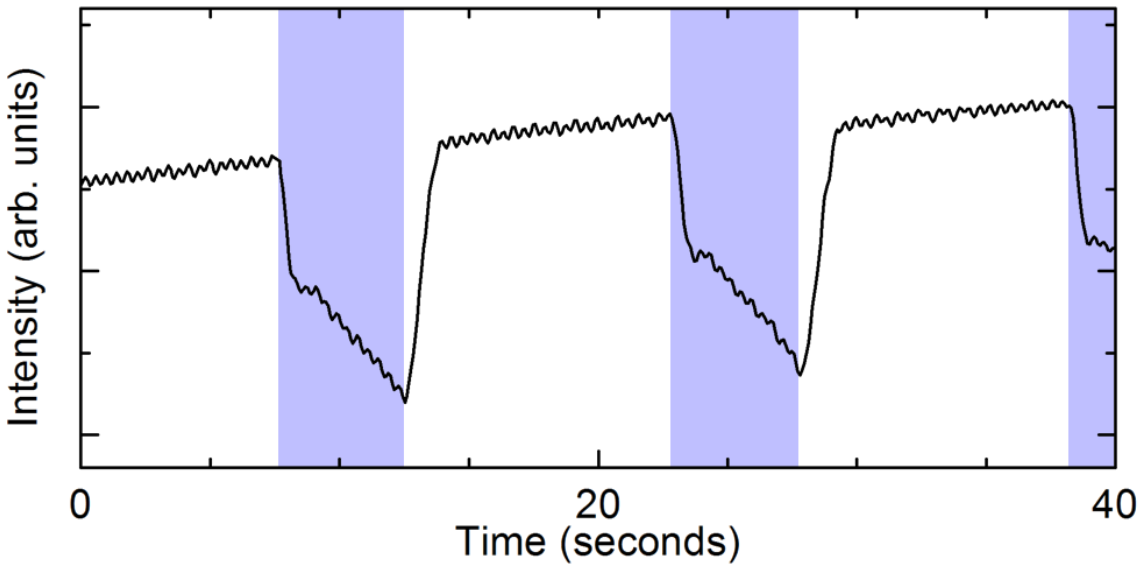

Figure 7.2: Representative transient RHEED intensity recorded during growth for all samples discussed in Chapter 7. The shaded regions indicate where the metal shutters were open. These RHEED signatures are very similar to that described for GaN in Chapter 2.

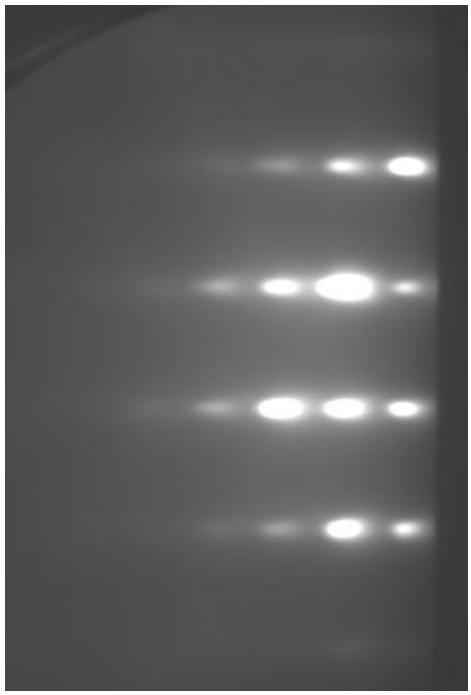

Figure 7.3: Representative RHEED pattern at the end of growth for all samples discussed in Chapter 7. The spotty-streaky RHEED pattern agrees well with that previously seen for high hole concentration GaN grown by MME [223].

7.5 Electrical Analysis of AlGaN Layers

After growth, these films were characterized by room-temperature Hall effect analysis. The resistivities recorded for all samples are shown in Figure 7.4. As expected, the p-GaN sample was the most conductive with a resistivity of approximately 0.5 Ω-cm. The 2.9% AlGaN sample was more resistive, with an average resistivity of approximately 2.7 Ω-cm. The 8.3% AlGaN sample was even more resistive, with an average resistivity of approximately 2.9 Ω-cm. Finally, the 19.8% AlGaN sample was the most resistive, with an average resistivity of 70 Ω-cm. These electrical results agree with that expected from the literature, such that a higher aluminum composition produces a deeper acceptor [218].

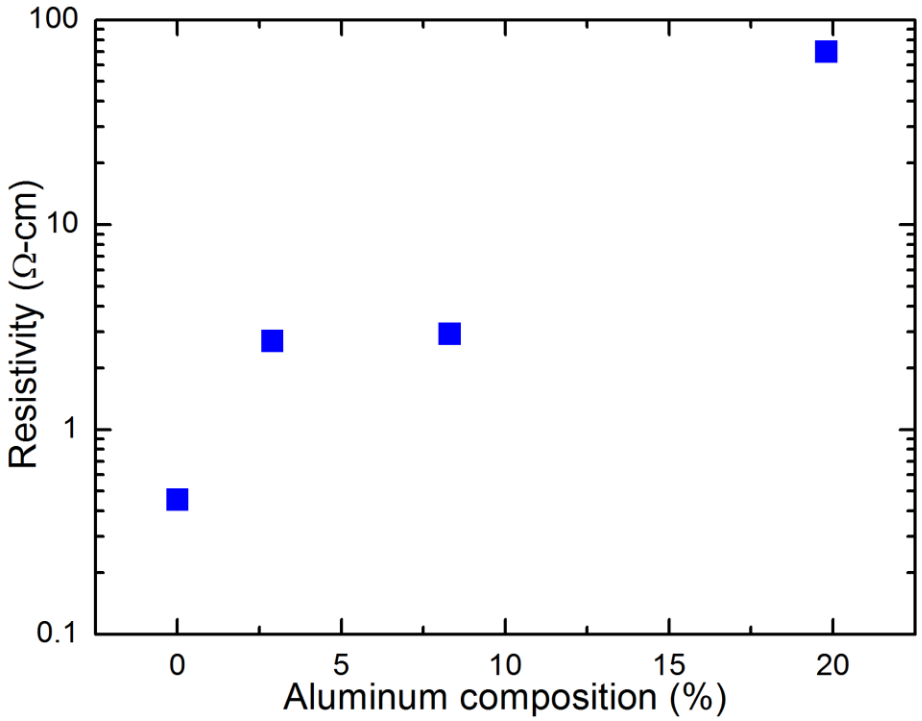

Figure 7.4: Resistivities of Mg-doped GaN and AlGaN samples. As the targeted aluminum composition of the film increased, the resistivity increased, agreeing well with that expected from the literature [218].

The hole concentrations of these samples were also extracted and are shown in Figure 7.5. The p-GaN, 2.9% p-AlGaN, and 8.3% p-AlGaN samples each had positive hall coefficients in good agreement with each other. The 19.8% p-AlGaN exhibited mixed Hall conductivity. This mixed conductivity is attributed to a very low mobility of charge carriers. As a result, only the GaN, 2.9% AlGaN, and 8.3% AlGaN results are shown. It is worth noting that although the 19.8% AlGaN samples exhibited mixed conductivity, the hot probe technique confirmed that the film was overall p-type.

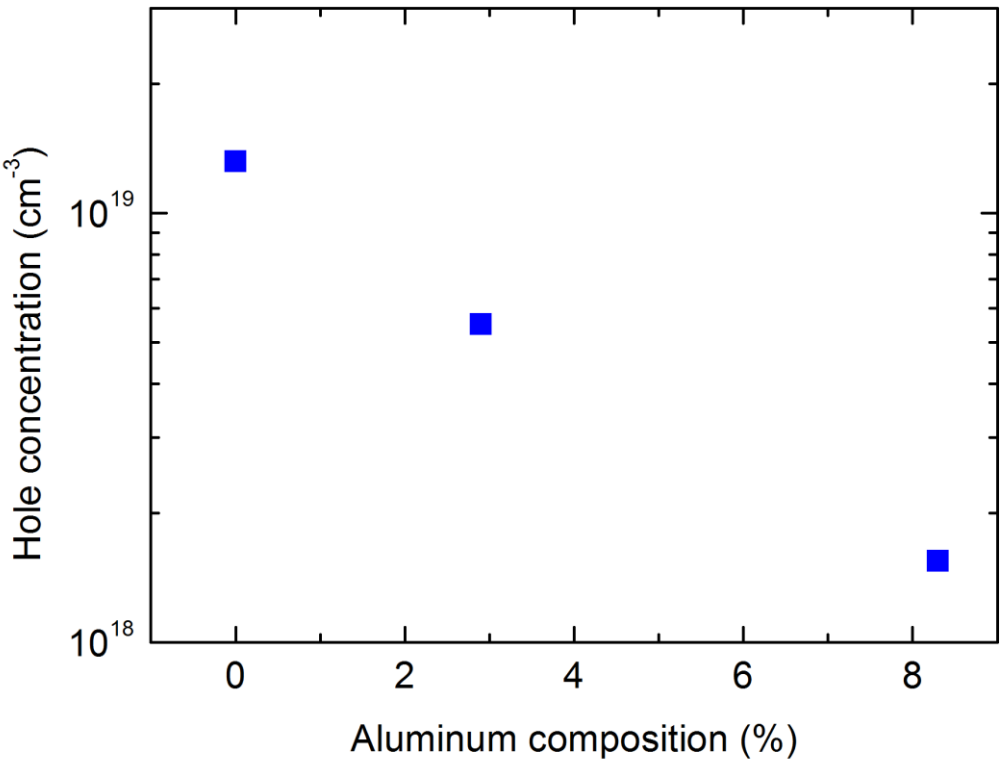

Figure 7.5: Hole concentrations of Mg-doped GaN, 2.9% AlGaN, and 8.3% AlGaN. Although the hot probe technique detected that the 19.8% AlGaN sample was p-type, Hall effect characterization detected mixed conductivity.

As shown in Figure 7.5, the hole concentrations detected for p-GaN, 2.9% AlGaN, and 8.3% AlGaN were 1.32×10^{19} cm^{-3}, 5.8×10^{18} cm^{-3}, and 1.55×10^{18} cm^{-3}, respectively. The mobilities for these samples were 1 cm^2/Vs, 0.4 cm^2/Vs, and 1.4 cm^2/Vs, respectively. Considering the much higher hole concentrations previously obtained for GaN [29, 153, 219], it is clear that the growth conditions used in this experiment were unoptimized. Nonetheless, these very high hole concentrations detected for these AlGaN layers demonstrate the feasibility [224-226] of the MME growth technique for Mg-doping in AlGaN alloys.

7.6 Conclusions

In this chapter, Metal-Modulated Epitaxy is applied to the growth of Mg-doped AlGaN layers. The crystal quality of these layers was found to be very high, demonstrating that AlGaN layers can be feasibly grown by MME. Transient RHEED intensity analysis was found to be similar to that found for AlN and GaN, indicating that MME can control excess metal accumulation to fractions of metal monolayers. RHEED patterns recorded for the GaN control and AlGaN experimental layers all agreed well with those previously seen for high hole concentration samples grown by MME. The p-GaN control samples exhibited the lowest resistivity, while the 2.9%, 8.3%, and 19.8% targeted AlGaN had higher resistivities, increasing with Al content. The maximum hole concentration observed for AlGaN was 5.8×10^{18} cm^{-3}, demonstrating that MME is a viable technique for the growth of bulk p-type AlGaN layers without the need for polarization- or short period superlattice-induced techniques.

CHAPTER 8: ATTEMPT GROWTH OF HIGH-QUALITY $Al_xGa_{1-x}N$ LAYERS ON A LATTICE-MATCHED SUBSTRATE

8.1 Introduction

The group III-nitride materials system has an outstanding set of properties that facilitate a wide array of electronic [227-229] and optoelectronic [230-232] device applications. Specifically, these materials have a tunable, direct bandgap from 6.2 eV (AlN) [233] to 0.7 eV (InN) [61], along with high breakdown fields [69], thermal conductivities [71], and thermal stabilities [46]. However, the large difference in lattice constants from AlN ($a_{AlN} = 3.112\,\text{Å}, c_{AlN} = 4.982\,\text{Å}$) to InN ($a_{InN} = 3.533\,\text{Å}, c_{InN} = 5.693\,\text{Å}$) inherently leads to a lack of a native substrate. This lack of a lattice-matched substrate results in the propagation of defects from strain relaxation [186]. These defects do much to hinder device performance, producing non-radiative recombination centers, reducing minority carrier lifetimes, reducing thermal conductivity and introducing energy states into the bandgap [67]. The mitigation of these detrimental properties has been a primary focus in the III-nitride growth community for almost 30 years [85, 122, 166].

Single crystalline aluminum oxide, known as sapphire, remains the most commonly used substrate for III-nitride growth [67]. This substrate has a mismatch of approximately 14% to GaN, resulting in a very high dislocation density of usually 10^{-10} cm^{-2} in epitaxially grown films [234]. Much effort has been invested in the amelioration of these defect densities, since available bulk sapphire substrates are cheap and of high

structural quality. One of these defect-reduction techniques is a nitridation step, which converts a thin surface layer of sapphire into AlN, enhancing subsequent GaN nucleation [158-161]. Another technique common among many epitaxial processes is the use of a low-temperature buffer layer [235], which enhances coalescence of islands and increases grain sizes [236, 237]. A popular utilization of these developments is the growth of 4-10 μm of GaN or AlN buffers on sapphire substrates, terminating dislocations through thick growth [114]. These nitride pseudosubstrates or templates can be tailored to the needs of the consumer, but are often expensive. Despite these advances in dislocation reduction, this substrate still exhibits a different coefficient of thermal expansion than GaN, yielding thermally-induced stress [238]. Sapphire is also thermally and electrically non-conductive, reducing heat dissipation and prohibiting the use of the substrate as a contact to the film [67]. Finally, sapphire is very resistive to lapping and etching, making substrate removal difficult [239].

Silicon carbide (SiC) is another preferred substrate for the growth of III-nitrides. This material has only a 3% mismatch to GaN and is much more thermally conductive than sapphire [240]. SiC is also a polar material, potentially enabling control of the polarity of grown III-nitride films [241]. Electrically conductive SiC can also be purchased, facilitating the use of the substrate as a backside contact. However, some disadvantages also accompany the use of this substrate. There is poor wetting and adhesion of GaN layers grown directly on SiC [242]. This problem is alleviated by the use of an AlN or AlGaN buffer [243], but in turn produces a highly resistive region between grown devices and the substrate. Finally, although high-quality SiC is readily available, these substrates are expensive.

Silicon has long been an appealing substrate candidate for III-nitride epitaxial growth. This material is available with very low prices and very high qualities as a result of its mature development and large-scale production [67]. Silicon has demonstrated a great deal of promise not only as a substrate [244] but also as an electrical component of the device in III-nitride epitaxy [245]. Nonetheless, there are significant hurdles to overcome. The Si (111) plane, generally chosen for hexagonal nitride growth because of its trigonal symmetry, has a lattice mismatch of 17% to GaN [246]. In addition, silicon has a tendency to form an amorphous Si_xN_y layer at the GaN/Si interface [247]. This amorphous layer is prevented by the growth of an intermediate AlN layer [248], but this highly resistive buffer reduces the electrical conductivity between the nitride device and the substrate. At high growth temperatures, group-III metals and silicon form an amorphous mixture through a eutectic chemical reaction [249, 250]. This reaction results amorphous nucleation layers and subsequent growth of defective material [251].

The limitations of the above-mentioned substrates provide a great deal of incentive to explore new alternatives. Devices employing large areas, complicated structures, or high power densities would suffer greatly from defects propagated from state-of-the-art nucleation and growth techniques using standard substrates [50, 252]. Lithium gallate ($LiGaO_2$) is a substrate that removes many of these restrictions and provides a feasible alternative to current III-nitride substrates.

Inexpensive, Czochralski-grown $LiGaO_2$ has been studied since 1965 for its piezoelectric properties, so much of its inherent properties are well-known [253]. First determined as having an orthorhombic crystal structure, lithium gallate was found to have quasi-hexagonal symmetry with a lattice mismatch to GaN of only 1-2% [67, 121].

$LiGaO_2$ is a polar material, potentially facilitating the growth of either Ga-polar or N-polar material on either the Li, Ga-terminated or O-terminated surface, respectively. Although nitride films exhibit poor adhesion and tend to peel off if grown on the oxygen terminated surface [163], Ga-polar films grown on the lithium terminated surface adhere well and can be easily transferred to another host. The surface polarity and termination of the transferred film can be chosen by the transfer process, either bonded substrate removal or epitaxial lift-off [120]. The only buffer layer needed to enhance film adhesion is a simple, thin, nitrogen-rich nucleation layer [167]. The lattice mismatch between GaN and $LiGaO_2$ is very impressive, but this substrate is capable of 0% biaxial mismatch to AlGaN. AlGaN with a 12.5% Al content can be lattice matched to $LiGaO_2$ at growth temperature (700 °C), while AlGaN with a 45% Al content can be lattice matched to $LiGaO_2$ at room temperature [165]. These properties make lithium gallate an excellent candidate for AlGaN growth.

The objective of this study is to evaluate the growth of AlGaN layers on a lattice-matched substrat. AlGaN layers with varying aluminum compositions are grown on $LiGaO_2$ substrates. These layers are characterized by x-ray diffraction to evaluate aluminum content, layer thickness, and structural quality. The feasibility of lithium gallate as a substrate for AlGaN growth is evaluated.

8.2 Experimental Setup

All growths described in this chapter were conducted in a Riber 32 molecular-beam epitaxy (MBE) system using the Metal-Modulated Epitaxy (MME) growth technique. A Veeco SUMO cell was used to supply gallium, while a standard effusion cell was used to supply aluminum. A Veeco Unibulb plasma source was used to supply active nitrogen to the growth surface, and was operated at 350 W with a flow rate of 1.3 standard cubic centimeters per minute. Custom-polished (1 Å rms roughness) lithium gallate substrates were used for all growths, with the 5.014 Å lattice spacing parallel to the growth direction. All substrates had 1 μm of tantalum sputtered on the rough backside to ensure uniform radiative heating. The substrates were solvent cleaned with trichloroethylene, acetone, and methanol for 30 minutes each in a sonic bath. Each substrate was outgassed at 150 °C for 30 minutes in an introductory chamber before being loaded into the growth chamber.

Before growth, a nitrogen-rich GaN buffer with a III/V ratio of approximately 1:5 was deposited for 1 minute at 600 °C to ensure film adhesion [29]. AlGaN layers were then grown at 600 °C targeting 10%, 15%, and 20% aluminum compositions and are described here as Samples A, B, and C, respectively. The AlGaN layers had a targeted thickness of approximately 125 nm, and employed a III/V ratio of approximately 1.5:1. In order to consume the excess metal accumulated as a result of these metal-rich conditions, a shutter modulation scheme of 5 seconds shutter open time followed by 5 seconds shutter closed time was employed. These growth conditions are summarized in Table 8.1.

Table 8.1: Growth conditions employed for the growth of AlGaN layers on $LiGaO_2$.

	Al/Ga Flux Ratio (%)	Total metal flux (normalized by Z, Torr BEP)	III/V ratio	Measured Al composition (%)
Sample A	10	0.35×10^{-7}	1.5	9.2
Sample B	15	0.35×10^{-7}	1.5	14.1
Sample C	20	0.35×10^{-7}	1.5	21.1

8.3 Structural Analysis of AlGaN Layers by X-ray Diffraction

X-ray diffraction spectra recorded from each sample after growth are shown in Figure 8.1. The lithium gallate substrate produces a peak shown on the right side of each scan, corresponding to a lattice spacing of 5.013 Å. This is in good agreement with the c lattice constant of lithium gallate reported in the literature [254]. On the left side of each scan is a peak associated with the AlGaN epitaxial layer. With increasing targeted aluminum composition, the positions of these peaks move to the right, associated with a smaller lattice spacing. Each of these AlGaN layers exhibits smaller fringes surrounding the main peak. These are known as Pendellösung fringes, and yield a quantifiable *ex situ* measure of the layer thicknesses. These thicknesses, which are all approximately 125 nm, are included in Figure 8.1.

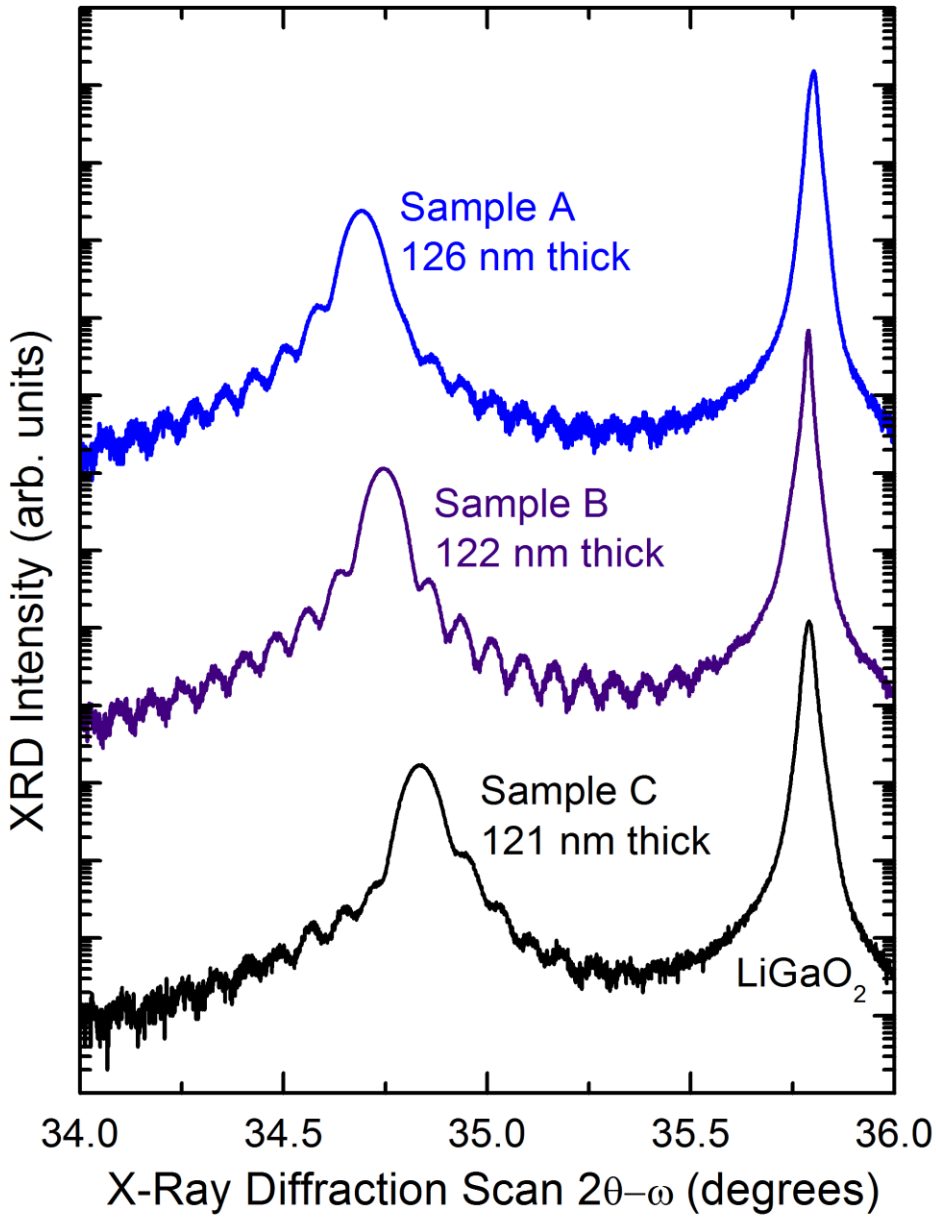

Figure 8.1: X-ray diffraction spectra of AlGaN layers grown on lithium gallate.

8.4 Calculation of In-Plane Lattice Constants

Normally for III-nitride films of similar thicknesses grown on sapphire, SiC, or GaN pseudosubstrates, Vegard's rule applies and estimation of alloy compositions are relatively straightforward. However in this case, the film is not expected to be fully relaxed, and the c-spacings extracted from the x-ray diffraction spectra are not enough information to accurately determine the aluminum composition. Reciprocal space maps must be recorded to determine the in-plane lattice constants of these layers which can then be used to determine the AlN content. Equation 9.1 can be used to accurately measure the Al composition of strained and partially strained AlGaN films [255]. This equation is solved iteratively to determine the Al composition with an accuracy of ±2%.

$$\left(\frac{c_{\exp}-[x\cdot c_{AlN}+(1-x)c_{GaN}]}{x\cdot c_{AlN}+(1-x)c_{GaN}}\right)\cdot\left(\frac{x\cdot a_{AlN}+(1-x)a_{GaN}}{a_{\exp}-[x\cdot a_{AlN}+(1-x)a_{GaN}]}\right)=-2\cdot\frac{[x\cdot C_{13}^{AlN}+(1-x)C_{13}^{GaN}]}{x\cdot C_{33}^{AlN}+(1-x)C_{33}^{GaN}} \quad (8.1)$$

The stiffness coefficients ($C_{13}^{AlN}=110, C_{33}^{AlN}=392, C_{13}^{GaN}=82, C_{33}^{GaN}=411$) were assumed to be linearly related to the composition of the film. The measured lattice spacings ($a_{\exp}$ and $c_{\exp}$) were determined from reciprocal space maps of the AlGaN layers. After inserting the theoretical lattice parameters for GaN ($a_{GaN}=3.189$ Å, $c_{GaN}=5.185$ Å) and AlN ($a_{AlN}=3.112$ Å, $c_{AlN}=4.982$ Å), the equation was solved iteratively for x, the aluminum composition of the $Al_xGa_{1-x}N$ layers.

For a six-fold symmetric hexagonal structure, the following relationships apply [121]:

$$a = \frac{\lambda}{Q_x \sqrt{3}} \sqrt{(h^2 + k^2} \tag{8.2}$$

$$c = \frac{\lambda l}{2Q_y} \tag{8.3}$$

where h, k, and l are the miller indices of the Bragg reflection, Qx and Qy are the reciprocal lattice vectors, and λ is the wavelength of the x-ray (1.54056 Å). However, the lithium gallate unit cell exhibits a quasi-hexagonal structure with slight differences in bond angles and atomic distances from a perfect hexagon. As a result, III-nitride films experience anisotropic strain to align to the lithium gallate substrate, producing two in-plane hexagonal lattice spacings and invalidating Equation 9.2. This behavior is illustrated for the case of GaN in Figure 8.2.

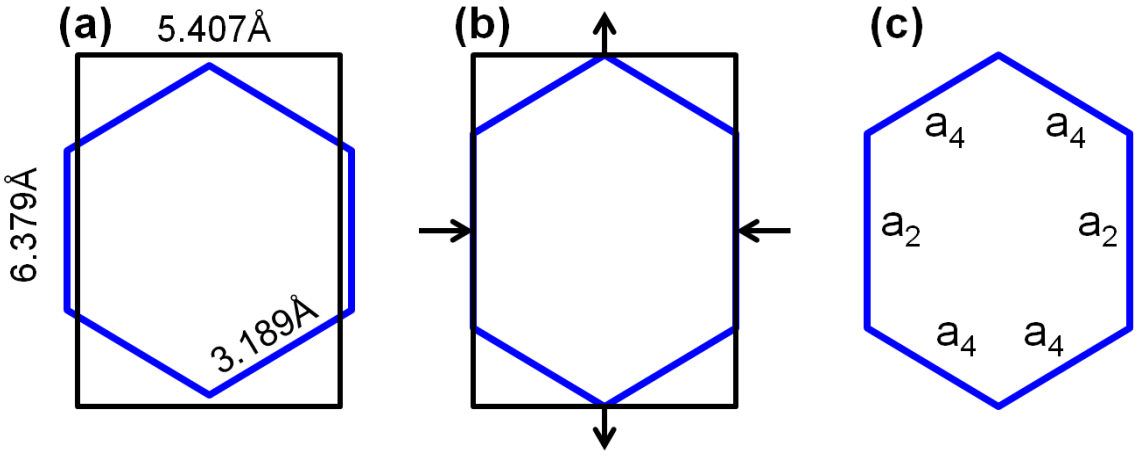

Figure 8.2: (a) Relaxed GaN hexagonal unit cell superimposed onto a lithium gallate unit cell. (b) Anisotropically strained GaN unit cell superimposed onto the lithium gallate substrate, illustrating compressive strain along the a-axis and tensile strain along the b-axis. (c) Resulting in-plane lattice spacings of the strained GaN unit cell. The illustrations are not drawn to scale.

As shown in Figure 8.2(a), the GaN unit cell is not perfectly lattice matched to $LiGaO_2$ and will experience compressive strain along the a-axis and tensile strain along the b-axis. This strain is illustrated in Figure 8.2(b). This strain results in two different in-plane lattice spacings for the III-nitride unit cell, as shown in Figure 8.2(c). Four sides of the distorted III-nitride hexagon are equal and are labeled as $a_{-4,}$ while the remaining two sides are also equal and are labeled as a_{-2}. Since there are two different in-plane hexagonal lattice spacings, there will be two different reciprocal space map peaks. Thus, a minimum of two and a maximum of three RSMs per sample must be conducted, and the sample must be rotated by approximately 60 degrees between each RSM. Furthermore, calculation of the in-plane lattice constants given the reciprocal lattice vectors from the RSMs becomes more complex.

An in-plane vector beginning at the center of the distorted hexagonal structure and ending at a right angle with the side of the hexagon can be determined with the following equation [256]:

$$v = \frac{\lambda}{2Q_x}. \tag{8.4}$$

Considering the two-fold symmetry in the distorted III-nitride unit cell as shown in Figure 8.2, there will be two in-plane vectors that are equal and labeled as v_{-2}, and four in-plane vectors that are equal and labeled as v_{-4}. Given these measured values from the reciprocal space maps, the in-plane lattice spacings can be calculated. These in-plane vectors are shown on the III-nitride unit cell in Figure 8.3. It is assumed that these vectors intersect the sides of the distorted hexagon at 90° angles. The error from this assumption has been calculated in the literature as less than 0.15% [256].

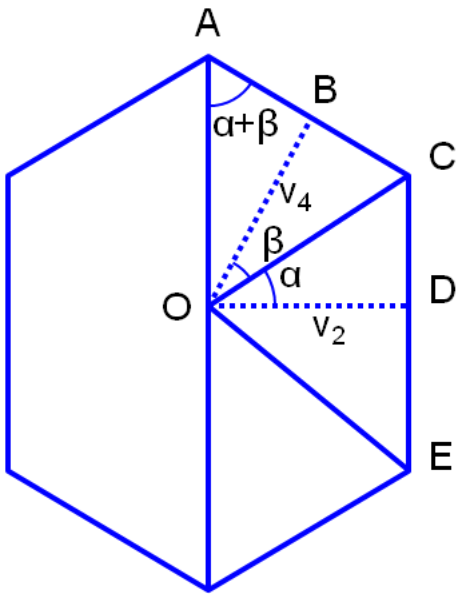

Figure 8.3: Illustration of the in-plane vectors of a distorted hexagonal unit cell calculated from the reciprocal lattice vectors. Capital letters indicate intersections, and Greek letters indicate angles.

Considering the two-fold symmetry of this distorted hexagonal unit cell shown in Figure 8.3, it is clear that $AO = CE = 2CD$.

As a result, $\cos(90-(\alpha+\beta)) = \frac{v_4}{AO} = \frac{v_4}{2CD}$. (8.5)

Since $\tan(\alpha) = \frac{CD}{v_2}$, (8.6)

Then combining Equations 8.5 and 8.6, $\cos(90-(\alpha+\beta)) = \frac{v_4}{2v_2\tan(\alpha)}$. (8.7)

Triangles OBC and ODC share a hypotenuse, so $\cos(\alpha) = \frac{v_2}{CO}$ (8.8)

and $\cos(\beta) = \frac{v_4}{CO}$. (8.9)

Thus, by combining Equations 8.8 and 8.9, we can state $\frac{\cos(\alpha)}{\cos(\beta)} = \frac{v_2}{v_4}$. (8.10)

We can then substitute Equation 8.10 into Equation 8.7 to obtain one equation with only α and β: $\cos(90-(\alpha+\beta)) = \frac{\cos(\beta)}{2\cos(\alpha)\tan(\alpha)}$. (8.11)

Equation 8.11 can then be solved iteratively for α and β. Finally, we can solve for a2 and a4, the sides of the distorted unit cell by $a_2 = CE = 2CD = 2v_2\tan(\alpha)$ (8.12)

and $a_4 = \frac{v_2}{\sin(\alpha+\beta)}$. (8.13)

The two in-plane lattice spacings calculated for each sample are then averaged, producing a single lattice spacing. This average in-plane lattice spacing can then be used with Equation 9.1 to determine the aluminum composition. The aluminum compositions for Samples A, B, and C were determined to be 9.2%, 14.1%, and 21.1%, respectively. These aluminum compositions are in good agreement with that targeted for each sample. Rocking curve full-width at half-maxima (FWHM) for Samples A, B, and C were determined to be 139, 116, and 146 arcseconds, respectively. These results are summarized in Table 8.2. It is important to note that Sample B has the highest crystalline quality and has an aluminum content (14.1%) closest to the predicted lattice match at growth temperature (12.5%).

Table 8.2: Summary of measured structural results from AlGaN layers grown on $LiGaO_2$.

	Al/Ga Flux Ratio	Measured Al composition (%)	Sample thickness (nm)	(0002) RC FWHM (arcseconds)
Sample A	10%	9.1%	126	139
Sample B	15%	14.1%	122	116
Sample C	20%	21.1%	121	146

8.5 Conclusions

AlGaN layers have been grown on lithium gallate substrates. Aluminum compositions were chosen in an attempt to lattice match the AlGaN layers at growth temperature. Aluminum contents were calculated from multiple reciprocal space maps conducted for each sample. It was found that the sample with an aluminum content of 14.1% had the highest structural quality as detected by x-ray diffraction rocking curves. This aluminum content is closest of all three samples grown to 12.5%, which has been previously calculated as being lattice matched to $LiGaO_2$ at growth temperature. The experiments described in this chapter establish that not only is $LiGaO_2$ a feasible substrate for the growth of lattice-matched AlGaN layers, but MME is a viable growth technique for these layers as well.

CHAPTER 9: CONCLUSIONS AND FUTURE DIRECTIONS

9.1 Conclusions

The research presented in this thesis focuses on the growth kinetics of III-nitride materials by molecular-beam epitaxy. The group-III nitride materials system has an exciting set of properties that are capable of hosting a wide range of electronic and optoelectronic devices. Although some of these devices have been developed, many more applications of these materials have yet to be realized. This lack of progress has been attributed to insufficient structural and electrical material quality, which is directly associated with the growth of the material. The goal of this work is to evaluate and solve several of the major issues with the growth of III-nitride binaries and ternaries, and enable the development of novel or currently unfeasible device structures. The primary results of this work include:

1. A novel technique for *in situ* growth characterization by analyzing time-dependent RHEED intensities has been developed. It was found that the intensity of a RHEED streak recorded during the growth of a sample is greatly dependent on the presence and quantity of an adsorbed, amorphous metal layer that accumulates during metal-rich growth. This layer could be controlled through periodic opening and closing of the metal shutters to produce the desired growth conditions *in situ*.

2. A comprehensive study of the growth kinetics of GaN has been performed. Excess metal layers resulting from metal-rich growth were analyzed to determine how the GaN growth surface behaves. This study confirmed the thickness of the stable laterally contracted Ga bilayer which was previously only theoretically calculated in literature.

3. A novel method of *in situ* growth rate determination was demonstrated. Adlayer consumption into the film during the metal-modulated epitaxy process was quantifiably measured. By eliminating species desorption from the sample surface and incoming reactants to the growth, this consumption was translated directly into growth rate and found to be accurate within margins of error.

4. The highest reported hole concentration in GaN is presented. By monitoring and manipulating the behavior of adsorbed layers on the GaN growth surface, Mg dopant atoms could be encouraged to preferentially occupy a Ga-substitutional site. This technique resulted in a Mg activation efficiency five times higher than the previous best reported in the literature, and a hole concentration of nearly 8×10^{19} cm^{-3}. This value is an order of magnitude higher than previously perceived limits reported in the literature.

5. A method of observing and controlling indium surface segregation during the metal-rich growth of InGaN alloys is discovered. Evidence of indium surface segregation occurring *in situ* is detected in transient RHEED intensities.

6. The behavior and onset of the indium surface segregation phenomenon is elucidated. It was found that indium surface segregation is most accurately associated with the quantity of excess indium and gallium on the growth surface, as opposed to metal-rich growth in general. This conclusion differs from results of less rigorous studies in the literature, and enables the growth of high-quality InGaN materials.

7. A means to quantify the onset of indium surface segregation during the growth of InGaN is discovered. This method is not growth-system dependent, allowing this quantification to be conducted on a variety of molecular-beam epitaxy systems. It was found that the growth conditions nearest to the onset of indium surface segregation resulted in the highest crystalline quality and smoothest surfaces. Thus, the ability to accurately calculate the onset of indium surface segregation is essential for the growth of high quality InGaN alloys.

8. The growth of InGaN alloys of arbitrary indium composition with no evidence of phase separation is demonstrated. This alloy has previously been grown with relatively small (<20%) indium compositions, but the growth of single-phase material with high indium contents has proven to be elusive. This study shows that by controlling indium surface segregation and growing at relatively low temperature, all means of phase separation can be prevented. Although grown at low substrate temperatures, these layers exhibited extremely high crystalline qualities necessary for device implementation.

9. Growth of InN by Metal-Modulated Epitaxy is reported. The transient RHEED intensities recorded during the growth of this binary were found to be very similar to those previously recorded for GaN and AlN. Structural and electrical qualities of these layers were found to be consistent with state-of-the-art layers reported in the literature.

10. The first reported instance of AlGaN grown by Metal-Modulated Epitaxy is reported. Transient RHEED intensities recorded during the growth of this alloy were similar to that previously reported for GaN and AlN, and exhibited no evidence of surface segregation.

11. Mg-doped AlGaN layers were grown by Metal-Modulated Epitaxy with an extremely high hole concentration. Hole activation energies increase with aluminum contents in AlGaN, a hole concentration of nearly 6×10^{18} cm^{-3} was detected by electrical characterization.

12. AlGaN layers were grown by Metal-Modulated Epitaxy on a nearly lattice-matched substrate. It has been previously predicted that AlGaN with an aluminum content of ~12.5% would be lattice matched to a lithium gallate substrate. It was found experimentally that the highest crystalline quality AlGaN layers had an aluminum very close to this theoretically calculated value.

9.2 Future Directions

This work has solved many of the major hurdles preventing the realization of several currently unavailable devices, such as III-nitride solar cells and high-efficiency LEDs within the green gap. However, several challenges associated with the growth and fabrication of device structures still remain. Future work in this area may include:

1. Reduction of defect densities in InGaN layers. Although single-phase high-indium content InGaN layers were grown, solar cells fabricated using these materials exhibited large leakage currents. To increase the turn-on voltage of solar cells and subsequently increase external efficiency, these defects must be reduced. Suggested angles of attack include *ex situ* defect passivation, growth on lattice matched substrates, and more precisely calibrated growth conditions.

2. Growth of III-nitride layers on silicon. Growth on sapphire involves costly substrate purchasing, nucleation, and buffer conditions. Commercialization of group-III nitride-based devices would benefit from a cheaper substrate, such as silicon. Although bulk growth of silicon produces some of the highest quality substrates available to crystal growers, this substrate is still difficult to use due to amorphous Si_xN_y layer formation and large lattice mismatches. Further exploration of III-nitride nucleation on silicon and the application of the III-nitride growth techniques outlined in this thesis would be very beneficial.

3. Growth and fabrication of a III-nitride tunnel junction. Tunnel junctions are essential for the production of multi-junction solar cells, enabling electrical conductivity through multiple p-n junctions. Some groups have created III-nitride tunnel junctions with the assistance of polarization fields, but none have been produced through more conventional means. The extremely high hole concentration, deeply degenerate p-GaN material discussed in this thesis provides a template for a III-nitride tunnel junction.

APPENDIX A: CHEMICAL MECHANICAL POLISHING OF LITHIUM GALLATE SUBSTRATES

A.1 Abrasive Material Removal: Sanding, Lapping, and Polishing

Abrasive removal of material is a very popular method of surface preparation in the semiconductor industry. Often, materials either need to be reduced in thickness or a surface needs to be smoothed, allowing the next step of the process to continue. Examples of this include polishing after wafer dicing from a boule and the Damascene process. Abrasive material removal can be as crude as the use of sandpaper, and can also describe very carefully controlled processes producing a mirror-like finish. The two dominant techniques of abrasive material removal in the semiconductor industry are lapping and polishing. Although extremely similar in principle, these two techniques represent different processes and are discussed herein.

In both lapping and polishing, a sample is generally attached to a flat, free-moving mount. This mount, sometimes called a "chuck" is placed face-down onto an abrasive surface. This surface can be a glass plate or a polishing pad, and has small particles of abrasive material scattered upon it. The surface is then moved relative to the mount, or the mount is moved relative to the surface, and the abrasive scrapes or rubs against the sample surface. In this way, the abrasive surface literally scratches and fractures small chunks of material away from the sample surface. An illustration of these basic principles of abrasive material removal is shown in Figure A.1.

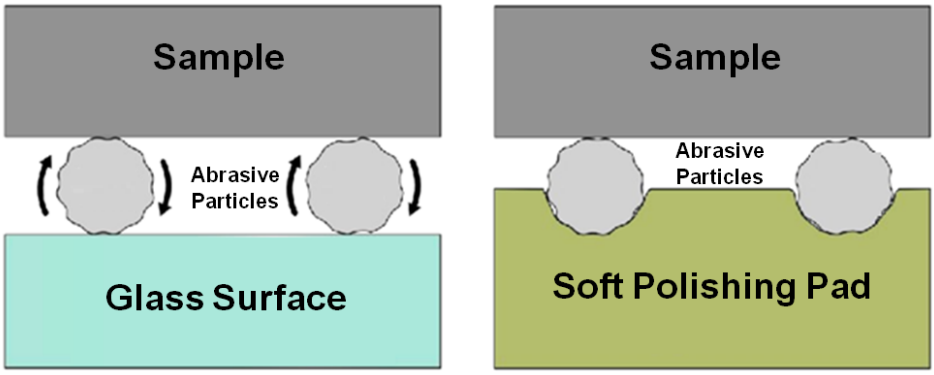

Figure A.1: Illustration of lapping (left side) and polishing (right side) [257]. Both processes involve the use of abrasive particles that scratch a sample. Polishing generally uses much smaller particles than lapping, and produces mirror-like finishes.

It is worth noting that polishing and lapping are two similar processes whose names are sometimes used interchangeably. However, lapping is a term generally employed for the removal of material or roughening of a surface rather than polishing. Prior to polishing, samples are usually lapped to establish a starting point for the rest of the polish. Instead of a soft pad, lapping uses a glass plate, and usually a larger abrasive particle (3 μm and above). This plate forces the medium closer to the sample than a pad would, effectively gouging more material out. The flat, glass surface ensures an even removal of material across the entire sample surface. The fact that the glass surface is hard helps the abrasive particles remove material quicker, as well. Polishing, on the other hand, uses smaller particles (1μ and below) and employs a polishing pad. The pad allows the abrasive particles to sit down into small crevices and holes, exposing the sample to a less rough surface. A wide variety of pads can be purchased with different densities and sizes of these crevices and holes, called the "nap". A variety of polishing pads are available, each with different properties that can chosen to suit a specific polishing application.

The abrasive material is usually some type of powder composed of hard, microscopic material that is mixed with a liquid forming a "slurry". By far the most popular abrasive material is aluminum oxide (Al_2O_3), however diamond, SiC, and SiO_2 are also available for different applications. Obviously, the harder the material that needs to be lapped or polished, the harder the abrasive needs to be. In a situation where the sample has a hardness of greater than or equal to alumina, diamond is suggested. The abrasive material is mixed with a liquid (usually water) and sometimes mixed with a lubricating agent (usually ethylene glycol) and dripped onto the glass surface or polishing pad. The consistency of this slurry is important. If the slurry is very thick, a large amount of abrasive material will be supplied to the polishing or lapping process, increasing the polish or lap rate. On the other hand, a thick slurry may not be lubricated enough and can accumulate on the sample surface, producing a non-uniform polish. Conversely, too thin of a slurry results in a very slow polish or lap rate. Generally, the slurry includes white abrasives, and the consistency should resemble that of milk for a reasonable balance. As the polishing process takes place, pieces of material removed from the sample surface are washed away, and new abrasive particles are supplied.

Material can also be removed through a combination of chemical and mechanical techniques. Different liquids such as an etchant may be added to the slurry to support the abrasive process. Although capable of a quicker and sometimes finer polish, this type of polishing is quite specific the material that needs to be polished.

A.2 Lapmaster Polisher

The brand of polishing and lapping equipment used for all processes detailed in this appendix was Lapmaster. The Lapmaster Polisher and Lapper are identical pieces of equipment except for the abrasive surface. The abrasive surface for both cases is a horizontal, flat, circular surface that is spun continuously by an electric motor. In the case of the Lapmaster Lapper, the surface is glass, whereas it is a metal plate in the case of the Polisher. The user is expected to adhere a polishing pad onto the metal plate for polishing. In the middle and around the outsides of the abrasive surface are drains to collect particles of material removed from the sample surface. Before use, the entire abrasive surface must be wiped down carefully with isopropanol and a new polishing pad must be used in the case of polishing to ensure no abrasive material cross-contamination. In the case of lapping, the entire glass surface must also be profusely rinsed and dried to remove all previous abrasive particles, preventing cross-contamination between lapping steps.

The samples are adhered into a plastic plate with recesses fit to the size of each sample. This plate should be made of a very soft material to ensure that small chunks removed from the plate will not scratch the material to be polished. Teflon makes a great material for this plate because it is easily milled to the appropriate size and thickness, it is very soft, and it won't react in a chemical-mechanical polishing process. The recesses in this plate ensure that samples do not move or become detached during the lapping or polishing process. However, removal of these samples from the recesses can be difficult if they are adhered with double-sided tape. The recommended adhesion material is wax,

which can be melted on a hot-plate or dissolved with trichloroethylene for easy removal of the samples from the plate. The use of wax prevents the user from having to place physical stress on the sample with tweezers to remove it from the recess. An illustration of this plate is shown in Figure A.2. The sample plate is then adhered by double-sided tape onto the heavy, metal sample mount called an Accupole in the case of the Lapmaster brand of lappers and polishers. This Accupole sample mount process is shown in Figure A.3 and a cross-sectional view of the completed setup is shown in Figure A.4.

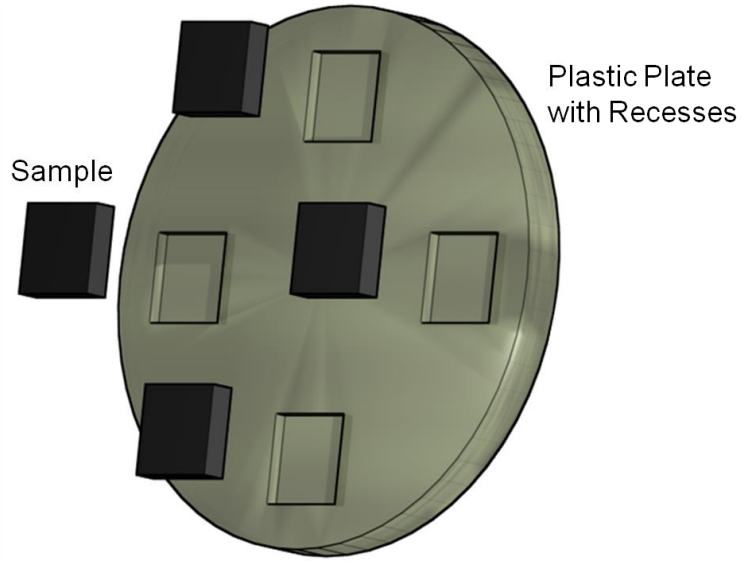

Figure A.2: Plastic sample mount with recesses for small, square samples [257]. The samples are adhered into the recesses with wax, which is melted using a hot-plate.

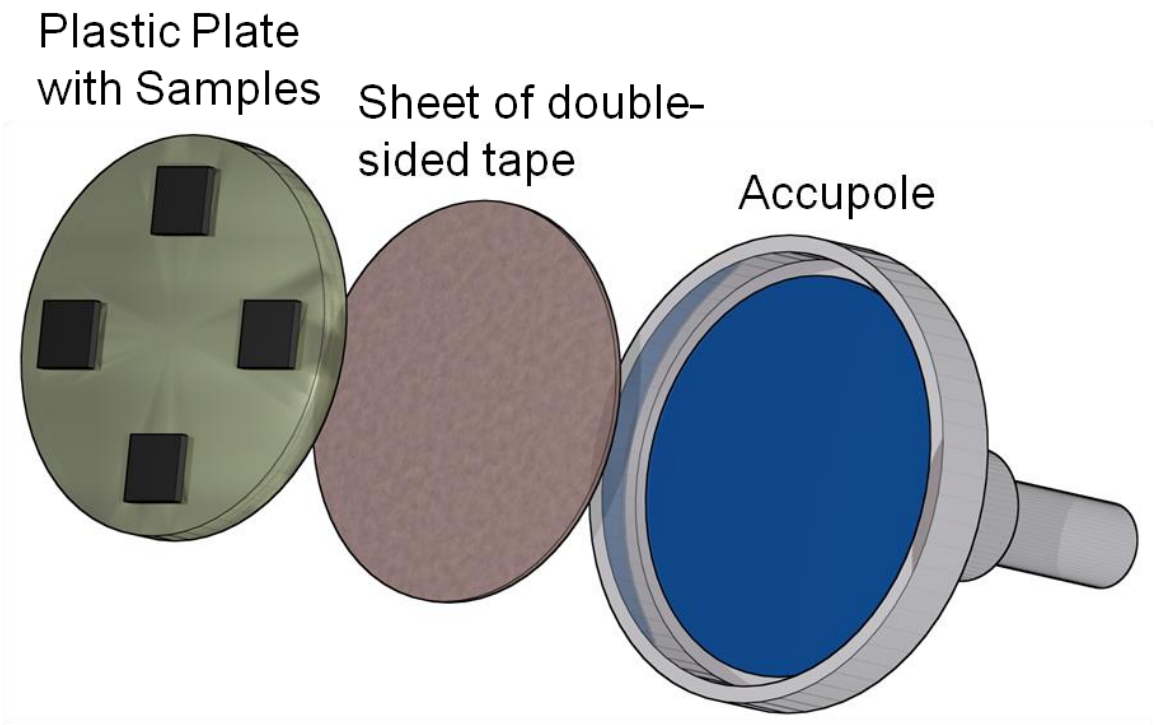

Figure A.3: Accupole sample-mount process [257]. After placing the samples into the plastic plate recesses, this plate is secured to the Accupole with double-sided tape.

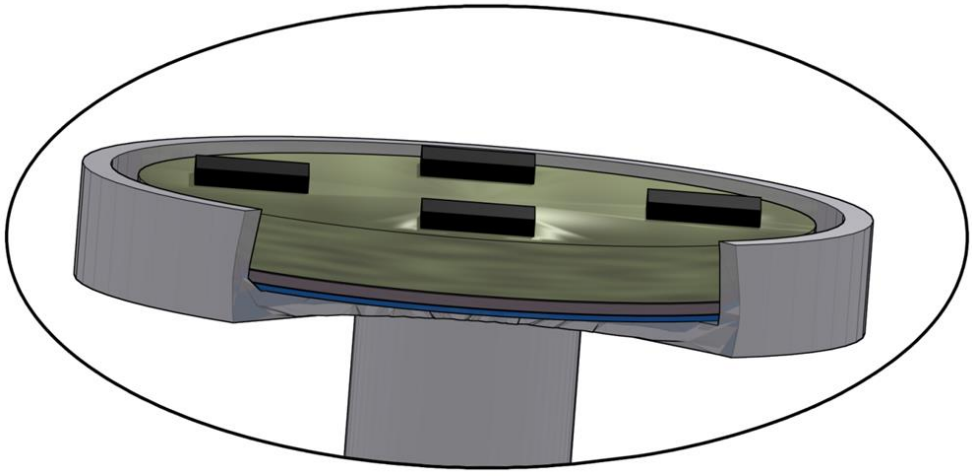

Figure A.4: Cross-sectional view of the Accupole with the samples, recessed plastic plate, and double-sided tape [257].

Once the samples are mounted onto the Accupole, this mount is set aside and the adhesive slurry is prepared. The user must mix his or her own slurry made from water, ethylene glycol (optional), and the chosen abrasive material. This slurry is kept in an open container, and a plastic tube runs from the container to the polishing pad surface. The slurry may need to be stirred to maintain a mixture. Although this stirring can be done manually with a simple glass rod, it is suggested to use a magnetic stirrer with a Teflon-coated magnet in the container. A peristaltic pump is used to flow material through the tube without contaminating the slurry. A separate slurry tube should be used for each size of abrasive material to prevent cross-contamination between polishing/lapping steps. The desired flow rate can vary depending on the application, yet a reasonable safe rate to employ is one drop per second. The abrasive surface is then spun at a speed of approximately 0.2 revolutions per second while the slurry is flowing.

The Accupole may be adjusted by twisting the rod that extends out of the top such that the plastic sample plate is recessed, and only the outer ring of the Accupole may touch the abrasive surface when placed sample-side down. This is done to ensure uniform coverage of the abrasive slurry onto the abrasive surface without allowing the samples to come into contact with the abrasive. The Accupole is then placed sample-side down onto the abrasive surface, and is held laterally in the same location by arms that extend from a post secured outside of the abrasive surface. On these arms are two rollers, which allow the Accupole to rotate with the abrasive surface. Once the abrasive surface is uniformly wet with the slurry, the Accupole can again be adjusted to allow the samples to come into contact with the abrasive surface. At this point, the polishing or lapping process is taking place. An illustration of this setup is shown in Figure A.5.

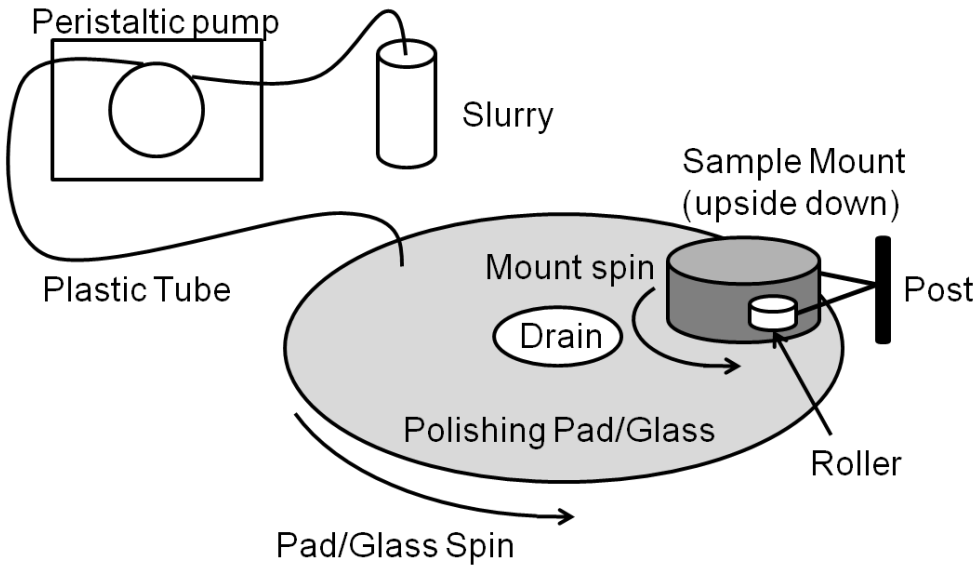

Figure A.5: Polishing and lapping setup, showing the sample mount (sample-side down), abrasive surface, slurry container, and peristaltic pump for non-contaminating slurry movement. The abrasive surface spins as labeled, and the sample mount is free to spin in the same direction.

The sample setup discussed in Figure A.5 has several techniques to customize the quality and rate of the lap or polish. The sample-mount itself can be weighted to apply more force between the sample and the abrasive surface. More pressure will generally include a faster and rougher polish. In the case of a very rough polish where only a mirror finish is desired, or in a rough lap where only a coarse finish is required, this weight can be increased easily. However, for very fine processes where the surface morphology must be precisely controlled, the sample mount should not be weighted. Similarly, the rotation speed of the abrasive surface can be increased or decreased by a knob on the Lapmaster equipment. A faster rotation increases material removal rate, but can result in a non-uniform sample morphology.

A.3 Lithium Gallate As-Received Wafers

Lithium gallate substrates pose a challenge for growers wishing to obtain an atomically flat, epitaxy-ready surface. This material is etched very slowly by water, necessitating storage in a very dry environment. Lithium gallate is also very brittle, and relatively soft, requiring very careful handling and producing very fast lapping rates. Substrates received from the vendor had a surface morphology as shown in Figure A.6, and had an average roughness of approximately 0.43 nm RMS.

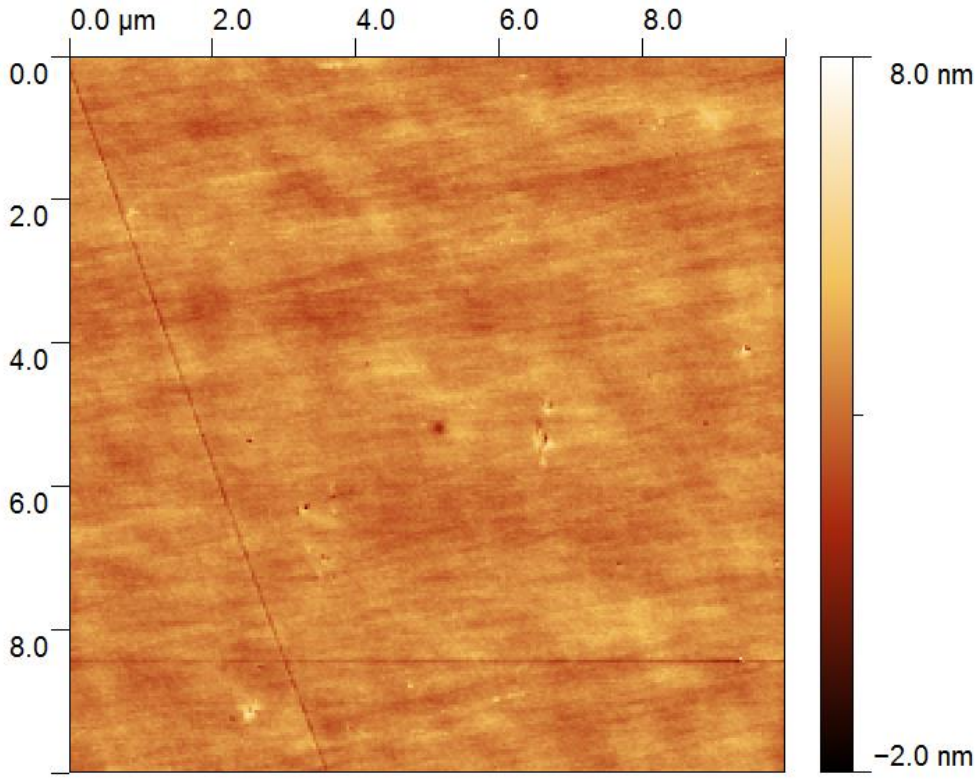

Figure A.6: Surface morphology of an as-received lithium gallate wafer over a 10 × 10 µm area. The Z-scale is 10 nm, and the RMS roughness was calculated to be 0.43 nm.

Although relatively smooth, these films exhibited sub-surface damage. After a solvent clean in trichloroethylene, acetone, and methanol, the as received samples had a rough morphology. As shown by the AFM scan in Figure A.7, scratches and pits are visible. This solvent-cleaned sample had an average surface roughness of 2.62 nm rms.

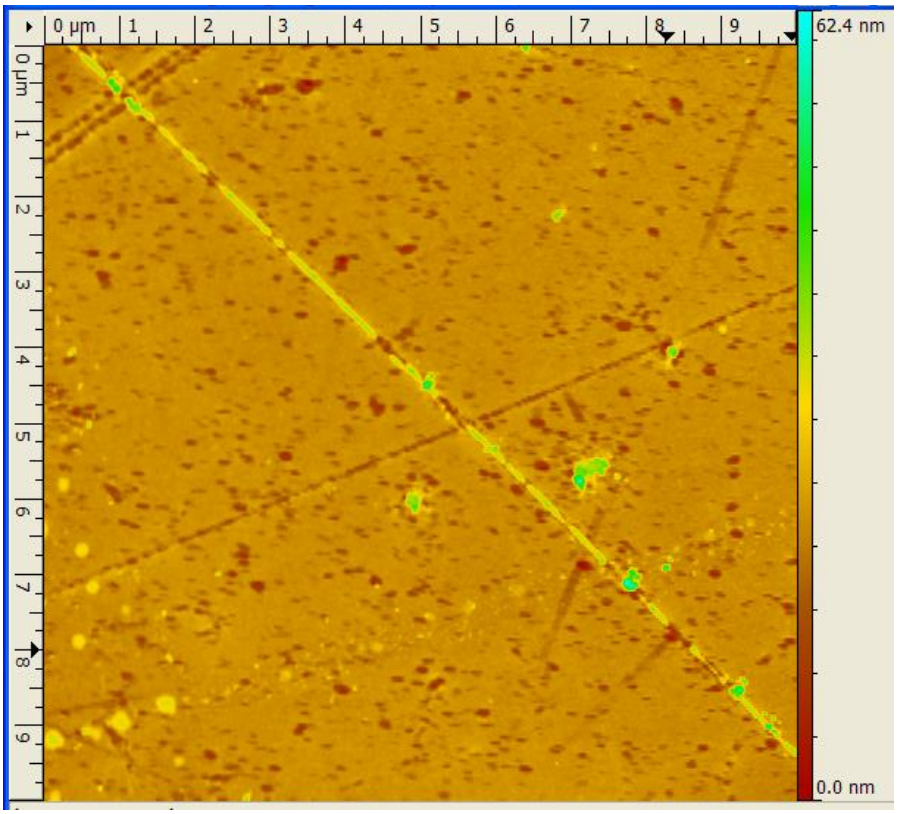

Figure A.7: Surface morphology of a solvent-cleaned, as-received lithium gallate wafer over a 10 × 10 µm area. The Z-scale is 62.4 nm, and the RMS roughness was calculated to be 2.62 nm. Scratches and pits are revealed after solvent cleaning in trichloroethylene, acetone, and methanol.

Substrates exhibiting the kind of sub-surface damage shown in Figure A.7 have been shown to result in rough morphologies in subsequently grown III-nitride films. An example of a rough GaN film grown on top of a rough, poorly-prepared lithium gallate substrate is described by the AFM morphology in Figure A.8. The GaN surface shown in Figure A.8 had an RMS roughness of 8.2 nm [167].

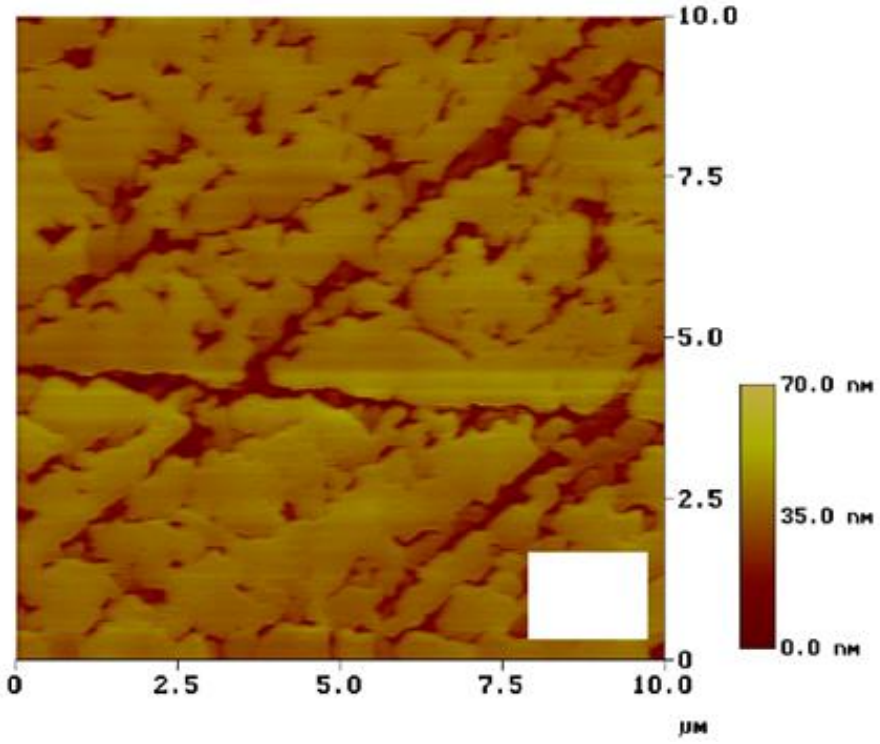

Figure A.8: Surface morphology of a GaN thin film grown by molecular-beam epitaxy over a 10 × 10 μm area on a poorly-prepared lithium gallate substrate. The Z-scale is 70 nm, and the RMS roughness of the GaN film was calculated to be 8.2 nm [167]. The lines visible in the AFM image are translated from scratches on the lithium gallate substrate.

A.4 Lithium Gallate Polishing Process

To remove subsurface damage, decrease surface roughness, and improve epitaxially grown crystalline layers, a custom polishing process was developed for lithium gallate. Considering the already relatively smooth surface of these as-received lithium gallate wafers, a lapping procedure was not necessary. Instead, a three step polishing process is used, beginning with a mechanical abrasive polish and concluding with a chemical-mechanical process. The pads used for all polishing steps described in this section were Politex (PF-PRL), purchased from Eminess Technologies, Inc.

Before polishing, the epitaxial surface of the as-received lithium gallate samples was gently beveled around the edges with 600-grit sandpaper. This bevel prevents large chunks from the edge of the sample from breaking off during the polish and scraping across the smooth surface of the sample. Following this exposure to relatively dirty and high particle count sandpaper, the samples were solvent cleaned with TCE, acetone, and methanol. Five lithium gallate samples were then adhered into the recesses of the plastic plate and mounted onto the Accupole as described in A.2. The metallic outer ring of the Accupole sample mount that touches the abrasive surface was replaced with a Teflon ring. Abrasively removed material from this Teflon ring will not scratch the soft lithium gallate surface, whereas metallic chunks would.

The first step of the polishing process employed 1 μm alumina abrasive. A 500 mL Nalgene bottle was used to store the prepared slurry. This bottle was initially filled with 375 mL of DI water. Next, the alumina powder was added to produce a consistency and color resembling milk. Finally, the remainder of the bottle was filled with ethylene

glycol to lubricate the polishing process. A small Teflon-coated iron rod was dropped into this prepared slurry bottle, and a magnetic stirrer was used to maintain a consistent mixture. Tygon tubing was used to deliver the prepared slurry to the polishing pad. A different slurry bottle, Teflon Accupole ring, Teflon-coated iron rod, polishing pad, and slurry delivery tube was used for each size abrasive powder to prevent cross-contamination.

The slurry flow rate onto the polishing pad was approximately one drop per second, and the rotation speed of the polishing pad was approximately 0.2 revolutions per second. The Accupole was placed onto the polishing pad with the samples disengaged from the surface to sufficiently wet the abrasive surface. After the surface was uniformly coated with the polishing slurry, the Accupole was adjusted to engage the samples with the abrasive surface and polishing slurry. The samples were then allowed to polish for 15 minutes.

After the samples have polished for the specified time, the Accupole was removed from the polishing pad. The sample plate and samples were then fully solvent cleaned in TCE, acetone, and methanol to remove the wax and 1 μm slurry particles, and the entire workspace was thoroughly wiped down with isopropanol. The polishing pad for this step was discarded. The Teflon Accupole ring, Teflon-coated iron rod, slurry bottle, and slurry delivery tube were all stored in plastic bags to be used for later 1 μm slurry polishing processes.

A clean Teflon Accupole ring, Teflon-coated iron rod, slurry bottle, slurry delivery tube, and polishing pad were installed. The clean, 1 μm polished samples were adhered into the sample plate, which was mounted onto the Accupole. The second step

of this polishing process was identical to the first step, but employed 0.3 μm slurry. This reduction in slurry particle size produces a much finer smoothness, but does not achieve an epitaxy-ready surface. The cleanup for this second step was also similar to the first step. The sample plate and samples were fully solvent cleaned in TCE, acetone, and methanol to remove the wax and 0.3 μm slurry particles, and the entire workspace was thoroughly wiped down with isopropanol. The polishing pad for this step was discarded. The Teflon Accupole ring, Teflon-coated iron rod, slurry bottle, and slurry delivery tube were all stored in plastic bags to be used for later 0.3 μm slurry polishing processes.

The third and final step of the polishing process utilizes water as a mild etchant of lithium gallate [258, 259] instead of an abrasive technique. A clean Teflon Accupole ring, Teflon-coated iron rod, slurry bottle, slurry delivery tube, and polishing pad were installed. The clean, 0.3 μm polished samples were adhered into the sample plate, which was mounted onto the Accupole. A 1:1 mixture of water and ethylene glycol was prepared in a 500 mL Nalgene bottle. The samples were allowed to polish for 30 minutes. All other parameters of this third polishing step are identical to the first two steps. The cleanup for this third step was also similar to the first two steps. The sample plate and samples were fully solvent cleaned in TCE, acetone, and methanol to remove the wax and ethylene glycol. The polishing pad for this step was discarded. The Teflon Accupole ring, Teflon-coated iron rod, slurry bottle, and slurry delivery tube were all stored in plastic bags to be used for later chemical-mechanical polishing processes.

The use of water, a mild $LiGaO_2$ etchant, as a chemical polishing agent in concert with the very fine Politex pads produces an extremely flat surface morphology. After a full solvent clean to remove any surface particles and expose sub-surface damage, the

samples were examined using an atomic force microscope (AFM). Shown in Figure A.9 is the surface morphology of a solvent-cleaned lithium gallate sample that was polished using the process outlined in this chapter. The Z-scale of the morphology shown in Figure A.9 is 10 nm. The RMS roughness was calculated to be 0.11 nm.

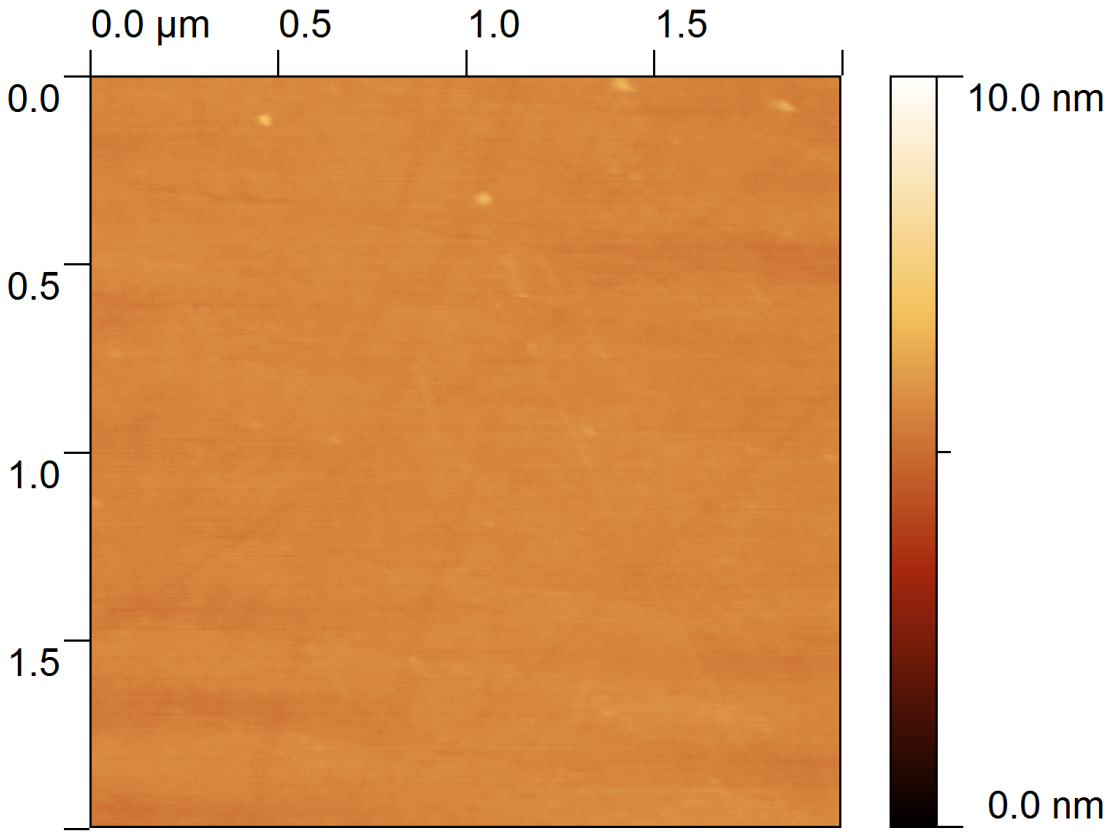

Figure A.9: Surface morphology of custom-polished lithium gallate wafer over a 2 × 2 µm area. The Z-scale is 10 nm, and the RMS roughness was calculated to be 0.11 nm.

REFERENCES

[1] G. B. Stringfellow, "Epitaxy", *Rep. Prog. Phys.* **45**, 469 (1982).

[2] J. E. Davey and T. Pankey, "Epitaxial GaAs Films Deposited by Vacuum Evaporation", *J. Appl. Phys.* **39**, 1941 (1968).

[3] A. Y. Cho, M. B. Panish and I. Hayashi, "Molecular Beam Epitaxy of GaAs, $Al_xGa_{1-x}As$, and GaP", *3rd Int. Symp on Gallium Arsenide and Related Compounds* **9**, 18 (1970).

[4] J. R. Arthur, "Molecular beam epitaxy", *Surf. Sci.* **50**, 189 (2002).

[5] G. Koblmüller, R. Averbeck, H. Riechert and P. Pongratz, "Direct observation of different equilibrium Ga adlayer coverages and their desorption kinetics on GaN (0001) and (000$\bar{1}$1) surfaces", *Phys. Rev. B* **69**, 035325 (2004).

[6] J. S. Brown, G. Koblmuller, F. Wu, R. Averbeck, H. Riechert and J. S. Speck, "Ga adsorbate on (0001) GaN: In situ characterization with quadrupole mass spectrometry and reflection high-energy electron diffraction", *J. Appl. Phys.* **99**, 074902 (2006).

[7] H. Okumura, K. Balakrishnan, H. Hamaguchi, T. Koizumi, S. Chichibu, H. Nakanishi, T. Nakatomo and S. Yoshida, "Analysis of MBE growth mode for GaN epilayers by RHEED", *J. Cryst. Growth* **189/190**, 364 (1998).

[8] J. Suda, T. Kurobe, T. Masuda and H. Matsunami, "Preferential Growth Mode of Cubic GaN by Metalorganic Molecular Beam Epitaxy on Sapphire (0001) Substrates", *Phys. Status Solidi A* **176**, 503 (1999).

[9] J. L. Deiss, C. Hirlimann, J. L. Loison, M. Robino and G. Versini, "Epitaxial growth of GaN thin films on sapphire (0001) by pulsed laser deposition: influence of surface preparation and nitridation", *Mater. Sci. Eng., B* **B82**, 68 (2001).

[10] S. Marlafeka, N. Bock, T. S. Cheng, S. V. Novikov, A. J. Winser, I. Harrison, C. T. Foxon and P. D. Brown, "A structural study of phase transitions within GaN layers grown by low-temperature molecular beam epitaxy", *J. Cryst. Growth* **230**, 415 (2001).

[11] Y. Liu, M. H. Xie, Y. G. Cao, H. S. Wu and S. Y. Tong, "A study of $In_xGa_{1-x}N$ growth by reflection high-energy electron diffraction", *J. Appl. Phys.* **97**, 023502 (2005).

[12] B. Heying, R. Averbeck, L. F. Chen, E. Haus, H. Riechert and J. S. Speck, "Control of GaN surface morphologies using plasma-assisted molecular beam epitaxy", *J. Appl. Phys.* **88**, 1855 (2000).

[13] G. Koblmüller, J. Brown, R. Averbeck, H. Riechert, P. Pongratz and J. S. Speck, "Ga Adlayer Governed Surface Defect Evolution of (0001)GaN Films Grown by Plasma-Assisted Molecular Beam Epitaxy", *Jpn. J. Appl. Phys., Part 2* **44**, 906 (2005).

[14] C. D. Lee, Y. Dong, R. M. Feenstra, J. E. Northrup and J. Neugebauer, "Growth and Surface Reconstructions of AlN(0001) Films", *Mater. Res. Soc. Symp. Proc.* **798**, 317 (2004).

[15] R. M. Feenstra, H. Chen, V. Ramachandran, A. R. Smith and D. W. Greve, "Reconstructions of GaN and InGaN surfaces", *Appl. Surf. Sci.* **166**, 165 (2000).

[16] C. E. C. Wood, "RED Intensity Oscillations During MBE of GaAs", *Surf. Sci.* **108**, L441 (1981).

[17] W. Braun, *Applied RHEED: Reflection High-Energy Electron Diffraction During Crystal Growth*. Springer tracts in modern physics. 1999, Berlin, Germany: Springer.

[18] J. M. Cowley, *Electron Diffraction Techniques*. 1993, Chester, England: International Union of Crystallography.

[19] C. Adelmann, R. Langer, G. Feuillet and B. Daudin, "Indium incorporation during the growth of InGaN by molecular-beam epitaxy studied by reflection high-energy electron diffraction intensity oscillations", *Appl. Phys. Lett.* **75**, 3518 (1999).

[20] C. Adelmann, J. Brault, E. Martinez-Guerrero, G. Mula, H. Mariette, L. S. Dang and B. Daudin, "Molecular-Beam Epitaxy of GaN: A Phase Diagram", *Phys. Status Solidi A* **188**, 575 (2001).

[21] C. Adelmann, J. Brault, G. Mula and B. Daudin, "Gallium adsorption on (0001) GaN surfaces", *Phys. Rev. B* **67**, 165419 (2003).

[22] C. Adelmann, J. Brault, D. Jalabert, P. Gentile, H. Mariette, G. Mula and B. Daudin, "Dynamically stable gallium surface coverages during plasma-assisted molecular-beam epitaxy of (0001) GaN", *J. Appl. Phys.* **91**, 9638 (2002).

[23] S. D. Burnham and W. A. Doolittle, "*In situ* growth regime characterization of AlN using reflection high energy electron diffraction", *J. Vac. Sci. Technol. B* **24**, 2100 (2006).

[24] S. D. Burnham, G. Namkoong, K.-K. Lee and W. A. Doolittle, "Reproducible reflection high energy electron diffraction signatures for improvement of AlN

using *in situ* growth regime characterization", *J. Vac. Sci. Technol. B* **25**, 1009 (2007).

[25] T. Yamaguchi, D. Muto, T. Araki, N. Maeda and Y. Nanishi, "Novel InN growth method under In-rich condition on GaN/Al_2O_3 (0001) templates", *Phys. Status Solidi C* **6**, S360 (2009).

[26] T. Yamaguchi and Y. Nanishi, "Indium Droplet Elimination by Radical Beam Irradiation for Reproducible and High-Quality Growth of InN by RF Molecular Beam Epitaxy", *Appl. Phys. Express* **2**, 051001 (2009).

[27] K. Wang, T. Yamaguchi, T. Araki, E. Yoon and Y. Nanishi, "In situ Investigation of Growth Mechanism during Molecular Beam Epitaxy of In-Polar InN", *Jpn. J. Appl. Phys.* **50**, (2011).

[28] S. D. Burnham, W. Henderson and W. A. Doolittle, "Closed-loop MBE growth of droplet-free GaN with very metal rich conditions using Metal Modulated Epitaxy with Mg and In", *Phys. Status Solidi C* **5**, 1855 (2008).

[29] M. Moseley, D. Billingsley, W. Henderson, E. Trybus and W. A. Doolittle, "Transient atomic behavior and surface kinetics of GaN", *J. Appl. Phys.* **106**, 014905 (2009).

[30] M. Moseley, J. Lowder, D. Billingsley and W. A. Doolittle, "Control of surface adatom kinetics for the growth of high-indium content InGaN throughout the miscibility gap", *Appl. Phys. Lett.* **97**, 191902 (2010).

[31] M. Moseley, B. Gunning, J. Greenlee, J. Lowder, G. Namkoong and W. A. Doolittle, "Observation and control of the surface kinetics of InGaN for the elimination of phase separation", *J. Appl. Phys.* **112**, 014909 (2012).

[32] J. E. Northrup, J. Neugebauer, R. M. Feenstra and A. R. Smith, "Structure of GaN(0001): The laterally contracted Ga bilayer model", *Phys. Rev. B* **61**, 9932 (2000).

[33] J. Neugebauer, T. K. Zywietz, M. Scheffler, J. E. Northrup, H. Chen and R. M. Feenstra, "Adatom Kinetics On and Below the Surface: The Existence of a New Diffusion Channel", *Phys. Rev. Lett.* **90**, 056101 (2003).

[34] S. Martini, A. A. Quivy, T. E. Lamas, M. J. d. Silva, E. C. F. d. Silva and J. R. Leite, "Influence of indium segregation on the RHEED oscillations during the growth of InGaAs layers on a GaAs(001) surface", *J. Cryst. Growth* **251**, 101 (2003).

[35] S. Martini, A. A. Quivy, E. C. F. d. Silva and J. R. Leite, "Real-time determination of the segregation strength of indium atoms in InGaAs layers grown by molecular-beam epitaxy", *Appl. Phys. Lett.* **81**, 2863 (2002).

[36] D. K. Gaskill, N. Bottka and M. C. Lin, "OMVPE of GaN and AlN films by metal alkyls and hydrazine", *J. Cryst. Growth* **77**, 418 (1986).

[37] S. Miyoshi, K. Onabe, N. Ohkouchi, H. Yagichi, R. Ito, S. Fukatsu and Y. Shiraki, "MOVPE growth of cubic GaN and GaAs using dimethylhydrazine", *J. Cryst. Growth* **124**, 439 (1992).

[38] M. Losurdo, P. Capezzuto and G. Bruno, "Remote plasma MOCVD growth and processing of GaN: A study by real time ellipsometry", *Phys. Status Solidi A* **176**, 733 (1999).

[39] C. H. Seager, A. F. Wright, J. Yu and W. Gotz, "Role of carbon in GaN", *J. Appl. Phys.* **92**, 6553 (2002).

[40] A. F. Wright, "Substitutional and interstitial carbon in wurtzite GaN", *J. Appl. Phys.* **92**, 2575 (2002).

[41] S. D. Burnham, W. A. Doolittle, G. Namkoong and W. Henderson, "Mg doped GaN using a valved, thermally energetic source: enhanced incorporation, control and quantitative optimization", *Materials Research Society Proceeding* **798**, Y8.11 (2003).

[42] S. D. Burnham, W. A. Doolittle, G. Namkoong and W. Henderson, "Mg doped GaN using a valved, thermally energetic source: enhanced incorporation, and control", *J. Cryst. Growth* **279**, 26 (2005).

[43] S. D. Burnham, Ph.D. Thesis, *Improved Understanding and Control of Magnesium-Doped Gallium Nitride by Plasma Assisted Molecular Beam Epitaxy*, Georgia Institute of Technology, 2007.

[44] G. Namkoong, E. Trybus, K. K. Lee, M. Moseley, W. A. Doolittle and D. C. Look, "Metal modulation epitaxy growth for extremely high hole concentrations above 10^{19} cm^{-3} in GaN", *Appl. Phys. Lett.* **93**, 172112 (2008).

[45] S. D. Burnham, G. Namkoong, D. C. Look, B. Clafin and W. A. Doolittle, "Reproducible increased Mg incorporation and large hole concentration in GaN using metal modulated epitaxy", *J. Appl. Phys.* **104**, 024902 (2008).

[46] U. K. Mishra, L. Shen, T. E. Kazior and Y.-F. Wu, "GaN-Based RF Power Devices and Amplifiers", *Proc. IEEE* **96**, 287 (2007).

[47] H. Xing, S. Keller, Y. F. Wu, L. McCarthy, I. P. Smorchkova, D. Buttary, J. J. Xu, B. P. Keller, S. P. DenBaars and U. K. Mishra, "Gallium nitride based transistors", *J. Phys.: Condens. Matter* **13**, 7139 (2001).

[48] S. Nakamura, T. Mukai and M. Senoh, "High-Power GaN P-N Junction Blue-Light-Emitting Diodes", *Jpn. J. Appl. Phys., Part 2* **30**, L1998 (1991).

[49] S. Nakamura, T. Mukai and M. Senoh, "Candela-class high-brightness InGaN/AlGaN double-heterostructure blue-light-emitting diodes", *Appl. Phys. Lett.* **64**, 1687 (1994).

[50] S. Nakamura, "InGaN-based violet laser diodes", *Semicond. Sci. Technol.* **14**, R27 (1999).

[51] T. Mukai, S. Nagahama, T. Kozaki, M. Sano, D. Morita, T. Yanamoto, M. Yamamoto, K. Akashi and S. Masui, "Current status and future prospects of GaN-based LEDs and LDs", *Phys. Status Solidi A* **201**, 2712 (2004).

[52] E. Trybus, G. Namkoong, W. Henderson, S. Burnham, W. A. Doolittle, M. Cheung and A. Cartwright, "InN: A material with photovoltaic promise and challenges", *J. Cryst. Growth* **288**, 218 (2006).

[53] E. Trybus, O. Jani, S. Burnham, I. Ferguson, C. Honsberg, M. Steiner and W. A. Doolittle, "Characteristics of InGaN designed for photovoltaic applications", *Phys. Status Solidi C* **5**, 1843 (2008).

[54] J. Wu, W. Walukiewicz, K. M. Yu, W. Shan, J. W. Ager, E. E. Haller, H. Lu, W. J. Schaff, W. K. Metzger and S. Kurtz, "Superior radiation resistance of $In_{1-x}Ga_xN$ alloys: Full-solar-spectrum photovoltaic material system", *J. Appl. Phys.* **94**, 6477 (2003).

[55] H. P. Maruska and J. J. Tietjen, "The preparation and properties of vapor-deposited single-crystalline GaN", *Appl. Phys. Lett.* **15**, 327 (1969).

[56] W. C. Johnson and J. B. Parsons, "Nitrogen Compounds of Gallium. I, II", *J. Phys. Chem.* **36**, 2588 (1932).

[57] R. Juza and H. Hahn, "Crystal structures of Cu3N, GaN, and InN -- Metallic amides and metallic nitrides", *Z. Anorg. Allg. Chem.* **239**, 282 (1938).

[58] H. Ott, "The grids of aluminum nitride", *Z. Phys. A: Hadrons Nucl.* **22**, 201 (1924).

[59] S. N. Mohammad and H. Morkoc, "Progress and Prospects of Group-III Nitride Semiconductors", *Prog. Quant. Electr.* **20**, 361 (1996).

[60] V. Y. Davidov, A. A. Klochikhin, R. P. Seisyan, V. V. Emtsev, S. V. Ivanov, F. Bechstedt, J. Furthmuller, H. Harima, A. V. Mudryi, J. Aderhold, O. Semchinova and J. Graul, "Absorption and Emission of Hexagonal InN. Evidence of Narrow Fundamental Band Gap", *Phys. Status Solidi B* **229**, R1 (2002).

[61] J. Wu, W. Walukiewicz, K. M. Yu, J. W. Ager, E. E. Haller, H. Lu, W. J. Schaff, Y. Saito and Y. Nanishi, "Unusual Properties of the Fundamental Band Gap of InN", *Appl. Phys. Lett.* **80**, 3967 (2002).

[62] Z. M. Lochner, Master's Thesis, *Green light emitting diodes and laser diodes grown by metalorganic chemical vapor deposition*, Georgia Institute of Technology, 2010.

[63] J. Wu, W. Walukiewicz, K. M. Yu, J. W. Ager, E. E. Haller, H. Lu and W. J. Schaff, "Narrow bandgap group III-nitride alloys", *Phys. Status Solidi B* **240**, 412 (2003).

[64] O. Katz, B. Meyler, U. Tisch and J. Salzman, "Determination of Band-Gap Bowing for $Al_xGa_{1-x}N$ Alloys", *Phys. Status Solidi A* **188**, 2001 (2001).

[65] I. Gorczyca, T. Suski, N. E. Christensen and A. Svane, "Gap bowing in $In_xGa_{1-x}N$ and $In_xAl_{1-x}N$ under pressure", *Phys. Status Solidi C* **6**, S368 (2009).

[66] J. Wu, "When group-III nitrides go infrared: New properties and perspectives", *J. Appl. Phys.* **106**, 011101 (2009).

[67] L. Liu and J. H. Edgar, "Substrates for gallium nitride epitaxy", *Mater. Sci. Eng., R* **37**, 61 (2002).

[68] T. P. Chow, "High-voltage SiC and GaN power devices", *Microelectron. Eng.* **83**, 112 (2006).

[69] B. Gelmont, K. Kim and M. Shur, "Monte Carlo simulation of electron transport in gallium nitride", *J. Appl. Phys.* **74**, 1818 (1993).

[70] M. A. Khan, R. A. Skogman, J. M. V. Hove, D. T. Olson and J. N. Kuznia, "Atomic layer epitaxy of GaN over sapphire using switched metalorganic chemical vapor deposition", *Appl. Phys. Lett.* **60**, 1366 (1992).

[71] I. Akasaki and H. Amano, "Recent progress of crystal growth, conductivity control and light emitters in group III nitride semiconductors", *Tech. Dig. Int. Electron Devices Meet.* **96**, 231 (1996).

[72] S. C. Jain, M. Willander, J. Narayan and R. V. Overstraeten, "III-nitrides: Growth, characterization, and properties", *J. Appl. Phys.* **87**, 965 (2000).

[73] J. R. Jinschek, R. Erni, N. F. Gardner, A. Y. Kim and C. Kisielowski, "Local indium segregation and band gap variations in high efficiency green light emitting InGaN/GaN diodes", *Solid State Commun.* **137**, 230 (2006).

[74] N. Grandjean and M. Ilegems, "Visible InGaN/GaN Quantum Dot Materials and Devices", *Proc. IEEE* **95**, 1853 (2007).

[75] F. Barkusky, C. Peth, A. Bayer, K. Mann, J. John and P. E. Malinowski, "Radiation damage resistance of AlGaN detectors for applications in the extreme-ultraviolet spectral range", *Rev. Sci. Instrum.* **80**, 093102 (2009).

[76] V. Rawat, D. N. Zakharov, E. A. Stach and T. D. Sands, "Pseudomorphic stabilization of rocksalt GaN in TiN/GaN multilayers and superlattices", *Phys. Rev. B* **80**, 024114 (2009).

[77] E. S. Hellman, "The polarity of GaN: a critical review", *MRS Internet J. Nitride Semicond. Res.* **3**, 11 (1998).

[78] N. Takeuchi, A. Selloni, T. H. Myers and A. Doolittle, "Adsorption and diffusion of Ga and N adatoms on GaN surfaces: Comparing the effects of Ga coverage and electronic excitation", *Phys. Rev. B* **72**, 115307 (2005).

[79] M. Sumiya and S. Fuke, "Review of polarity determination and control of GaN", *MRS Internet J. Nitride Semicond. Res.* **9**, 1 (2004).

[80] X. Q. Shen, T. Ide, S. H. Cho, M. Shimizu, S. Hara, H. Okumura, S. Sonoda and S. Shimizu, "Realization of Ga-polarity GaN films in radio-frequency plasma-assisted molecular beam epitaxy", *J. Cryst. Growth* **218**, 155 (2000).

[81] X. Q. Shen, T. Ide, S. H. Cho, M. Shimizu, S. Hara, H. Okumura, S. Sonoda and S. Shimizu, "Optimization of GaN Growth with Ga-Polarity by Referring to Surface Reconstruction Reflection High-Energy Electron Diffraction Patterns", *Jpn. J. Appl. Phys., Part 2* **40**, L23 (2001).

[82] M. A. Khan, J. N. Kuznia, J. M. V. Hove, N. Pan and J. Carter, "Observation of a two-dimensional electron gas in low pressure metalorganic chemical vapor deposited GaN-$Al_xGa_{a-x}N$ Heterojunctions", *Appl. Phys. Lett.* **60**, 3027 (1992).

[83] I. Akasaki, "Key inventions in the history of nitride-based blue LED and LD", *J. Cryst. Growth* **300**, 2 (2007).

[84] H. Amano, I. Akasaki, K. Hiramatsu, N. Koide and N. Sawaki, "Effects of the buffer layer in metalorganic vapour phase epitaxy of GaN on sapphire substrate", *Thin Solid Films* **163**, 415 (1988).

[85] H. Amano, N. Sawaki, I. Akasaki and Y. Toyoda, "Metalorganic vapor phase epitaxial growth of a high quality GaN film using an AlN buffer layer", *Appl. Phys. Lett.* **48**, 353 (1986).

[86] H. Amano, I. Akasaki, T. Kozawa, K. Hiramatsu, N. Sawaki, K. Ikeda and Y. Ishii, "Electron beam effects on blue luminescence of zinc-doped GaN", *J. Lumin.* **40**, 121 (1988).

[87] H. Amano, M. Kitoh, K. Hiramatsu and I. Akasaki, "Growth and Luminescence Properties of Mg-Doped GaN Prepared by MOVPE", *J. Electrochem. Soc.* **137**, 1639 (1990).

[88] H. Amano, M. Kito, K. Hiramatsu and I. Akasaki, "P-Type Conduction in Mg-Doped GaN Treated with Low-Energy Electron Beam Irradiation (LEEBI)", *Jpn. J. Appl. Phys.* **28**, L2112 (1989).

[89] S. Nakamura, M. Senoh, N. Iwasa and S. Nagahama, "High-power InGaN single-quantum-well-structure blue and violet light-emitting diodes", *Appl. Phys. Lett.* **67**, 1868 (1995).

[90] S. Nakamura, M. Senoh, N. Iwasa and S. Nagahama, "High-Brightness InGaN Blue, Green and Yellow Light-Emitting Diodes with Quantum Well Structures", *Jpn. J. Appl. Phys., Part 2* **34**, L797 (1995).

[91] S. Nakamura, M. Senoh, S. Nagahama, N. Iwasa, T. Yamada, T. Matsushita, Y. Sugimoto and H. Kiyoku, "Room-temperature continuous-wave operation of InGaN mult-quantum-well structure laser diodes", *Appl. Phys. Lett.* **69**, 4056 (1996).

[92] W. W. Chow, K. D. Choquette, M. H. Crawford, K. L. Lear and G. R. Hadley, "Design, fabrication, and performance of infrared and visible vertical-cavity surface-emitting lasers", *IEEE J. Quantum Electron.* **33**, 1810 (1997).

[93] J. Piprek, "Efficiency droop in nitride-based light-emitting diodes", *Phys. Status Solidi A* **207**, 2217 (2010).

[94] Y. C. Shen, G. O. Mueller, S. Watanabe, N. F. Gardner, A. Munkholm and M. R. Krames, "Auger recombination in InGaN measured by photoluminescence", *Appl. Phys. Lett.* **91**, 141101 (2007).

[95] J. Hader, J. V. Maloney and S. W. Koch, "Density-activated defect recombination as a possible explanation for the efficiency droop in GaN-based diodes", *Appl. Phys. Lett.* **96**, 221106 (2010).

[96] Q. Dai, M. F. Schubert, M. H. Kim, J. K. Kim, E. F. Schubert, D. D. Koleske, M. H. Crawford, S. R. Lee, A. J. Fischer, G. Thaler and M. A. Banas, "Internal

quantum efficiency and nonradiative recombination coefficient of GaInN/GaN multiple quantum wells with different dislocation densities", *Appl. Phys. Lett.* **94**, 111109 (2009).

[97] M. H. Kim, M. F. Schubert, Q. Dai, J. K. Kim, E. F. Schubert, J. Piprek and Y. Park, "Origin of efficiency droop in GaN-based light-emitting diodes", *Appl. Phys. Lett.* **91**, 183507 (2007).

[98] I. V. Rozhansky and D. A. Zakheim, "Analysis of processes limiting quantum efficiency of AlGaInN LEDs at high pumping", *Phys. Status Solidi A* **204**, 227 (2007).

[99] A. A. Efremov, N. I. Bochkareva, R. I. Gorbunov, D. A. Lavrinovich, Y. T. Rebane, D. V. Tarkhin and Y. G. Shreter, "Effect of the Joule Heating on the Quantum Efficiency and Choice of Thermal Conditions for High-Power Blue InGaN/GaN LEDs", *Semiconductors* **40**, 605 (2006).

[100] D. A. Zakheim, A. S. Pavluchenko and D. A. Bauman, "Blue LEDs - way to overcome efficiency droop", *Phys. Status Solidi C* **8**, 2340 (2011).

[101] X. Li, H. Liu, X. Ni, U. Ozgur and H. Morkoc, "Effect of carrier spillover and Auger recombination on the efficiency droop in InGaN-based blue LEDs", *Superlattices Microstruct.* **47**, 118 (2010).

[102] X. Ni, Q. Fan, R. Shimada, Ü. Özgür and H. Morkoç, "Reduction of efficiency droop in InGaN light emitting diodes by coupled quantum wells", *Appl. Phys. Lett.* **93**, 171113 (2008).

[103] X. Li, X. Ni, J. Lee, M. Wu, Ü. Özgür, H. Morkoç, T. Paskova, G. Mulholland and K. R. Evans, "Efficiency retention at high current injection levels in m-plane InGaN light emitting diodes", *Appl. Phys. Lett.* **95**, 121107 (2009).

[104] C. H. Wang, C. C. Ke, C. Y. Lee, S. P. Chang, W. T. Chang, J. C. Li, Z. Y. Li, H. C. Yang, H. C. Kuo, T. C. Lu and S. C. Wang, "Hole injection and efficiency droop improvement in InGaN/GaN light-emitting diodes by band-engineered electron blocking layer", *Appl. Phys. Lett.* **97**, 261103 (2010).

[105] J. H. Ryou, W. Lee, J. Limb, D. Yoo, J. P. Liu, R. D. Dupuis, Z. H. Wu, A. M. Fischer and F. A. Ponce, "Control of quantum-confined Stark effect in InGaN/GaN multiple quantum well active region by p-type layer for III-nitride based visible light emitting diodes", *Appl. Phys. Lett.* **92**, 101113 (2008).

[106] Z. C. Feng, W. Liu, S. J. Chua, J. H. Chen, C. C. Yang, W. Lu and W. E. Collins, "Recombination mechanism of InGaN multiple quantum wells grown by metalorganic chemical vapor deposition", *Phys. Status Solidi C* **2**, 2377 (2005).

[107] M. Strassburg, A. Hoffmann, J. Holst, J. Christen, T. Riemann, F. Bertram and P. Fischer, "The origin of the PL photoluminescence Stokes shift in ternary group-III nitrides: field effects and localization", *Phys. Status Solidi C* **0**, 1835 (2003).

[108] H. Ohta and K. Okamoto, "Nonpolar/semipolar GaN Technology for Violet, Blue, and Green Laser Diodes", *MRS Bull.* **34**, 324 (2009).

[109] H. Masui and S. Nakamura, "Nonpolar and Semipolar Orientations: Material Growth and Properties", *Mater. Sci. Forum* **590**, 211 (2008).

[110] B. L. VanMil, H. Guo, L. J. Holbert, K. Lee, C. H. Swartz, T. Liu, D. Korakakis and T. H. Myers, "High temperature limitations for GaN growth by RF-plasma assisted molecular beam epitaxy: Effects of active nitrogen species, surface polarity, and excess Ga-overpressure", *Phys. Status Solidi C* **2**, 2174 (2005).

[111] O. Ambacher, B. Foutz, J. Smart, J. R. Shealy, N. G. Weimann, K. Chu, M. Murphy, A. J. Sierakowski, W. J. Schaff, L. F. Eastman, R. Dimitrov, A. Mitchell and M. Stutzmann, "Two dimensional electron gases induced by spontaneous and piezoelectric polarization in undoped and doped AlGaN/GaN heterostructures", *J. Appl. Phys.* **87**, 334 (2000).

[112] O. Ambacher, A. Link, S. Hackenbuchner, M. Stutzmann, R. Dimitrov, M. Murphy, J. Smart, J. R. Shealy, B. Green, W. J. Schaff and L. F. Eastman, "2DEGs and 2DHGs Induced by Spontaneous and Piezoelectric Polarization in AlGaN/GaN Heterostructures", *Mat. Res. Soc. Symp. Proc.* **622**, T5.10.1 (2000).

[113] A. Khan, J. N. Kuznia, D. T. Olson, W. J. Schaff, J. W. Burm and M. S. Shur, "Microwave performance of a 0.25 μm gate AlGAN/GaN heterostructure field effect transistor", *Appl. Phys. Lett.* **65**, 1121 (1994).

[114] J. Jasinski and Z. Liliental-Weber, "Extended Defectsand Polarity of Hydride Vapor Phase Epitaxy GaN", *J. Electron. Mater.* **31**, 429 (2002).

[115] D. Holec, P. Costa, M. Kappers and C. Humphreys, "Critical thickness calculations for InGaN/GaN", *J. Cryst. Growth* **303**, 314 (2007).

[116] G. B. Stringfellow, "Microstructures produced during the epitaxial growth of InGaN alloys", *J. Cryst. Growth* **312**, 735 (2010).

[117] G. Namkoong, S. Burnham, K.-K. Lee, E. Trybus and W. A. Doolittle, "III-nitrides on oxygen- and zinc-face ZnO substrates", *Appl. Phys. Lett.* **87**, 184104 (2005).

[118] A. Janotti and C. G. Van De Walle, "Fundamentals of zinc oxide as a semiconductor", *Rep. Prog. Phys.* **72**, 126501 (2009).

[119] T. Paskova, D. A. Hanser and K. R. Evans, "GaN Substrates for III-Nitride Devices", *Proc. IEEE* **98**, 1324 (2010).

[120] W. A. Doolittle, T. Kropewnicki, C. Carter-Coman, S. Stock, P. Kohn, N. M. Jokerst, R. A. Metzger, S. Kang, K. K. Lee, G. May and A. S. Brown, "Growth of GaN on lithium gallate substrates for development of a GaN thin compliant substrate", *J. Vac. Sci. Technol. B* **16**, 1300 (1998).

[121] G. Namkoong, S. Huang, M. Moseley and W. A. Doolittle, "In-plane anisotropic strain of elastically and plastically deformed III-nitrides on lithium gallate", *accepted to Thin Solid Films* (2009).

[122] L. M. Sorokin, A. E. Kalmykov, V. N. Besselov, N. A. Feoktistov, A. V. Osipov, S. A. Kukushkin and N. V. Veselov, "Structural Characterization of GaN Epilayers on Silicon: Effect of Buffer Layers", *Tech. Phys. Lett.* **37**, 326 (2011).

[123] G. Thaler, D. Koleske, S. Lee, K. Bogart and M. Crawford, "Thermal stability of thin InGaN films on GaN", *J. Cryst. Growth* **312**, 1817 (2010).

[124] F. K. Yam and Z. Hassan, "InGaN: An overview of the growth kinetics, physical properties, and emission mechanisms", *Superlattices Microstruct.* **43**, 1 (2008).

[125] Y. Nanishi, Y. Saito, T. Yamaguchi, M. Hori, F. Matsuda, T. Araki, A. Suzuki and T. Miyajima, "MBE growth, characterization and properties of InN and InGaN", *Phys. Status Solidi A* **200**, 202 (2003).

[126] I. Stanley, G. Coleiny and R. Venkat, "Theoretical Study of In desorption and segregation kinetics in MBE growth of InGaAs and InGaN", *J. Cryst. Growth* **251**, 23 (2003).

[127] Y. Saito, N. Teraguchi, A. Suzuki, T. Araki and Y. Nanishi, "Growth of High-Electron-Mobility InN by RF Molecular Beam Epitaxy", *Jpn. J. Appl. Phys.* **40**, 91 (2001).

[128] A. Zukauskas, K. Kazlauskas, G. Tamulaitis, P. Pobedinskas, S. Jursenas, S. Miasojedovas, V. Y. Ivanov, M. Godlewski, C. Skierbiszewski, M. Siekacz, G. Franssen, P. Perlin, T. Suski and I. Grzegory, "Role of band potential roughness on the luminescence properties of InGaN quantum wells grown by MBE on bulk GaN substrates", *Phys. Status Solidi B* **243**, 1614 (2006).

[129] Z. H. Wu, Y. Kawai, Y. Y. Fang, C. Q. Chen, H. Kondo, M. Hori, Y. Honda, M. Yamaguchi and H. Amano, "Spontaneous formation of highly regular superlattice structure in InGaN epilayers grown by molecular beam epitaxy", *Appl. Phys. Lett.* **98**, 141905 (2011).

[130] E. Hahn, A. Rosenauer, D. Gerthsen, J. Off, V. Perez-Solorzano, M. Jetter and F. Scholz, "In-Redistribution in a GaInN Quantum Well upon Thermal Annealing", *Phys. Status Solidi B* **234**, 738 (2002).

[131] S. Y. Karpov and Y. N. Makarov, "Surface Segregation in Group-III Nitride MBE", *Phys. Status Solidi A* **188**, 611 (2001).

[132] H. Chen, R. M. Feenstra, J. E. Northrup, T. Zywietz and J. Neugebauer, "Spontaneous Formation of Indium-Rich Nanostructures on InGaN(0001) Surfaces", *Phys. Rev. Lett.* **85**, 1902 (2000).

[133] S. Choi, T.-H. Kim, S. Wolter, A. Brown, H. O. Everitt, M. Losurdo and G. Bruno, "Indium adlayer kinetics on the gallium nitride (0001) surface: Monitoring indium segregation and precursor-mediated adsorption", *Phys. Rev. B* **77**, 115435 (2008).

[134] S. Y. Karpov and Y. N. Makarov, "Indium segregation kinetics in InGaAs ternary compounds", *Thin Solid Films* **380**, 71 (2000).

[135] J. Neugebauer, "Surfactants and antisurfactants on group-III-nitride surfaces", *Phys. Status Solidi C* **0**, 1651 (2003).

[136] E. Monroy, N. Gogneau, D. Jalabert, E. Bellet-Amalric and Y. Hori, "In incorporation during the growth of quaternary III-nitride compounds by plasma-assisted molecular beam epitaxy", *Appl. Phys. Lett.* **82**, 2242 (2003).

[137] O. Brandt, P. Waltereit, U. Jahn, S. Dhar and K. H. Ploog, "Impact of In Bulk and Surface Segregation on the Optical Properties of (In,Ga)N/GaN Multiple Quantum Wells", *Phys. Status Solidi A* **192**, 5 (2002).

[138] A. Dussaigne, B. Damilano, N. Grandjean and J. Massies, "In surface segregation in InGaN/GaN quantum wells", *J. Cryst. Growth* **251**, 471 (2003).

[139] H. Chen, R. M. Feenstra, J. E. Northrup, T. Zywietz, J. Neugebauer and D. W. Greve, "Surface structures and growth kinetics of InGaN(0001) grown by molecular beam epitaxy", *J. Vac. Sci. Technol. B* **18**, 2284 (2000).

[140] S. Nakamura, "The Roles of Structural Imperfections in InGaN-Based Blue Light-Emitting Diodes and Laser Diodes", *Science* **281**, 956 (1998).

[141] E. Monroy, B. Daudin, N. Gogneau, E. Bellet-Amalric, D. Jalabert and J. Brault, "Assessment of AlGaN growth by Plasma Assisted MBE Using In as a Surfactant", *Phys. Status Solidi B* **234**, 726 (2002).

[142] I. Berishev, E. Kim, A. Fartassi, M. Sayhi and A. Bensaoula, "Mg doping studies of electron cyclotron resonance molecular beam epitaxy of GaN thin films ", *J. Vac. Sci. Technol. A* **17**, 2166 (1999).

[143] C. G. Van De Walle, C. Stampfl and J. Neugebauer, "Theory of doping and defects in III-V Nitrides", *J. Cryst. Growth* **189/190**, 505 (1998).

[144] V. Ramachandran, R. M. Feenstra, W. L. Sarney, L. Salamanca-Riba, J. E. Northrup, L. T. Romano and D. W. Greve, "Inversion of wurtzite GaN(0001) by exposure to magnesium", *Appl. Phys. Lett.* **75**, 808 (1999).

[145] W. Gotz, N. M. Johnson, J. Walker, D. P. Bour and R. A. Street, "Activation of acceptors in Mg-doped GaN grown by metalorganic chemical vapor deposition", *Appl. Phys. Lett.* **68**, 667 (1995).

[146] W. Kim, A. Salvador, A. E. Botchkarev, O. Aktas, S. N. Mohammad and H. Morkoc, "Mg-doped p-type GaN grown by reactive molecular beam epitaxy", *Appl. Phys. Lett.* **69**, 559 (1996).

[147] A. Bhattacharyya, W. Li, J. Cabalu, T. D. Moustakas, D. J. Smith and R. L. Hervig, "Efficient p-type doping of GaN films by plasma-assisted molecular beam epitaxy", *Appl. Phys. Lett.* **85**, 4956 (2004).

[148] M. McLaurin, T. E. Yates and J. S. Speck, "Molecular-beam epitaxy of p-type m-plane GaN", *Appl. Phys. Lett.* **86**, 262104 (2005).

[149] M. McLaurin, T. E. Mates, F. Wu and J. S. Speck, "Growth of p-type and n-type m-plane GaN by molecular beam epitaxy", *Appl. Phys. Lett.* **100**, 063707 (2006).

[150] S. K. O'Leary, B. E. Foutz, M. S. Shur and L. F. Eastman, "Steady-State and Transient Electron Transport Within the III-V Nitride Semiconductors, GaN, AlN, and InN: A Review", *J. Mater. Sci. - Mater. Electron.* **17**, 87 (2006).

[151] C. J. Neufeld, N. G. Toledo, S. C. Cruz, M. Iza, S. P. DenBaars and U. K. Mishra, "High quantum efficiency in InGaN/GaN solar cells with 2.95 eV band gap", *Appl. Phys. Lett.* **93**, 143502 (2008).

[152] V. Kumar, W. Lu, R. Schwindt, A. Kuliev, G. Simin, J. Yang, M. A. Khan and I. Adesida, "AlGaN/GaN HEMTs on SiC with f_T of Over 120 GHz", *IEEE Electron Device Lett.* **23**, 455 (2002).

[153] E. Trybus, W. A. Doolittle, M. Moseley, W. Henderson, D. Billingsley, G. Namkoong and D. C. Look, "Extremely high hole concentrations in c-plane GaN", *Phys. Status Solidi C* **6**, S788 (2009).

[154] C. Munasinghe and A. J. Steckl, "GaN:Eu electroluminescent devices grown by interrupted growth epitaxy", *Thin Solid Films* **496**, 636 (2006).

[155] C. Poblenz, P. Waltereit and J. S. Speck, "Uniformity and control of surface morphology during growth of GaN by molecular beam epitaxy", *J. Vac. Sci. Technol. B* **23**, 1379 (2005).

[156] N. Gogneau, E. Sarigiannidou, E. Monroy, S. Monnoye, H. Mank and B. Daudin, "Surfactant effect of gallium during the growth of GaN on AlN(000-1) by plasma-assisted molecular beam epitaxy", *Appl. Phys. Lett.* **85**, 1421 (2004).

[157] M. Losurdo, P. Capezzuto, G. Bruno, G. Namkoong, W. A. Doolittle and A. S. Brown, "The Chemistry of Sapphire Nitridation in Relation to the GaN Structural Quality: Why Low Temperature 200 C Nitridation?", *Phys. Status Solidi A* **188**, 561 (2001).

[158] M. Losurdo, P. Capezzuto, G. Bruno, G. Namkoong, W. A. Doolittle and A. S. Brown, "Role of sapphire nitridation temperature on GaN growth by plasma assisted molecular beam epitaxy: Part II. Interplay between chemistry and structure of layers", *J. Appl. Phys.* **91**, 2508 (2002).

[159] G. Namkoong, W. A. Doolittle and A. S. Brown, "Role of low-temperature (200 C) nitridation in the growth of GaN by plasma-assisted molecular-beam epitaxy", *J. Vac. Sci. Technol. B* **20**, 1221 (2002).

[160] G. Namkoong, W. A. Doolittle, A. S. Brown, M. Losurdo, P. Capezzuto and G. Bruno, "Role of sapphire nitridation temperature on GaN growth by plasma assisted molecular beam epitaxy: Part I. Impact of the nitridation chemistry on material characteristics", *J. Appl. Phys.* **91**, 2499 (2002).

[161] G. Namkoong, W. A. Doolittle, A. S. Brown, M. Losurdo, M. M. Giangregorio and G. Bruno, "The impact of substrate nitridation temperature and buffer design and synthesis on the polarity of GaN epitaxial films", *J. Cryst. Growth* **252**, 159 (2003).

[162] G. Namkoong, W. A. Doolittle, A. S. Brown, M. Losurdo, M. M. Giangregorio and G. Bruno, "Effect of Buffer Design on AlGaN/AlN/GaN Heterostructures by MBE", *Mater. Res. Soc. Symp. Proc.* **798**, 359 (2004).

[163] Y. Tazoh, T. Ishii and S. Miyazawa, "GaN Thin Film Growth on $LiGaO_2$ Substrate with a Multi-Domain Structure", *Jpn. J. Appl. Phys., Part 2* **36**, L746 (1997).

[164] T. Ishii, Y. Tazoh and S. Miyazawa, "Single-crystal growth of $LiGaO_2$ for a substrate of GaN thin Þlms", *J. Cryst. Growth* **1998**, 409 (1998).

[165] W. A. Doolittle, S. Kang and A. Brown, "MBE growth of high quality GaN on $LiGaO_2$ for high frequency, high power electronic applications", *Solid-State Electron.* **44**, 229 (2000).

[166] A. S. Brown and W. A. Doolittle, "The status and promise of compliant substrate technology", *Appl. Surf. Sci.* **166**, 392 (2000).

[167] S. Kang, Ph.D. Thesis, *The Epitaxial Growth of GaN and AlGaN/GaN Heterostructure Field Effect Transistors (HFET) on Lithium Gallate ($LiGaO_2$) Substrates*, Georgia Institute of Technology, 2002.

[168] W. Seifert, N. Carlsson, M. Miller, M.-E. Pistol, L. Samuelson and L. R. Wallenberg, "In-situ growth of quantum dot structures by the Stranski-Krastanow growth mode", *Prog. Cryst. Growth Charact. Mater.* **33**, 423 (1996).

[169] A. Christensen, W. A. Doolittle and S. Graham, "Heat Dissipation in High-Power GaN Electronics on Thermally Resistive Substrates", *IEEE Trans. Electron Devices* **52**, 1683 (2005).

[170] R. Klauser, P. S. A. Kumar and T. J. Chuang, "A synchrotron radiation photoemission study of gallium and nitrogen adsorption on 6H-SiC, LiGaO2 and GaN substrates: initial stages of GaN formation", *Surf. Sci.* **411**, 329 (1998).

[171] J. H. Edgar, S. Strite, I. Akasaki, H. Amano and C. Wetzel, eds. *Properties, Processing and Applications of Gallium Nitride and Related Semiconductors*. 1999, INSPEC, The Institution of Electrical Engineers: London, UK.

[172] K. Iwata, H. Asahi, S. J. Yu, K. Asami, H. Fujita, M. Fushida and S.-i. Gonda, "High Quality GaN Growth on (0001) Sapphire by Ion-Removed Electron Cyclotron Resonance Molecular Beam Epitaxy and First Observation of (2x2) and (4x4) Reflection High Energy Electron Diffraction Patterns", *Jpn. J. Appl. Phys., Part 2* **35**, L289 (1996).

[173] S. Fernandez-Garrido, G. Koblmuller, E. Calleja and J. S. Speck, "In situ GaN decomposition analysis by quadrupole mass spectrometry and reflection high-energy electron diffraction", *J. Appl. Phys.* **104**, 033541 (2008).

[174] R. R. Lieten, V. Motsnyi, L. Zhang, K. Cheng, M. Leys, S. Degroote, G. Buchowicz, O. Dubon and G. Borghs, "Mg doping of GaN by molecular beam epitaxy", *J. Phys. D: Appl. Phys.* **44**, 135406 (2011).

[175] L. S. Chuah, Z. Hassan and H. A. Hassan, "Ohmic contacts properties of Ni/Ag metallization scheme on p-type GaN", *J. Non-Cryst. Solids* **356**, 181 (2010).

[176] J. O. Song, J.-S. Ha and T.-Y. Seong, "Ohmic-Contact Technology for GaN-Based Light-Emitting Diodes: Role of P-Type Contact", *IEEE Trans. Electron Devices* **57**, 42 (2010).

[177] J. Xie, X. Ni, Q. Fan, R. Shimada, Ü. Özgür and H. Morkoç, "On the efficiency droop in InGaN multiple quantum well blue light emitting diodes and its reduction with p-doped quantum well barriers", *Appl. Phys. Lett.* **93**, 121107 (2008).

[178] M. A. Sanchez-Garcia, E. Calleja, E. Monroy, F. J. Sanchez, F. Calle, E. Munoz and R. Beresford, "The effect of the III/V ratio and substrate temperature on the morphology and properties of GaN- and AlN-layers grown by molecular beam epitaxy on Si(111)", *J. Cryst. Growth* **193**, 23 (1998).

[179] M. A. Sanchez-Garcia, J. L. Pau, F. Naranjo, A. Jimenez, S. Fernandez, J. Ristic, F. Calle, E. Calleja and E. Munoz, "Plasma-assisted MBE growth of group-III nitrides: from basics to device applications", *Mater. Sci. Eng., B* **93**, 189 (2002).

[180] M. Zhang, P. Bhattacharya, W. Guo and A. Banerjee, "Mg doping of GaN grown by plasma-assisted molecular beam epitaxy under nitrogen-rich conditions", *Appl. Phys. Lett.* **96**, 132103 (2010).

[181] U. Kaufmann, P. Schlotter, H. Obloh, K. Kohler and M. Maier, "Hole conductivity and compensation in epitaxial GaN:Mg layers", *Phys. Rev. B* **62**, 10867 (2000).

[182] Y. Xian, S. Huang, Z. Zheng, B. Fan, Z. Wu, H. Jiang and G. Wang, "Effects of growth pressure on the properties of p-GaN layers", *J. Cryst. Growth* **325**, 32 (2011).

[183] C. Guarneros and V. Sanchez, "Magnesium doped GaN grown by MOCVD", *Mater. Sci. Eng., B* **174**, 263 (2010).

[184] R. Singh, D. Doppalapudi and T. D. Moustakas, "Phase sepaation in InGaN thick films and formation of InGaN/GaN double heterostructures in the entire alloy composition", *Appl. Phys. Lett.* **70**, 1089 (1997).

[185] J. Zheng and J. Kang, "Theoretical study of phase separation in wurtzite InGaN", *Mater. Sci. Semicond. Process.* **9**, 341 (2006).

[186] H. K. Cho, J. Y. Lee, C. S. Kim and G. M. Yang, "Influence of strain relaxation on structural and optical characteristics of InGaN/GaN multiple quantum wells with high indium composition", *J. Appl. Phys.* **91**, 1166 (2002).

[187] P. M. F. J. Costa, R. Datta, M. J. Kappers, M. E. Vickers, C. J. Humphreys, D. M. Graham, P. Dawson, M. J. Godfrey, E. J. Thrush and J. T. Mullins, "Misfit

dislocations in In-rich InGaN/GaN quantum well structures", *Phys. Status Solidi A* **203**, 1729 (2006).

[188] J. J. Harris, B. A. Joyce and P. J. Dobson, "Oscillations in the Surface Structure of Sn-Doped GaAs During Growth by MBE", *Surf. Sci.* **103**, L90 (1981).

[189] Y. Moriyasu, H. Goto, N. Kuze and M. Matsui, "In situ monitoring of reflection high-energy electron diffraction oscillation during the growth of gallium nitride films by gas-source molecular beam epitaxy", *J. Cryst. Growth* **150**, 916 (1995).

[190] B. Daudin and F. Widmann, "Layer-by-layer growth of AlN and GaN by molecular beam epitaxy", *J. Cryst. Growth* **182**, 1 (1997).

[191] W. Braun, L. Daweritz and K. H. Ploog, "Origin of Electron Diffraction Oscillations during Crystal Growth", *Phys. Rev. Lett.* **80**, 4935 (1998).

[192] C. S. Gallinat, G. Koblmuller, J. S. Brown and J. S. Speck, "A growth diagram for plasma-assisted molecular beam epitaxy of In-face InN", *J. Appl. Phys.* **102**, 064907 (2007).

[193] F. Fischer and F. Schröter, "Über neue Metall-Stickstoff-Verbindungen und ihre Stabilität an der Hand des periodischen Systems", *Ber Deut. Chem. Ges.* **43**, 1465 (1910).

[194] K. Westra, R. Lawson and M. Brett, "The effects of oxygen contamination on the properties of reactively sputtered indium nitride films", *J. Vac. Sci. Technol. A* **6**, 1730 (1988).

[195] K. Osamura, S. Naka and Y. Murakami, "Preparation and optical properties of $Ga_{1-x}In_xN$ thin films", *J. Appl. Phys.* **46**, 3432 (1975).

[196] T. Matsuoka, H. Tanaka, T. Sasaki and A. Katsui, "Wide-gap semiconductor (In, Ga) N", *Inst. Phys. Conf. Ser* **106**, 141 (1990).

[197] W. Hoke, P. Lemonias and D. Weir, "Evaluation of a new plasma source for molecular beam epitaxial growth of InN and GaN films", *J. Cryst. Growth* **111**, 1024 (1991).

[198] M. Higashiwaki and T. Matsui, "High-quality InN film grown on a low-temperature-grown GaN intermediate layer by plasma-assisted molecular-beam epitaxy", *Jpn. J. Appl. Phys.* **41**, 540 (2002).

[199] H. Lu, W. J. Schaff, J. Hwang, H. Wu, G. Koley and L. F. Eastman, "Effect of an AlN buffer layer on the epitaxial growth of InN by molecular-beam epitaxy", *Appl. Phys. Lett.* **79**, 1489 (2001).

[200] E. Trybus, G. Namkoong, W. Henderson, W. A. Doolittle, R. Liu, J. Mei, F. Ponce, M. Cheung, F. Chen and M. Furis, "Growth of InN on Ge substrate by molecular beam epitaxy", *J. Cryst. Growth* **279**, 311 (2005).

[201] A. G. Bhuiyan, A. Hashimoto and A. Yamamoto, "Indium nitride (InN): A review on growth, characterization, and properties", *J. Appl. Phys.* **94**, 2779 (2003).

[202] R. Jones, K. Yu, S. Li, W. Walukiewicz, J. Ager, E. Haller, H. Lu and W. Schaff, "Evidence for p-type doping of InN", *Phys. Rev. Lett.* **96**, 125505 (2006).

[203] J. Ager, N. Miller, R. Jones, K. Yu, J. Wu, W. Schaff and W. Walukiewicz, "Mg-doped InN and InGaN–Photoluminescence, capacitance–voltage and thermopower measurements", *Phys. Status Solidi B* **245**, 873 (2008).

[204] ASTM Standard F76, *Test Methods for Measuring Resistivity and Hall Coefficient and Determining Hall Mobility in Single-Crystal Semiconductors*, (ASTM International, West Conshohocken, PA, 2011)

[205] B. Arnaudov, T. Paskova, S. Evtimova, B. Monemar, H. Lu and W. J. Schaff, "Electron concentration and mobility profiles in InN layers grown by MBE", *Phys. Status Solidi A* **203**, 1681 (2006).

[206] Y. Nanishi, Y. Saito and T. Yamaguchi, "RF-molecular beam epitaxy growth and properties of InN and related alloys", *Jpn. J. Appl. Phys.* **42**, 2549 (2003).

[207] H. Lu, W. J. Schaff, L. F. Eastman and C. E. Stutz, "Surface charge accumulation of InN films grown by molecular-beam epitaxy", *Appl. Phys. Lett.* **82**, 1736 (2003).

[208] I. Mahboob, T. D. Veal, C. F. McConville, H. Lu and W. J. Schaff, "Intrinsic Electron Accumulation at Clean InN Surfaces", *Phys. Rev. Lett.* **92**, 036804 (2004).

[209] W. Walukiewicz, J. Ager III, K. Yu, Z. Liliental-Weber, J. Wu, S. Li, R. Jones and J. Denlinger, "Structure and electronic properties of InN and In-rich group III-nitride alloys", *J. Phys. D: Appl. Phys.* **39**, R83 (2006).

[210] T. L. Tansley and R. J. Egan, "Point-defect energies in the nitrides of aluminum, gallium, and indium", *Phys. Rev. B* **45**, 10942 (1992).

[211] C. Van de Walle, J. Lyons and A. Janotti, "Controlling the conductivity of InN", *Phys. Status Solidi A* **207**, 1024 (2010).

[212] D. C. Look, G. C. Farlow, P. J. Drevinsky, D. F. Bliss and J. R. Sizelove, "On the nitrogen vacancy in GaN", *Appl. Phys. Lett.* **83**, 3525 (2003).

[213] S. Spruytte, M. Larson, W. Wampler, C. Coldren, H. Petersen and J. Harris, "Nitrogen incorporation in group III–nitride–arsenide materials grown by elemental source molecular beam epitaxy", *J. Cryst. Growth* **227**, 506 (2001).

[214] M. S. Shur and A. Zukauskas, "Solid-State Lighting: Toward Superior Illumination", *Proc. IEEE* **93**, 1691 (2005).

[215] A. Khan, K. Balakrishnan and T. Katona, "Ultraviolet light-emitting diodes based on group three nitrides", *Nat. Photonics* **2**, 77 (2008).

[216] C. Honsberg, W. A. Doolittle, M. Allen and C. Wang, "GaN betavoltaic energy converters", *Photovoltaic Specialists Conference*, 2005.

[217] A. Allerman, M. Crawford, A. Fischer, K. Bogart, S. Lee, D. Follstaedt, P. Provencio and D. Koleske, "Growth and design of deep-UV (240–290nm) light emitting diodes using AlGaN alloys", *J. Cryst. Growth* **272**, 227 (2004).

[218] M. Kneissl, T. Kolbe, C. Chua, V. Kueller, N. Lobo, J. Stellmach, A. Knauer, H. Rodriguez, S. Einfeldt and Z. Yang, "Advances in group III-nitride-based deep UV light-emitting diode technology", *Semicond. Sci. Technol.* **26**, 014036 (2010).

[219] B. Gunning, J. Lowder, M. Moseley and W. Alan Doolittle, "Negligible carrier freeze-out facilitated by impurity band conduction in highly p-type GaN", *Appl. Phys. Lett.* **101**, 082106 (2012).

[220] A. Holmes, K. Fertitta, F. Ciuba and R. Dupuis, "X-ray diffraction studies of high-quality GaN heteroepitaxial films grown by metal organic chemical vapour deposition", *Electron. Lett.* **30**, 1252 (1994).

[221] L. Romano, B. Krusor, R. Singh and T. Moustakas, "Structure of GaN films grown by molecular beam epitaxy on (0001) sapphire", *J. Electron. Mater.* **26**, 285 (1997).

[222] L. Vegard, "Die konstitution der mischkristalle und die raumfüllung der atome", *Z. Phys. A-Hadron. Nucl.* **5**, 17 (1921).

[223] E. Trybus, Ph.D. Thesis, *Molecular beam epitaxy growth of indium nitride and indium gallium nitride materials for photovoltaic applications*, Georgia Institute of Technology, 2009.

[224] L. Wang, R. Li, D. Li, N. Liu, L. Liu, W. Chen, C. Wang, Z. Yang and X. Hu, "Strain modulation-enhanced Mg acceptor activation efficiency of AlGaN/GaN superlattices with AlN interlayer", *Appl. Phys. Lett.* **96**, 061110 (2010).

[225] K. Nagamatsu, K. Takeda, T. Mori, H. Tsuzuki, M. Iwaya, S. Kamiyama and I. Akasaki, "Growth and conductivity control of high quality AlGaN and its

application to high-performance ultraviolet laser diodes", *Proc. of SPIE* **7216**, 72161B (2009).

[226] T. Mori, K. Nagamatsu, K. Nonaka, K. Takeda, M. Iwaya, S. Kamiyama, H. Amano and I. Akasaki, "Crystal growth and p-type conductivity control of AlGaN for high-efficiency nitride-based UV emitters", *Phys. Status Solidi C* **6**, 2621 (2009).

[227] F. Bechstedt, U. Grossner and J. Furthmüller, "Dynamics and polarization of group-III nitride lattices: A first-principles study", *Phys. Rev. B* **62**, 8003 (2000).

[228] M. S. Shur, R. Gaska and A. Khan, "III-Nitride Power Devices-Good Results and Great Expectations", *Mater. Sci. Forum* **353**, 807 (2001).

[229] C. Oxley, "Gallium nitride: the promise of high RF power and low microwave noise performance in S and I band", *Solid-State Electron.* **48**, 1197 (2004).

[230] M. A. Khan, M. Shatalov, H. Maruska, H. Wang and E. Kuokstis, "III-nitride UV devices", *Jpn. J. Appl. Phys.* **44**, 711 (2005).

[231] I. Akasaki and H. Amano, "Widegap Column-III Nitride Semiconductors for UV/Blue Light Emitting Devices", *J. Electrochem. Soc.* **141**, 2266 (1994).

[232] F. Ponce and D. Bour, "Nitride-based semiconductors for blue and green light-emitting devices", *Nature* **386**, 351 (1997).

[233] S. Strite and H. Morkoc, "GaN, AlN, and InN: a review", *J. Vac. Sci. Technol. B* **10**, 1237 (1992).

[234] O. Ambacher, "Growth and applications of group III-nitrides", *J. Phys. D: Appl. Phys.* **31**, 2653 (1999).

[235] H. Amano, M. Iwaya, T. Kashima, M. Katsuragawa, I. Akasaki, J. Han, S. Hearne, J. Floro, E. Chason and J. Figiel, "Stress and defect control in GaN using low temperature interlayers", *Jpn. J. Appl. Phys.* **37**, L1540 (1998).

[236] K. Hiramatsu, S. Itoh, H. Amano, I. Akasaki, N. Kuwano, T. Shiraishi and K. Oki, "Growth mechanism of GaN grown on sapphire with A1N buffer layer by MOVPE", *J. Cryst. Growth* **115**, 628 (1991).

[237] X. Wu, D. Kapolnek, E. Tarsa, B. Heying, S. Keller, B. Keller, U. Mishra, S. DenBaars and J. Speck, "Nucleation layer evolution in metal-organic chemical vapor deposition grown GaN", *Appl. Phys. Lett.* **68**, 1371 (1996).

[238] E. Etzkorn and D. Clarke, "Cracking of GaN films", *J. Appl. Phys.* **89**, 1025 (2001).

[239] Y. Sung, H. Kim, Y. Lee, J. Lee, S. Chae, Y. Park and G. Yeom, "High rate etching of sapphire wafer using $Cl_2/BCl_3/Ar$ inductively coupled plasmas", *Mater. Sci. Eng., B* **82**, 50 (2001).

[240] H. Morkoc, S. Strite, G. Gao, M. Lin, B. Sverdlov and M. Burns, "Large-band-gap SiC, III-V nitride, and II-VI ZnSe-based semiconductor device technologies", *J. Appl. Phys.* **76**, 1363 (1994).

[241] R. Capaz, H. Lim and J. Joannopoulos, "Ab initio studies of GaN epitaxial growth on SiC", *Phys. Rev. B* **51**, 17755 (1995).

[242] H. Lahreche, M. Leroux, M. Laugt, M. Vaille, B. Beaumont and P. Gibart, "Buffer free direct growth of GaN on 6H--SiC by metalorganic vapor phase epitaxy", *J. Appl. Phys.* **87**, 577 (2000).

[243] P. Waltereit, O. Brandt, A. Trampert, M. Ramsteiner, M. Reiche, M. Qi and K. H. Ploog, "Influence of AlN nucleation layers on growth mode and strain relief of GaN grown on 6H--SiC(0001)", *Appl. Phys. Lett.* **74**, 3660 (1999).

[244] M. A. Sanchez-Garcia, F. Naranjo, J. Pau, A. Jimenez, E. Calleja and E. Munoz, "Ultraviolet electroluminescence in GaN/AlGaN single-heterojunction light-emitting diodes grown on Si (111)", *J. Appl. Phys.* **87**, 1569 (2000).

[245] L. A. Reichertz, I. Gherasoiu, K. M. Yu, V. M. Kao, W. Walukiewicz and J. W. Ager III, "Demonstration of a III--Nitride/Silicon Tandem Solar Cell", *Appl. Phys. Express* **2**, 122202 (2009).

[246] A. Krost and A. Dadgar, "GaN-based optoelectronics on silicon substrates", *Mater. Sci. Eng., B* **93**, 77 (2002).

[247] E. Calleja, M. Sánchez-Garcıa, F. Sanchez, F. Calle, F. Naranjo, E. Munoz, S. Molina, A. Sanchez, F. Pacheco and R. Garcıa, "Growth of III-nitrides on Si (111) by molecular beam epitaxy doping, optical, and electrical properties", *J. Cryst. Growth* **201/202**, 296 (1999).

[248] P. Chen, R. Zhang, Z. Zhao, D. Xi, B. Shen, Z. Chen, Y. Zhou, S. Xie, W. Lu and Y. Zheng, "Growth of high quality GaN layers with AlN buffer on Si (111) substrates", *J. Cryst. Growth* **225**, 150 (2001).

[249] P. Drechsel, P. Stauss, W. Bergbauer, P. Rode, S. Fritze, A. Krost, T. Markurt, T. Schulz, M. Albrecht and H. Riechert, "Impact of buffer growth on crystalline quality of GaN grown on Si (111) substrates", *Phys. Status Solidi A* **209**, 427 (2012).

[250] M. Kumar, M. K. Rajpalke, B. Roul, T. N. Bhat, N. Sinha, A. T. Kalghatgi and S. B. Krupanidhi, "The impact of ultra thin silicon nitride buffer layer on GaN growth on Si (111) by RF-MBE", *Appl. Surf. Sci.* **257**, 2107 (2011).

[251] A. Ajagunna, A. Adikimenakis, E. Iliopoulos, K. Tsagaraki, M. Androulidaki and A. Georgakilas, "InN films and nanostructures grown on Si (111) by RF-MBE", *J. Cryst. Growth* **311**, 2058 (2009).

[252] W. A. Doolittle, S. Kang, T. J. Kropewnicki, S. Stock, P. A. Kohl and A. S. Brown, "MBE Growth of High Quality GaN on $LiGaO_2$", *J. Electron Mater.* **27**, L58 (1998).

[253] M. Marezio, "The crystal structure of LiGaO2", *Acta Crystallogr.* **18**, 481 (1965).

[254] H. Neumann, E. Pirl and G. Kühn, "Thermal expansion of $LiGaO_2$", *J. Mater. Sci. Lett.* **6**, 495 (1987).

[255] Q. Paduano, D. Weyburne and S. Q. Wang, "Determination of Alloy Composition and Residual Stress for $Al_xGa_{1-x}N$/GaN Epitaxial Films", *Phys. Status Solidi A* **188**, 821 (2001).

[256] S. Huang, Ph.D. Thesis, *GaN-Based and High-Speed Metal-Semiconductor-Metal Photodetector: Growth and Device Structures for Integration*, Georgia Institute of Technology, 2003.

[257] Used with permission from Preston Galle.

[258] P. Kung, A. Saxler, X. Zhang, D. Walker, R. Lavado and M. Razeghi, "Metalorganic chemical vapor deposition of monocrystalline GaN thin films on b-LiGaO2 substrates", *Appl. Phys. Lett.* **69**, 2116 (1996).

[259] W. A. Doolittle, A. S. Brown, S. Kang, S. W. Seo, S. Huang and N. M. Jokerst, "Recent Advances in III-Nitride Devices Grown on Lithium Gallate", *Phys. Status Solidi A* **188**, 491 (2001).

VITA

Michael Moseley is a native of Blakely, Georgia. He attended the Georgia Academy of Mathematics, Engineering, and Science at Middle Georgia College, where he received an Associate's Degree in Mathematics and Computer Science in 2004. He then attended the Georgia Institute of Technology, where he was awarded a Bachelor's Degree in Computer Engineering in 2007 and a Master's Degree in Electrical and Computer Engineering in 2011. He plans to receive his Ph.D. in May of 2013 under the supervision of Dr. W. Alan Doolittle.

Publications and conference presentations resulting from this work:

M. Moseley, B. Gunning, J. Lowder, G. Namkoong, and W. A. Doolittle, "Structural and Electrical Characterization of InN, InGaN, and p-InGaN Grown by Metal-Modulated Epitaxy," J. Vac. Sci. Technol. B. 31, 03C104 (2013).

A. M. Fischer, Y. O. Wei, F. A. Ponce, **M. Moseley**, B. Gunning, W. A. Doolittle, "Lattice-mismatch strain relaxation in thick InxGa1-xN layers with x =>0.66," submitted to Advanced Materials, (2012).

W. L. Calley, P. G. Staib, W. E. Henderson, J. Lowder, J. D. Greenlee, **M. Moseley**, and W. A. Doolittle, "An In situ Auger Probe Enabling Epitaxy Composition Control of Alloys by Elemental Surface Analysis," accepted to J. Vac. Sci. Technol. B. (2012).

J. Greenlee, W. Calley, **M. Moseley**, W. A. Doolittle, "Comparison of Interfacial and Bulk Ionic Motion in Analog Memristors," IEEE Trans. Electron Dev., 60, 427 (2012).

M. Moseley, B. Gunning, J. Greenlee, J. Lowder, G. Namkoong, and W. A. Doolittle, "Observation and Control of the Surface Kinetics of InGaN for the Elimination of Phase Separation," J. Appl. Phys., 112, 014909 (2012).

B. Gunning, J. Lowder, **M. Moseley**, and W. A. Doolittle, "Negligible carrier freeze-out facilitated by impurity-band conduction in highly p-type GaN," Appl. Phys. Lett., 101, 082106 (2012).

M. E. Zvanut, Y. Uprety, J. Dashdorj, **M. Moseley**, and W. Alan Doolittle, "Passivation and Activation of Mg acceptors in heavily doped GaN," J. Appl. Phys., 110, 044508 (2011).

M. Moseley, J. Lowder, D. Billingsley, W. A. Doolittle, "Control of Surface Adatom Kinetics for the Growth of High-Indium Content InGaN Throughout the Miscibility Gap," Appl. Phys. Lett., 97, 191902 (2010).

M. Rubio-Roy, F. Zaman, Y. Hu, C. Berger, **M. Moseley**, J. Meindl, and W. de Heer, "Structured epitaxial graphene growth on SiC by selective graphitization using a patterned AlN cap," Appl. Phys. Lett., 96, 082112 (2010).

M. Moseley, D. Billingsley, W. Henderson, E. Trybus, and W. A. Doolittle, "Transient Atomic Behavior and Surface Kinetics of GaN," J. Appl. Phys. 106, 014905 (2009).

G. Namkoong, S. Huang, **M. Moseley**, and W. A. Doolittle, "In-plane anisotropic strain of elastically and plastically deformed III-nitrides on lithium gallate," Thin Solid Films, 517, 6508 (2009).

E. Trybus, W. A. Doolittle, **M. Moseley**, W. Henderson, D. Billingsley, G. Namkoong, and D. C. Look, "Extremely High Hole Concentrations in c-Plane GaN," Phys. Status Solidi C, 6, S788 (2009).

G. Namkoong, E. Trybus, K. K. Lee, **M. Moseley**, W. A. Doolittle, and D. C. Look, "Metal modulation epitaxy growth for extremely high hole concentrations above 10^{19} cm^{-3} in GaN," Appl. Phys. Lett. 93, 172112 (2008).

Michael Moseley, Brendan Gunning, Jordan Greenlee, Jonathan Lowder, W. Alan Doolittle, "Characterization of MBE Grown, Threading Dislocation Free, High-Indium InGaN without Phase Separation," 29th North American Molecular Beam Epitaxy Conference, Stone Mountain, GA, USA, October 2012.

Chloe Fabien, **Michael Moseley**, Brendan Gunning, W. Alan Doolittle, A.M. Fisher, Y. Wei, F.A. Ponce, "Observation and Control of the Surface Kinetics of InGaN for the Elimination of Phase Separation," 29th North American Molecular Beam Epitaxy Conference, Stone Mountain, GA, USA, October 2012.

Brendan Gunning, **Michael Moseley**, W. Alan Doolittle, "Impurity Band Conduction in Highly p-type GaN and InGaN," 29th North American Molecular Beam Epitaxy Conference, Stone Mountain, GA, USA, October 2012.

Michael Moseley, Jonathan Lowder, Brendan Gunning, M. E. Zvanut, J. Dashdorj, W. Alan Doolittle, "Characterization of Mg Acceptors in GaN:Mg Grown by Metal Modulated Epitaxy and MOCVD," American Vacuum Society 58th International Symposium and Exhibition, Nashville, Tennessee, USA, October 2011.

Michael Moseley, Brendan Gunning, Jonathan Lowder, Gon Namkoong, W. Alan Doolittle, "Elimination of Indium Surface Segregation inInGaN Grown Throughout the Miscibility Gap," American Vacuum Society 58th International Symposium and Exhibition, Nashville, Tennessee, USA, October 2011.

Brendan Gunning, **Michael Moseley**, Jonathan Lowder, W. Alan Doolittle, J. Wierer, S. Lee, D. Koleske, Q. Li, "Metal-Modulated Epitaxy Growth of InGaN/GaN p-i-n Solar Cells," American Vacuum Society 58th International Symposium and Exhibition, Nashville, Tennessee, USA, October 2011.

W. Laws Calley, P. G. Staib, Jonathan Lowder, Jordan Greenlee, **Michael Moseley**, Walter Henderson, W. Alan Doolittle, "An Auger Electron Analyzer System for In Situ MBE Growth Monitoring" American Vacuum Society 58th International Symposium and Exhibition, Nashville, Tennessee, USA, October 2011.

Michael Moseley, Brendan Gunning, Jonathan Lowder, W. Alan Doolittle, "Elimination of Indium Surface Segregation in InGaN Grown Throughout the Miscibility Gap," 9th International Conference on Nitride Semiconductors, Glasgow, Scotland, UK, July 2011.

Michael Moseley, Brendan Gunning, Jonathan Lowder, Gon Namkoong, W. Alan Doolittle, "InN and n and p-type InGaN Grown by Metal-Modulated Epitaxy," 9th International Conference on Nitride Semiconductors, Glasgow, Scotland, UK, July 2011.

Brendan Gunning, **Michael Moseley**, Jonathan Lowder, W. Alan Doolittle, J. Wierer, S. Lee, D. Koleske, Q. Li, "InGaN/GaN p-i-n Solar Cells Grown by Metal-Modulated Epitaxy," 9th International Conference on Nitride Semiconductors, Glasgow, Scotland, UK, July 2011.

Jonathan Lowder, **Michael Moseley**, Brendan Gunning, W. Alan Doolittle, M. E. Zvanut, J. Dashdorj, "Characterization of Mg Acceptors in GaN:Mg grown by Metal Modulated Epitaxy and MOCVD," 9th International Conference on Nitride Semiconductors, Glasgow, Scotland, UK, July 2011.

Michael Moseley, Jonathan Lowder, Brendan Gunning, Daniel Billingsley, Gon Namkoong, W. Alan Doolittle, "Observation and Elimination of Indium Surface Segregation," Electronic Materials Conference 2011, Santa Barbara, CA, USA, June 2011.

Michael Moseley, Jonathan Lowder, Brendan Gunning, Elaissa Trybus, Daniel Billingsley, Walter Henderson, Gon Namkoong, W. Alan Doolittle, "Deeply Degenerate p-type Doping in III-Nitrides: Critical Milestones Achieved for High Power Electronics," Air Force Office of Scientific Research Joint Electronics Program Review, Arlington, VA, USA, May 2011.

Farhana Zaman, Miguel Rubio-Roy, **Michael Moseley**, Jonathan Lowder, W. Alan Doolittle, Claire Berger, Rui Dong, James Meindl, Walt de Heer, "Selective Epitaxial Graphene Growth on SiC via AlN Capping," APS March Meeting 2011, Dallas, Texas, USA, March 2011.

M. E. Zvanut, Y. Uprety, J. Dashdorj, **M. Moseley**, W. A. Doolittle, "Hydrogen incorporation in high hole density GaN:Mg," APS March Meeting 2011, Dallas, Texas, USA, March 2011.

Michael Moseley, Jonathan Lowder, Daniel Billingsley, Gon Namkoong, and W. Alan Doolittle, "Control of Adlayer Kinetics via Metal Modulated Epitaxy for the Growth of High Quality InGaN," 27th North American Molecular Beam Epitaxy Conference, Breckenridge, CO, USA, September 2010. Best Student Presentation Award.

Laws Calley, Philippe Staib, Walter Henderson, Jonathan Lowder, Jordan Greenlee, **Michael Moseley**, and W. Alan Doolittle, "An Auger Electron Analyzer System for In-situ MBE Stoichiometry Control," 27th North American Molecular Beam Epitaxy Conference, Breckenridge, CO, USA, September 2010.

Mary Ellen Zvanut, Jamiyana Dashdorj, **Michael Moseley**, and W. Alan Doolittle, "The Local Environment of the Mg Impurity in High Hole Density p-type GaN:Mg," 6th International Workshop on Nitride Semiconductors, Tampa, Florida, USA, September 2010.

Christiana Honsberg, **Michael Moseley**, and W. Alan Doolittle, "Progress and Future Prospects for InGaN Solar Cells," 6th International Workshop on Nitride Semiconductors, Tampa, Florida, USA, September 2010.

Jonathan Lowder, **Michael W. Moseley**, Elaissa Trybus, Walter Henderson, Daniel Billingsley and W. Alan Doolittle, "Deeply Degenerate p-GaN with Hole Concentrations Exceeding 7×1019 cm-3 Grown by Metal-Modulated Epitaxy," 6th International Workshop on Nitride Semiconductors, Tampa, Florida, USA, September 2010.

Michael Moseley, Jonathan Lowder, Daniel Billingsley, Gon Namkoong, W. Alan Doolittle, "Control of Adlayer Kinetics for the Growth of High-Quality InGaN Throughout the Miscibility Gap," 6th International Workshop on Nitride Semiconductors, Tampa, Florida, USA, September 2010.

W. A. Doolittle, **M. Moseley**, and E. Trybus, "Deeply-degenerate p-type GaN grown by metal modulated epitaxy," International Semiconductor Device Research Symposium 2009, College Park, Maryland, USA, December 2009.

W. Alan Doolittle, **Michael Moseley**, Elaissa Trybus, Daniel Billingsley, Walter Henderson, David Look, M. E. Zvanut, and J. Dashdorj, "Deeply Degenerate p-GaN Grown by Metal-Modulated Epitaxy," 8th International Conference on Nitride Semiconductors, Jeju, Korea, October 2009.

J. A. Freitas Jr., D. Look, P. Klein, **M. Moseley**, E. Trybus, W. Henderson, and W. A. Doolittle, "Compensation and Activation Mechanism in Metal Modulated Epitaxy p-GaN," 8th International Conference on Nitride Semiconductors, Jeju, Korea, October 2009.

Michael Moseley, Elaissa Trybus, Daniel Billingsley, Walter Henderson, Gon Namkoong, David Look, and W. Alan Doolittle, "Deeply Degenerate p-GaN Grown by Metal-Modulated Epitaxy," 26th North American Molecular Beam Epitaxy Conference, Princeton, NJ, August 2009. Best Student Presentation Award.

Elaissa Trybus, Walter Henderson, **Michael Moseley**, Gon Namkoong, David Look, Jaime Freitas, and W. Alan Doolittle, "Analysis of Degenerate p-type GaN by Metal-Modulated Epitaxy," 51st Electronic Materials Conference, University Park, PA, June 2009.

Elaissa Trybus, Shawn Burnham, Gon Namkoong, David C. Look, Daniel Billingsley, **Michael Moseley**, Walter Henderson, and W. Alan Doolittle, "Systematic Study of High Hole Concentration, Low Temperature Grown GaN Approaching the Compensated Region," 50th Electronic Materials Conference, Santa Barbara, CA, June 2008.